This electronic thesis or dissertation has been downloaded from Explore Bristol Research, http://research-information.bristol.ac.uk

Author:
Blower, Jonathan David

Title:
Degassing processes in volcanic eruptions.

Degassing Processes in Volcanic Eruptions

Jonathan David Blower

Department of Earth Sciences

University of Bristol

A Thesis submitted to the University of Bristol in accordance with the requirements for the degree of Doctor of Philosophy in the Faculty of Science

May 2001

Abstract

The loss of gas from magma (degassing) is a fundamental control on the physics of volcanic eruptions. This thesis contains three studies in which the dynamics of different aspects of magmatic degassing are investigated in detail.

Chapter 2 is an investigation of the generation of bubble size distributions (BSDs) in volcanic rocks. Results from numerical modelling, laboratory analogue experiments and textural observations of volcanic tephra are presented. It is shown that power law and exponential BSDs, both commonly observed in volcanic rocks, can form as a result of continuous nucleation of bubbles as magma ascends through the conduit. This contrasts with the commonly-employed assumption that nucleation occurs as a single event in response to decompression.

A numerical model of bubble growth is developed and applied in chapter 3. The study focuses on the consequences of incorporating the dependence of melt viscosity and volatile diffusivity on the concentration of water. A coupling between the effects of viscosity and diffusivity is revealed. A high diffusivity leads to fast mass transfer of volatiles into the bubbles, promoting growth and rapidly dehydrating the melt shell around the bubble. This leads to a rapid increase in the viscosity of the melt, inhibiting growth. The net rate of bubble growth is the result of a competition between these effects. With concentration-dependent diffusivity bubble growth rates are enhanced compared with those resulting from constant diffusivities of similar magnitude. This is due to the form of the profile of water concentration in the melt; in the case of concentration-dependent diffusivity the profile is such that the effective viscosity of the melt is reduced.

The development of permeability in magma may be the cause of transitions between explosive and effusive activity. Chapter 4 describes the formulation of a model which is used to elucidate the factors which control the permeability of magma. Power law relationships between permeability and porosity are revealed, in agreement with previous experimental and theoretical studies. These relationships are independent of the bubble size and insensitive to the form of the bubble size distribution. Permeability–porosity relationships are particularly sensitive to the ease of bubble coalescence in the magma; if bubble coalescence is difficult due to, for example, a high melt viscosity, permeability is significantly reduced.

For my parents

Acknowledgements

First and foremost, I would like to thank my supervisors Heidy Mader and Jeremy Phillips. Their constant help and guidance throughout the past three years are enormously appreciated. I am very glad to have had the opportunity of collaborating with Jon Keating and Simon Wilson. Their contributions, particularly to the mathematical aspects of the studies in this thesis, have been a vital part of this research. I would also like to thank Steve Sparks, Gerald Ernst, Catherine Mourtada-Bonnefoi, Oded Navon, Oleg Melnik, Colm Caulfield and the members of the GFD group for countless discussions and suggestions at all stages of this research. I am indebted to all my friends, particularly the denizens of office G9, for *not* discussing my research and thus ensuring my continued sanity— so thanks to Audrey, Ed, Tim, Jim, Debbie, Stu, Claire, Chloe, Costanza, Sue, several Jons and countless others.

For help with computer programming and numerical modelling, I would like to thank Ian Stewart, Don Henderson and Hugh Dixon. I am grateful to Bill Bosl for discussions on the subject of permeability and to Ian Wright for supplying bubble size distribution data. I would like to thank the workshop staff, Fred Wheeler, Mike Dury and Phil Boyd, for all their efforts and advice in the construction and use of the laboratory apparatus.

Special thanks must go to my family for continuous love, support and encouragement, in particular to my parents to whom this thesis is dedicated.

Author's declaration

I declare that the work in this dissertation was carried out in accordance with the Regulations of the University of Bristol. The work is original except where indicated by special reference in the text and no part of this dissertation has been submitted for any other degree.

Any views expressed in the dissertation are those of the author and in no way represent those of the University of Bristol.

The dissertation has not been presented to any other University for examination either in the United Kingdom or overseas.

SIGNED   DATE

Contents

List of Figures

List of Tables

Chapter 1

Introduction

Volcanoes are among the world's greatest natural hazards. It is estimated that over five hundred million people are currently at risk from their effects. The explosive power of volcanoes can be immense; the energy of the May 1980 eruption of Mount St. Helens was around a hundred times that of an atomic bomb. The 1815 eruption of Tambora, Indonesia, is the largest known historical eruption and was a further hundred times more energetic than the Mount St. Helens blast. Large explosive eruptions such as these produce immense mushroom clouds of gas and ash which can rise several tens of kilometers into the stratosphere. The effects of these eruption clouds can be global. Large amounts of sulphur dioxide are carried with the cloud into the upper atmosphere forming aerosols of sulphuric acid which scatter the sun's rays and cause a cooling of the earth's surface. The aerosols resulting from the 1991 eruption of Mount Piñatubo caused a temporary global cooling of around $0.5°C$. In the aftermath of the 1815 eruption of Tambora, global cooling was so marked as to cause widespread crop failure in the following two years; 1816 became known throughout Europe as the "year without a summer".

Each volcano is unique and presents its own hazards. Eruptions do not have to be highly explosive to cause widespread devastation and loss of life. Many volcanoes are topped by

glaciers and an eruption can cause the ice to melt, generating a flood. These floods, or *jökulhlaups*, are a particular hazard in Iceland, where subglacial eruptions occur frequently. In 1996 a volcano (Loki) erupted under the Vatnajökull glacier in southern Iceland, the largest glacier in Europe. Three billion cubic metres of water were released, causing widespread destruction of property and the island's infrastructure. In 1985 over twenty thousand lives were lost at Nevada del Ruiz, Colombia, when glacial meltwater formed a *lahar*, or volcanic mudflow, which flowed for 100 km along river valleys. Lahars are produced when rain or meltwater erodes the loose soil and ash on the steep slopes of a volcano, creating a fast-moving, highly-destructive river of dense mud. The recent activity at the Soufrière Hills volcano on Montserrat in the West Indies has drawn attention to a particularly deadly variety of volcanic hazard; the pyroclastic flow. Pyroclastic flows are essentially hot avalanches of rock, dust and gas which can attain speeds of hundreds of miles per hour, devastating anything in their path.

In the last three hundred years a quarter of a million people have lost their lives as a result of volcanic activity. There is clearly a need to be able to predict accurately the future behaviour of a volcano. It is important to be able to forecast not only *when* a volcano will erupt but also what will happen when it does. To this end, most of the world's largest and most dangerous volcanoes are constantly monitored in order to be able to anticipate any future activity. Valuable information can also be gleaned from field observations of the deposits of past eruptions. Up until the middle of the twentieth century, the bulk of our knowledge about volcanoes was obtained by these methods.

Predictions of volcanic hazards are reliant on an understanding of exactly how and why volcanoes erupt. The relative infrequency of large eruptions, together with the huge variety of volcanoes and eruption types, means that it can be very difficult to extract general principles of the behaviour of volcanoes by direct observation of eruptions or their deposits alone. In the past few decades, a great deal of research has focused on the detailed investigation of the fundamental physical processes which control volcanic eruptions. This

discipline has come to be known as *physical volcanology*.

1.1 Physical volcanology

In general, the aim of the physical volcanologist is to use an understanding of physics to develop models of volcanic eruptive behaviour. This approach is not intended by any means to replace the vital exercise of collecting primary data on past and present eruptions; on the contrary, theoretical models must always be tested against concrete evidence from the natural system. Physical volcanology is therefore a multi-disciplinary science, attracting physicists, chemists and mathematicians to join volcanologists in directing their energies towards the understanding of volcanic processes. The attraction does not lie only in the important and practical nature of the subject; volcanoes present very many fascinating and unique problems to the researcher which are of great interest in themselves. The relative youth of the discipline means that very many important questions are still to be answered.

It is instructive at this point to discuss the basic anatomy of a volcanic eruption. Figure 1.1 depicts a cross-section through a volcano during an explosive eruption. Magma is initially stored in a chamber underneath or within the volcano. The magma contains dissolved gases; in the case of most explosive eruptions the dominant gas is H_2O, but in some eruptions, particularly those involving basaltic magma, other gases such as CO_2 may be prevalent.

If the pressure on the magma chamber drops due to, for example, the breaking of a blockage in the system or the collapse of the volcanic edifice, the dissolved gas can no longer be held in solution. Bubbles form and grow rapidly, driving the magma up through the conduit. At a certain point the magma may spontaneously disrupt or *fragment* into a spray of ash and gas, giving an explosive eruption. If fragmentation does not occur then the magma
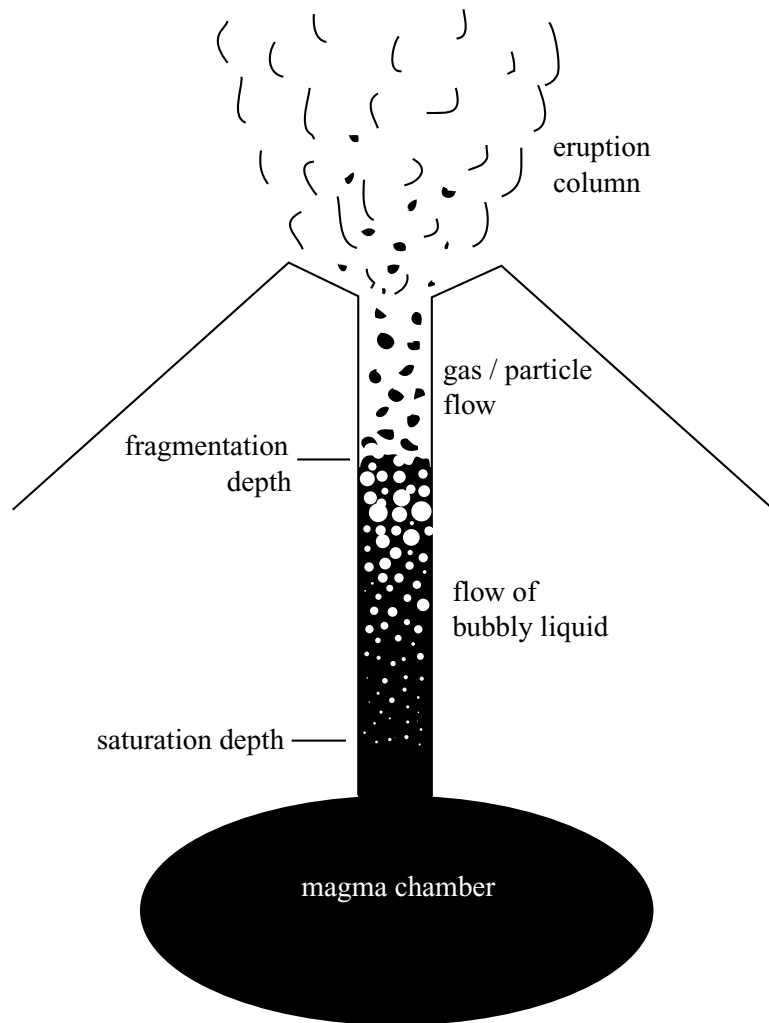
Figure 1.1: The 'classic' model of an explosive volcanic eruption (e.g. McBirney 1973; Wilson et al. 1980). Magma, containing dissolved volatile compounds such as H_2O, is held in a chamber under the pressure of the overlying rocks. If this pressure is released, water comes out of solution and forms bubbles at the saturation depth. These bubbles grow, driving a flow of bubbly liquid up through the conduit towards the surface. At a certain depth in the conduit, the bubbly magma fragments to form a gas flow containing droplets of bubble-rich liquid which solidify to form pumice and ash. This particulate gas flow rapidly expands to form a vigorously-convecting eruption column.

erupts as a bubbly liquid (lava) in an *effusive* eruption.

Verhoogen (1951) published one of the first studies which attempted to explain volcanic phenomena in a quantitative, physical context. He considered a question which remains unanswered even today, that of what causes magma inside a volcano to disrupt, forming an ash cloud. He proposed that magma fragments when bubbles grow more quickly than they can escape from the magma due to their buoyancy. Bubbles can therefore join together, transforming the magma from a bubbly foam into a gas-rich spray. However, McBirney (1963) showed that bubbles cannot easily escape from magma due to the high viscosity of the liquid and so Verhoogen's analysis is probably not valid in most cases. McBirney and Murase (1970) developed an alternative theory, proposing that fragmentation occurs when the pressure within the gas bubbles exceeds the tensile strength of the magma. McBirney (1973) was one of the first to propose that explosive activity is favoured by a high viscosity of the melt which retards bubble growth and allows bubble pressure to build. This explained why eruptions of andesitic magma are more likely to be explosive than their basaltic counterparts; previously it had been thought that this was due to the presence of a higher concentration of dissolved gases in andesitic melt.

Although these studies have been largely superseded, they have highlighted several important points. In particular, they have demonstrated the potential of theoretical investigation to explain the diversity of volcanic eruption types. Volcanoes are clearly extremely complicated systems, and the style of an eruption is the product of very many different factors. This complexity has restricted the development of mathematical models of eruptions; the governing equations cannot be solved exactly except in highly simplified cases. It is no coincidence that the recent acceleration in progress in physical volcanology is contemporaneous with the rapid development of computer technology; many studies use computer-based models to solve complex problems in volcanology. Progress in physical volcanology is dependent on an accurate knowledge of the physical properties of magma (such as its density, viscosity and heat capacity), a need recognized by McBirney and

Murase (1970). In response to this need, valuable data has been supplied by the studies of Shaw (1972), Murase and McBirney (1973), Zhang (1991) and Hess and Dingwell (1996), to name but a small selection of works from this important and ongoing area of research.

Despite these advances, our understanding of the details of the processes sketched out in figure 1.1 remains incomplete. Significant gaps in our knowledge include:

- A paucity of data concerning the geometry of the magmatic plumbing system. It is very unlikely that the volcanic conduit is perfectly straight and parallel-sided as figure 1.1 implies. The magma chamber is likely to be similarly irregular in shape. Ryan (1988) used seismic data to reconstruct the large-scale plumbing system under Kilauea volcano, Hawaii and discovered a complex and tortuous network of chambers and passages. This remains, however, a rare example of the study of the shape of magma chambers and volcanic conduits.

- A limited understanding of the rheology of multiple-phase mixtures of liquid, particles and bubbles. Rheology is the science of how liquids deform under stress and is a major control on how magma flows both underground through the volcanic system and, once erupted, over ground. The viscosity (resistance to flow) of magma is strongly affected by the presence of bubbles and crystals. Theoretical studies (e.g. Einstein 1906, 1911; Taylor 1932; Frankel and Acrivos 1970) of these effects are only applicable if the volumetric concentration of bubbles or crystals is very low (the dilute limit) or very high (the dry limit), but magma is commonly observed to contain crystals and bubbles in intermediate concentrations. Experimental studies have proven to be the most fruitful source of information in this field. The effect of crystals on magma rheology is comparatively well-understood (Pinkerton and Stevenson 1992; Lejeune and Richet 1995); crystals increase the magnitude of the magma viscosity and also introduce complex non-Newtonian behaviour. The effect of bubbles on magma rheology is less clear. Some theoretical and experimental studies reveal

an increase in magma viscosity with the volume fraction of bubbles (Einstein 1911; Taylor 1932; Stein and Spera 1992). In the experiments of Bagdassarov and Dingwell (1992) and Lejeune et al. (1999), however, the opposite effect was noted; magma viscosity *decreased* with increasing gas content. These contradictory findings may be explained by the study of Llewellin, Mader and Wilson (*The rheology of a bubbly liquid*, manuscript submitted to Proceedings of the Royal Society A) in which it is shown that the presence of bubbles may either increase or decrease the viscosity of a bubbly liquid depending on the exact conditions of shear.

- A lack of consensus about the mechanism by which magma fragments into ash and pumice. This process is fundamental to the understanding of the conditions under which an explosive eruption might occur. Despite being one of the oldest problems in physical volcanology (Verhoogen 1951) this issue remains unresolved. Many theories have been proposed to explain the fragmentation process. Early models (e.g. Wilson et al. 1980) proposed that magma disrupts when the volume fraction of bubbles reaches the close packing limit of identical spheres (74.1%). This is clearly an oversimplification as volcanic rocks such as pumices contain bubbles of a wide range of sizes and bubbles shapes are often far from spherical. Alidibirov (1994) developed a model of the dynamics of volcanic blasts in which highly viscous magma fragments due to the pressure in the bubbles exceeding the tensile strength of magma (cf. McBirney and Murase 1970). Papale (1999) proposed that fragmentation occurs when the elongation strain rate of magma exceeds some critical value, a condition which turns out to be mathematically the same as the bubble overpressure condition (Melnik 1999). Current theories concerning the mechanics of fragmentation (reviewed by Sahagian 1999) are complex and combine many previous ideas. It is proposed that magma, if it is stretched rapidly enough, can behave as a brittle solid and break apart. Under slow strains, magma behaves as a viscous liquid and will deform in a ductile fashion. However, if bubbles grow rapidly and the overpressure

inside them is high then the bubble walls are put under great stress. If this stress exceeds the tensile strength of the magma then brittle fragmentation occurs (Zhang 1999a). Martí et al. (1999) found that the textures observed in highly-deformed pumices were consistent with a fragmentation mechanism based on the transition from ductile to brittle behaviour. Zhang's (1999a) theory is a persuasive one but it is very new and not yet universally accepted.

All the above processes are very important topics of current research and must be investigated further in order to develop a more complete understanding of the physics behind volcanic eruptions. The studies in this thesis, however, focus on a different, but equally important, aspect of volcanic eruption dynamics, that of magmatic degassing. The remainder of this introduction is devoted to a general overview of the principal issues related to the degassing of magma. More comprehensive discussions of these problems can be found at the start of the subsequent chapters in this thesis, as outlined in section 1.4.

1.2 Degassing processes

Volcanic eruptions are driven by the expansion of gas (figure 1.1). Magma can contain up to a few weight percent of dissolved volatile compounds such as H_2O, CO_2, SO_2, Cl_2 and H_2S. In most cases of highly explosive eruptions, the most abundant volatile species is H_2O; figure 1.2 describes the origin of this water. In the following discussion, and indeed the remainder of this thesis, it shall be assumed that H_2O is the only gas present in the magma. Most of the principles and results discussed herein can, however, be readily extended to other gas species. The mechanisms by which volatile species such as water are lost from magma are collectively known as *degassing* processes. They include the nucleation and growth of bubbles and the loss of gas by permeable flow through the magma. Degassing processes provide fundamental controls on the behaviour of volcanic eruptions and have
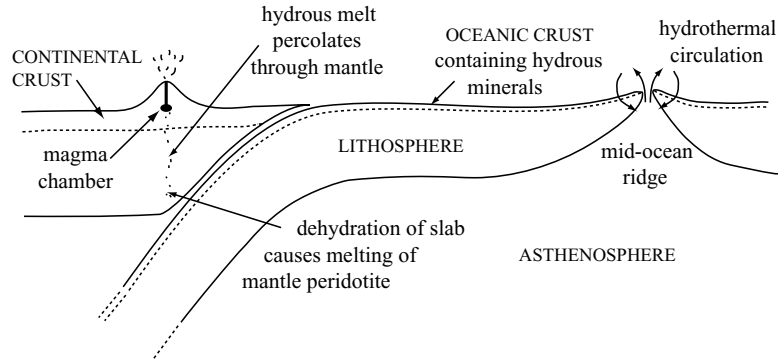
Figure 1.2: The origin of dissolved water in the majority of highly explosive volcanic systems. Water is incorporated into the oceanic crust in hydrothermal systems. This water, in the form of hydrous minerals such as serpentinite, is carried with the plate into subduction zones, where it is released into the mantle wedge above the subducting plate. Upon hydration, the melting point of the mantle peridotite is lowered. Small quantities of water-rich melt form and slowly percolate through the mantle into the crust. Here the melt accumulates and its chemical composition is altered by a combination of differentiation (fractional crystallization) and crustal assimilation.

thus become the subject of intense research.

Degassing commences when bubbles start to nucleate in magma, usually in response to a decompression which reduces the pressure of the magma to below the saturation pressure of water. This saturation pressure depends on the water content of the magma; the higher the water content the higher the pressure required to keep the water in solution. Henry's law gives a simple, and reasonably accurate, expression for the saturation pressure P_s as a function of the mass fraction of water c:

$$P_s = \left(\frac{c}{\alpha}\right)^2 \tag{1.1}$$

where α is the Henry constant which is usually taken to be around 4.11×10^{-6} Pa$^{-1/2}$ (e.g. Jaupart and Allègre 1991). Experimental and theoretical studies show that the pressure must, in fact, fall somewhat below this saturation pressure in order to induce nucleation. This *supersaturation*, ΔP, depends on many factors, especially the presence or absence of crystals in the melt and the composition of the crystal phases (Navon and Lyakhovsky

1998). It is energetically more favourable for bubbles to nucleate on the surface of certain crystals, particularly biotite and magnetite (*heterogeneous* nucleation) than for bubbles to nucleate in crystal-free melt (*homogeneous* nucleation). Typical estimated values for ΔP are < 10 MPa for heterogeneous nucleation and > 80 MPa for homogeneous nucleation (Navon and Lyakhovsky 1998; Mourtada-Bonnefoi and Laporte 1999). A great puzzle, which is beyond the scope of this thesis, is that the process of bubble nucleation is still not at all well-understood at the molecular level (Sahagian 1999).

Once bubbles have nucleated they will grow as long as the pressure inside them (p_g) exceeds the sum of the ambient pressure (p_a) and the surface tension pressure (i.e. if $p_g > p_a + 2\sigma/R$ where σ is the interfacial surface tension between the melt and the vapour and R is the bubble radius). Bubbles grow by a combination of decompression and the input of water molecules which diffuse towards the bubble through the magma. Growth is resisted primarily by the viscosity of the melt (Sparks 1978). A large melt viscosity can retard bubble expansion to such an extent that the pressure inside the bubble remains high during an eruption. This high pressure can cause the magma to fragment and lead to dangerous, explosive behaviour. The dynamics of bubble growth are highly complex and not yet fully understood. The viscosity of the melt, and the diffusivity of water molecules through the melt are both dependent on the concentration of water in the melt. Since the water concentration in the melt around a bubble varies in both time and space, calculating the rates at which bubbles can grow is very complicated. Determination of bubble growth rates is very important as it is the growth of bubbles which drives the expansion of magma up the volcanic conduit.

Once bubbles have grown to a certain size, they may begin to join up and create open pathways for gas flow through the magma. If the walls of the conduit are also permeable, and the pressure inside the magma is greater than that of its surroundings, then gas may be driven out of the volcano. We see abundant evidence of this gas loss in fumaroles (steam vents) and solfataras (sulphur fields) in volcanic areas. In this way a volcano can

quite literally 'let off steam', relieving the pressure inside the volcano and reducing the possibility of the occurrence of explosive activity (Jaupart and Allègre 1991).

Degassing processes are therefore fundamental to the behaviour of volcanoes. Despite decades of intense research there are still many important questions which remain unanswered. These include:

Does degassing proceed in equilibrium with falling pressure?

Many models of volcanic eruptions assume that the loss of gas from magma is a function only of the reduction in pressure (e.g. Melnik 2000). The concentration of water in the magma is therefore given by simple relationships such as Henry's law (equation 1.1). However, detailed studies of degassing (e.g. Proussevitch and Sahagian 1996) show that, under the conditions of an explosive volcanic eruption, the kinetics of degassing are too slow to keep pace with the falling pressure. The precise conditions under which equilibrium degassing can occur are not yet known. This problem is important as the rate of degassing controls the rate of expansion of magma.

How important is the loss of gas from magma by permeable flow?

The models of Jaupart and Allègre (1991), Woods and Koyaguchi (1994) and Melnik and Sparks (1999) show that, if gas can be lost from magma as it ascends through the conduit, then complex cycles between explosive and effusive eruptions are expected. Accurate modelling of this requires a knowledge of how rapidly gas is lost from magma. If it is lost by permeable flow through the magma itself then it is important to know at what stage open pathways through the magma can exist and to be able to calculate values of magma permeability. No model currently exists to do this.

What are the mechanisms controlling bubble nucleation?

In many simple models of explosive volcanism (e.g. figure 1.1), it is assumed that all bubbles nucleate at the saturation depth in a single 'burst' of nucleation. I have mentioned that a significant supersaturation is necessary to induce nucleation. If the supersaturation is large then bubbles may not form until late in an eruption when the magma is near the surface (Mangan and Sisson 2000). In this case the growth of bubbles is likely to be extremely rapid (Sparks 1978; Proussevitch et al. 1993a), and the eruption may be explosive. Furthermore, the assertion that no more bubbles form after the initial nucleation event is unlikely to be true. Textural studies of volcanic rocks reveal the presence of bubbles which very likely nucleated late in an eruption (e.g. Navon et al. 1998) There are currently no predictive models which adequately describe the mechanics of bubble nucleation (Sahagian 1999).

What are the effects of concentration-dependent viscosity and diffusivity on bubble growth?

The dynamics of bubble growth in magmas have been investigated by several authors (e.g. Sparks 1978; Lyakhovsky et al. 1996; Proussevitch and Sahagian 1996). These studies provided valuable insights into the process but were limited by assumptions of constant viscosity and diffusivity. As bubbles grow, a volatile-depleted, highly viscous shell forms around the bubble. This viscous shell will restrict bubble growth and allow high internal pressures to be maintained, but the extent to which this can occur is not known. The presence of this viscous shell is also likely to affect the dynamics of bubble coalescence and the rheology of the magma. More recent studies (Navon et al. 1998; Proussevitch and Sahagian 1998) have incorporated the effects of volatile-dependent viscosity and diffusivity, but the implications of this were not discussed.

What can the textures of volcanic rocks tell us about eruption processes?

The physical processes which operate during a volcanic eruption can rarely be observed *in situ*. Many studies have therefore attempted to infer the nature of these processes through the examination of the products of an eruption such as pumice, scoria and lava. Typically, evidence is gleaned from the examination of the sizes, shapes and distributions of bubbles and crystals. Most of these studies are semi-quantitative or qualitative in nature (e.g. Gardner et al. 1998) but have led to the development of many interesting and important theories about the physics of volcanic eruptions. For example, Stasiuk et al. (1996) noted that bubbles in the magma inside a fossil conduit had become aligned by shear, allowing the bubbles to join together to form an open pathway for gas escape to the conduit walls. It is notoriously difficult to develop rigorous, quantitative models which can explain the production of pumice textures in terms of real physical processes. However, the examination of one textural parameter, the bubble size distribution (BSD), has proved to be a fruitful line of research in this area. The studies of Toramaru (1989, 1990), Mangan and Cashman (1996) and Gaonac'h et al. (1996a) have drawn links between the BSDs of volcanic rocks and eruption parameters such as the ascent rate of magma and the rates of growth and nucleation of bubbles.

1.3 Modelling volcanic eruptions

The studies in this thesis each focus on an individual aspect of the volcanic degassing process. The studies of, for example, Wilson et al. (1980), Jaupart and Allègre (1991), Woods and Koyaguchi (1994), Papale et al. (1998), Melnik and Sparks (1999) and Melnik (2000) take a contrasting approach. In these investigations, the focus is on large-scale processes such as the expansion, flow and fragmentation of magma. These so-called 'conduit flow models' have provided extremely valuable insights about volcanic phenomena and eruptive

behaviour. They are, however, limited by many simplifying assumptions. Many of these assumptions pertain to the degassing of magma; very often the details of the degassing process are overlooked. Conversely, the investigations in this thesis do not incorporate the dynamics of magma flow and expansion. In a volcanic eruption the processes of degassing and large-scale flow are highly coupled and must be investigated simultaneously in order to gain deeper insights into the factors which control eruptive behaviour. To this end, each chapter in this thesis concludes with a section describing how its findings might influence our understanding of large-scale volcanic processes.

Although theoretical models of volcanic eruptions will continue to increase in sophistication and complexity, it is unlikely that every single aspect of the physics of volcanic processes will be captured in a single model. It is therefore vital to isolate those processes which are most important in controlling the dynamics of eruptions. Certain parameters may have a very strong influence on the eruption dynamics whereas others may have little effect and only serve to complicate the model. I have followed this philosophy by including tests of sensitivity in the models described in this thesis. For example, in chapter 4 I shall show that it is not necessary to know the exact form of the bubble size distribution to be able to calculate the permeability of magma. In contrast, in order to model bubble growth accurately (chapter 3) parameters such as the melt viscosity and volatile diffusivity must be tightly constrained.

1.4 The structure of this thesis

This thesis contains descriptions of three main areas of study. Chapter 2 is an investigation of the generation of the distribution of bubble sizes in volcanic rocks, combining evidence from numerical modelling, laboratory experiments and the examination of natural samples. These lines of evidence are used to draw inferences about the nucleation of bubbles during explosive eruptions. Chapter 3 describes the formulation of, and results

from, a numerical model of the dynamics of bubble growth, focusing particularly on the effects of the dependence of melt viscosity and volatile diffusivity on water concentration. In chapter 4 a model is developed and used to calculate the permeability of magma as a function of its porosity, the size distribution of bubbles and other parameters. The permeability of magma is a very important factor in the calculation of how rapidly gas can be lost from the volcanic system.

Each chapter opens with a brief summary of its main findings. This is followed by a substantial introductory section which collates the findings of previous studies and describes the importance of, and motivation behind, each piece of work. Each chapter closes with a summary of its results and a discussion outlining how these results contribute to the wider picture of modelling large-scale volcanic processes.

The chapters may be read as separate, self-contained entities, but their results are mutually linked. The thesis concludes (chapter 5) with a synthesis of the results of the previous chapters and a discussion of the implications of the findings of the thesis as a whole.

Four appendices provide supporting data and calculations for the main chapters. Appendix A gives the derivation of a key equation which is used in the measurement of bubble size distributions in chapter 2. Appendix B describes the physical properties of solutions of gum rosin and acetone; this liquid is used in analogue experiments of magma degassing in chapter 2. The bubble growth model of chapter 3 incorporates an equation describing the motion of fluid around a growing bubble in the case of a radially-varying viscosity; the derivation of this equation is given in appendix C. Appendix D also pertains to this bubble growth model and describes how the diffusion equation is solved numerically.

Chapter 2

The evolution of bubble size distributions in volcanic eruptions

2.1   Summary

Both power law and exponential bubble size distributions (BSDs) have been observed in many different types of volcanic rocks. These two forms of BSD have previously been attributed to two distinct mechanisms; a process of cascading coalescence gives power law BSDs and exponential BSDs are interpreted as the result of steady-state bubble nucleation and growth. In this chapter I shall discuss results of computer simulations and laboratory analogue experiments and show that both distributions can be interpreted as the product of continuous bubble nucleation resulting from non-equilibrium degassing. This ongoing nucleation causes the bubbles to evolve through an exponential size distribution into a power law size distribution as nucleation and growth progress; thus a single mechanism can explain both forms of BSD.

Many present models of the expansion and flow of magma in explosive volcanic eruptions make the simplifying assumption that degassing occurs in perfect equilibrium with pressure. By contrast, models of bubble growth show that, for high melt viscosity, rapid depressurization, low volatile diffusivity or low initial nucleation density the rate of de-

gassing is unlikely to be fast enough to keep pace with the falling pressure. This apparent contradiction may be resolved by the findings of this study; the efficiency of degassing may be increased by the nucleation of new bubbles.

2.2 Introduction

The inaccessibility of the volcanic interior means that the dynamics of degassing cannot be directly observed *in situ*. Processes of bubble nucleation and growth must be inferred from secondary sources such as theoretical studies, laboratory investigations and textural examination of volcanic deposits. Over the last two decades the detailed analysis of the structure of volcanic rocks such as pumice, scoria and lava has become a standard tool in the deduction of eruption parameters. One of the most common textural parameters which has been measured is the bubble size distribution (BSD) of the rock.

Sparks and Brazier (1982) published some of the first measurements of bubble size distributions in pumice. BSDs from five different pumice samples from different eruptions were reported and although quantitatively different, the five BSDs had very similar overall characteristics, showing three pronounced peaks at different bubble sizes. The authors interpreted the coarsest peak as originating from slow vesiculation in the magma chamber prior to eruption. The peak at intermediate bubble size was attributed to vesiculation in the conduit during an eruption and the fine population was interpreted as forming during or after fragmentation as the pressure rapidly fell. In the study, BSDs were measured using mercury porosimetry in which liquid mercury is forced into the pore spaces of a pumice. The pressure needed to drive the liquid into a pore space is related to the size of the pore. This method is, however, no longer widely used as it is suspected that the the measurements which arise from it are misleading; technically, the procedure measures the characteristic size of the apertures between pores, rather than the size of the pores themselves (Whitham and Sparks 1986). Furthermore, only pores which have an open

pathway to the surface of the sample are included in the analysis. Nevertheless, this study highlighted the potential ability of BSDs to reveal the mechanics of degassing.

Many theoretical methods have since been developed which link the BSD with eruption parameters such as the nucleation and growth rates of bubbles, the extent of bubble coalescence, magma ascent rate and volatile supersaturation. These methods, however, remain controversial due to the large number of physical processes which can act to modify the BSD; so far no theoretical model satisfactorily accounts for all these processes. In this chapter I shall begin by summarizing these studies and then describe the results of a new study which incorporates laboratory analogue experiments, numerical modelling and observations of volcanic rocks. This new study reveals that exponential and power law BSDs, both commonly observed in volcanic rocks, may be generated by the same process of continuous bubble nucleation and growth.

2.2.1 Theoretical models of BSD evolution

A sound theoretical basis is required to link eruption parameters quantitatively to BSDs. In response to this need, four distinct models describing the evolution of the BSD during an eruption have been generated. I shall now describe these models in turn, together with examples of studies which have applied them. The symbol $F(R)$ is used to represent the probability density function of the BSD; $F(R)\,\mathrm{d}R$ is then the number of bubbles whose radius lies between R and $R+\mathrm{d}R$.

Technically, the term 'bubble' refers to a void in liquid magma; a void in a solid volcanic rock is known as a *vesicle*. Since this chapter deals with the dynamic processes of magma vesiculation which occur in the liquid state I shall consistently refer only to 'bubble size distributions', even though observations of volcanic rocks strictly yield 'vesicle size distributions'.

Marsh (1988)

Although this model was originally developed to investigate the evolution of crystal size distributions, it has been applied on several occasions to studies of BSDs (Sarda and Graham 1990; Mangan et al. 1993; Klug and Cashman 1994; Burnard 1999). Considering a bubble population in which all bubbles are growing at a constant rate G, the assumption of a steady-state system was made. Under these conditions, the number of bubbles growing into a given size class balances the number of bubbles growing out of that class and the bubble size distribution does not change with time:

$$\frac{\partial F(R)}{\partial t} = 0 \qquad (2.1)$$

The resulting form of $F(R)$ is:

$$F(R) = N_0 \exp\left(-\frac{R}{G\tau}\right) \qquad (2.2)$$

where N_0 is the nucleation density ($F(R) = N_0$ for $R = 0$) and τ is the timescale available for bubble growth. The model therefore predicts an exponential form for the BSD (figure 2.1). The strength of the model lies largely in its convenience; eruption parameters may be calculated very simply. If equation 2.2 holds, a plot of $\ln(F(R))$ against R will be linear with a slope of $-(G\tau)^{-1}$; the growth rate G may therefore be calculated if τ can be estimated. The intercept of the plot on the y-axis is $\ln(N_0)$. The average nucleation rate $J = N_0 G$. The greatest uncertainty associated with this method lies in the estimation of τ, the time available for bubble growth, upon which all other calculations depend. This value is often calculated using models of conduit flow; for example, Klug and Cashman (1994) use the model of Wilson et al. (1980) to derive values of τ between 960 and 4120 s for the May 1980 eruption of Mount St. Helens.

The Marsh (1988) model has been applied in several studies. Sarda and Graham (1990)
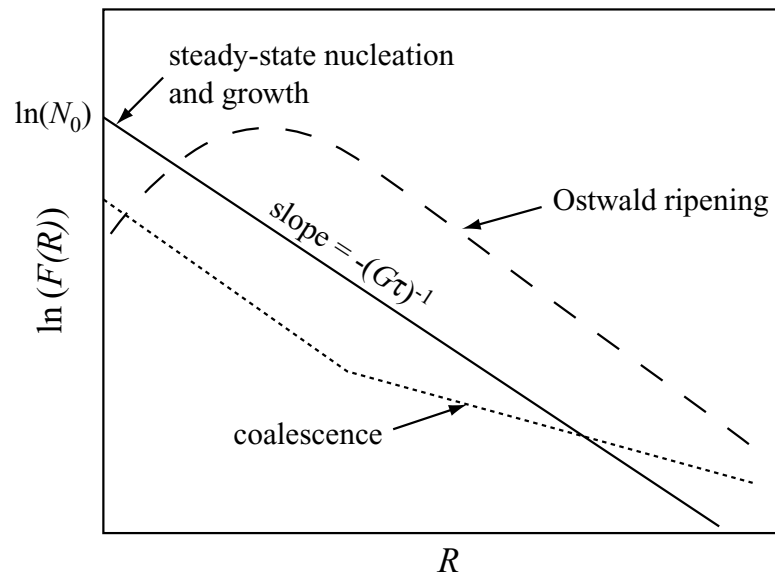
Figure 2.1: Bubble size distributions predicted by the model of Marsh (1988), after Mangan and Cashman (1996). If steady-state nucleation and growth applies (solid line) then a plot of $\ln(F(R))$ vs R is linear with a slope of $-(G\tau)^{-1}$ and intercept of $\ln(N_0)$. Coalescence (dotted line) acts to increase the proportion of bubbles in the large size fractions, whereas Ostwald ripening reduces the number of small bubbles (dashed line). Such BSDs were measured in samples of basaltic scoria and reticulite by Mangan and Cashman (1996).

and Burnard (1999) used it to calculate bubble growth rates from BSDs of popping rocks from the Mid-Atlantic Ridge. Mangan et al. (1993) inferred bubble growth rates of 3.2×10^{-4} cm s^{-1} and nucleation rates of 35.9 cm^{-3} s^{-1} for lavas from Kilauea, Hawai'i. Much lower growth rates ($1.2 - 5.7 \times 10^{-7}$ cm s^{-1}) were estimated by Klug and Cashman (1994) for the May 1980 eruption of Mount St. Helens, consistent with the higher viscosity and slower volatile diffusivity of this dacitic magma compared with typical basalts. Mangan and Cashman (1996) examined samples of basaltic scoria from fire-fountaining episodes of Kilauea. They calculated nucleation rates of $\sim 2 \times 10^4$ cm^{-3} s^{-1}, much greater than those estimated for effusive lava-flow activity (Mangan et al. 1993). This 'runaway' nucleation was interpreted to have been due to the development of a high supersaturation before nucleation, consistent with the more explosive behaviour of the eruption. Calculated bubble growth rates were also enhanced threefold ($\sim 9 \times 10^{-4}$ cm s^{-1}) compared with the effusive estimates.

The main limitation of Marsh's model lies in the assumption of constant bubble nucleation and growth rates. Numerical models of bubble growth due to diffusion and decompression (Sparks 1978; Proussevitch and Sahagian 1996 and chapter 3) reveal that growth rates may be far from constant. Although exponential BSDs of the form of equation 2.2 are commonly observed, many measurements reveal BSDs which deviate strongly from the model. Mangan and Cashman (1996) investigate two processes which cause deviation of the BSD from the form of equation 2.2, namely bubble coalescence and Ostwald ripening. Coalescence increases the proportion of large bubbles and manifests itself as an inflexion in the plot of $\ln(F(R))$ vs R. Ostwald ripening reduces the number of small bubbles in the population, giving a unimodal distribution (figure 2.1).

Toramaru (1989, 1990)

Toramaru's model, first published in 1989 and refined in 1990, takes a very different approach to that of Marsh (1988). The model considers an initial population of bubbles, generated in accordance with classical nucleation theory, which grow through a combination of diffusive mass transfer and expansion in response to a pressure drop. Nucleation is assumed to be homogeneous and to occur in a single event. The pressure drop is assumed to be linear, approximating a constant ascent rate of magma. The bubble growth law is simplified by assuming that the distribution of water concentration around a growing bubble is in steady state. Since bubbles are not created or destroyed after the initial nucleation event, we have:

$$\frac{\partial F(R,t)}{\partial t} + \frac{\partial}{\partial R}\left(v_R F(R,t)\right) = 0 \tag{2.3}$$

(cf. equation 2.1) where v_R is the growth rate of a single bubble and is the sum of the contributions from diffusive and decompressive growth.

Unlike the model of Marsh (1988), Toramaru's model relates the properties of the BSD to tangible physical parameters. He identifies three key parameters: the interfacial surface tension γ which controls the nucleation process, the initial saturation pressure P_0 and the 'effective diffusivity' of water D/U where D is diffusivity and U is the ascent velocity. D/U is a measure of the time available for diffusive growth.

In order to use the model, it is necessary to measure the BSD and calculate its moments. The ith moment M_i of the BSD is given by:

$$M_i = \int R^i F(R)\, \mathrm{d}R \tag{2.4}$$

The first four moments of the BSD are simply related to the total number of bubbles N, the average bubble radius $\bar{R}$, the total surface area per unit volume S and the total bubble

volume per unit volume (i.e. the porosity ϕ):

$$M_0 = N \qquad M_1 = \bar{R}N$$
$$M_2 = \frac{S}{4\pi} \qquad M_3 = \frac{3\phi}{4\pi} \tag{2.5}$$

Toramaru fits the moments of the BSDs to the empirical form

$$M_i \propto \gamma^{a_i} P_0^{b_i} \left(\frac{D}{U}\right)^{c_i} \tag{2.6}$$

where a_i, b_i and c_i are constants, given in Toramaru (1989) and modified in Toramaru (1990). These constants are calculated from experimental or theoretical studies (for example, the value of c_1 is the exponent in the bubble growth law $\bar{R} \propto t^{c_1}$). If three moments are measured, therefore, it appears that the parameters γ, P_0 and D/U could be estimated. However, Toramaru (1990) found that moments M_1 and M_2 are not independent of each other ($M_2 \propto \sqrt{M_1}$) and the third moment M_3 varies little between samples. Hence only two of the three unknown parameters may be calculated.

Toramaru (1990) presents some interesting correlations between the moments of the BSD, the SiO$_2$ content of the melt and the height of the eruption column. Clearly this study represents the basis of a useful, quantitative method of calculating eruption parameters from BSDs. The method, however, is limited by its assumptions of a simplified bubble growth rate, a single nucleation event and a constant ascent velocity. Nevertheless, certain predictions of the model are fulfilled by observations, and Toramaru (1990) claims that this success validates his assumptions regarding nucleation and growth, in particular that bubble coalescence does not appear to modify the observed BSDs significantly. Later in this chapter (section 2.3) I shall present a re-analysis of the data in Toramaru (1990).

Gaonac'h et al. (1996a)

Yet another framework for interpreting BSDs of volcanic rocks was proposed by Gaonac'h et al. (1996a). This work focused on the effects of bubble coalescence, a factor not considered in the analyses of Marsh (1988) and Toramaru (1989, 1990). The BSD evolves by a mechanism of cascading coalescence (figure 2.2). This process is assumed to be scale-invariant and in quasi-steady-state (equation 2.1), giving the relationship

$$F(V) \propto V^{-B-1} \tag{2.7}$$

where V is the bubble volume and B is an exponent. (Note that in this study, the BSD is expressed in terms of bubble volume, not radius.) The two forms are simply related; since $V \propto R^3$, then $F(R) \propto R^{-3(B-1)}$.) The model predicts two regimes; for small bubbles which have not yet been affected by coalescence $B \approx 0$ whereas for medium to large bubbles (the 'coalescence regime') $B \approx 1$. Small bubbles are imagined to grow by diffusion, whereas large bubbles grow by coalescence. Note that whereas the model of Marsh (1988) predicts an exponential form of the BSD, equation 2.7 is a *power law* distribution; this is an important distinction which will form a major part of the discussion in this chapter.

Gaonac'h et al. (1996b) measured BSDs of basaltic lavas from Mount Etna and found that they were in the form of equation 2.7. For small vesicles (with areas less than ~ 0.25 mm^2 in thin section) they obtain $B \approx 0$, in agreement with the model prediction. For larger vesicles $B \approx 0.85$, close to the predicted value of 1.

Herd and Pinkerton (1997)

In this study, BSDs are interpreted in terms of readily measurable textural parameters: porosity ϕ, surface area per unit volume S_v, number density N_v and mean bubble radius $\bar{R}$. Note that ϕ, S_v, N_v and $\bar{R}$ are simply related to the moments of the BSD (equation 2.5).
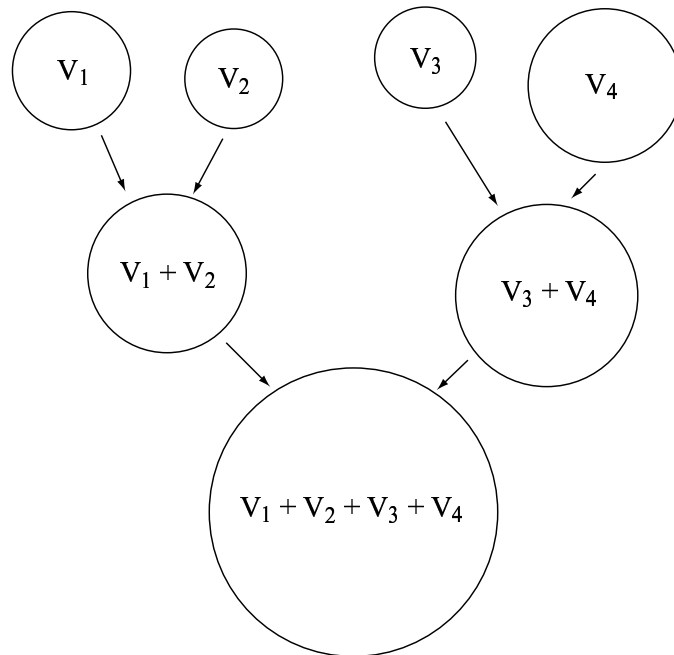
Figure 2.2: A coalescence cascade; V_i is the volume of bubble i. In the model of Gaonac'h et al. (1996a) BSDs evolve by the collision and coalescence of pairs of bubbles.

As with Toramaru (1989, 1990) the exact form of the BSD is not considered. The effects on these factors of vesiculation processes such as bubble nucleation and growth, coalescence and Ostwald ripening are examined. For example, coalescence decreases S_v and N_v but leaves ϕ unchanged. Bubble growth alone increases $\bar{R}$ but the factor $N_v/(1-\phi)$ remains constant. They plotted S_v, N_v and $\bar{R}$ versus ϕ for several samples of basaltic lava to reveal trajectories which were characteristic of the individual vesiculation processes. Their main conclusion was that extensive coalescence occurred in samples with $\phi > 35\%$.

2.2.2   Experimental studies

Experimental studies of degassing of natural or artificial silicate melts have revealed many important features of the dynamics of bubble nucleation and growth (e.g. Lyakhovsky et al. 1996; Mourtada-Bonnefoi and Laporte 1999; Gardner et al. 1999; Liu and Zhang 2000; Mangan and Sisson 2000). Generally speaking, however, these experiments do not

reproduce the bubble size distributions of natural samples. Usually, a single nucleation event occurs in the experiments and interactions between bubbles are limited, leading to a monodisperse or unimodal BSD (e.g. Lyakhovsky et al. 1996, Gardner et al. 1999).

One exception, however, is the study of Simakin et al. (1999). In their experiments, water-saturated granitic melts were decompressed, causing simultaneous vesiculation and crystallization. BSDs of the experimental samples were compared with those of basaltic scoria from Mount Etna and pumice from Vulcano. Power law BSDs were measured; on combining all the data, the relationship $F(R) \propto R^{-1.8}$ was revealed. It was noted that coalescence took place in only two of the experimental runs. Some mechanism other than that of Gaonac'h et al. (1996a) must have led to the formation of power law BSDs. The answer lies in the nucleation behaviour in the experiments. Whereas most previous laboratory experiments generate a single episode of nucleation in response to decompression (e.g. Lyakhovsky et al. 1996), Simakin et al. report that nucleation proceeded in a *continuous* fashion in their experiments. The presence of crystals probably promoted heterogeneous nucleation; previous studies were performed with crystal-free melt and so nucleation would have been more difficult. This mechanism of generating power law BSDs via continuous nucleation will form the crux of the arguments in this chapter.

2.2.3 Stereology

Currently, the most widely-used method for measuring the BSD of a volcanic rock is image analysis (Toramaru 1990; Mangan and Cashman 1993; Klug and Cashman 1994; Mangan and Cashman 1996; Gaonac'h et al. 1996b; Simakin et al. 1999). A thin section (or equivalent) of the rock is made and the resulting slices through the bubbles are analyzed. It is common to measure the apparent area A of each bubble on the image and convert this to an equivalent circular radius r ($= \sqrt{A/\pi}$). The task is to deduce the true size distribution $F(R)$ of three-dimensional bubbles from the measured two-dimensional distribution $f(r)$

of apparent circle radii; this is the problem of *stereology*.

Appendix A describes a method by which the expected distribution of two-dimensional slices may be calculated from a known three-dimensional distribution. Of course, this is the reverse of the problem faced by those who wish to measure BSDs. We shall see in this chapter, however, that the forward-modelling approach in appendix A is still useful.

If the BSD is monodisperse (i.e. all the bubbles are of the same size) then the problem is trivial. The average radius of the circular slices in thin section is $\bar{r} = (\pi/4)R \approx 0.785R$ where R is the true radius of the bubbles (appendix A). (Note that the expression $\bar{r} = 0.85R \Rightarrow R = 1.18\bar{r}$ in Mangan et al. 1993 is incorrect and probably a typographical error; the result in Cashman and Marsh, 1988 is correct.)

For the general case of a polydisperse BSD the problem is very much more complex. To illustrate this, imagine that we have measured a bubble whose apparent radius in thin section is 1 mm. This could have arisen by slicing through any bubble whose radius is greater than or equal to 1 mm. Sahagian and Proussevitch (1998) have, in my opinion, developed the clearest and most flexible stereological method. They consider the general polydisperse BSD to be the sum of many monodisperse distributions. Their figure 3 clearly summarizes the formulation. They also extend their method to deal with non-spherical objects such as ellipsoids, cubes and parallelepipeds. Although the approach of Sahagian and Proussevitch (1998) is general and powerful, it is rather unwieldy; unfortunately this is a characteristic problem of all stereological methods.

In this chapter, the problem is circumvented; most of the BSDs I shall measure are in the form of a power law. This greatly simplifies the stereological method. Appendix A shows that if bubbles are spherical and the true BSD is in the form of a power law of the form $F(R) \propto R^{-\alpha}$ then the two-dimensional distribution of circle slices is of the form $f(r) \propto r^{-(\alpha-1)}$. Therefore the exponent α of the three-dimensional distribution is simply one greater than the exponent of the measured two-dimensional distribution (this result

was also found by Gaonac'h et al., 1996b).

2.2.4 Power law BSDs and their properties

Power law size distributions are described by the relationship

$$N(R) \propto R^{-(d+1)} \Rightarrow N(> R) \propto R^{-d} \tag{2.8}$$

where $N(R)$ is the number of objects of a size (radius) R, $N(> R)$ is the number of objects with a radius greater than R, and d is the power law exponent. In this chapter the cumulative form of equation 2.8, i.e. $N(> R)$ versus R, is used to express power law BSDs. This gives a more accurate estimate of d as it does not require the data to be binned, which can cause large uncertainties in the calculation of the exponent.

Power law distributions, unlike unimodal or exponential BSDs (equations 2.9 and 2.10), have no characteristic length scale and so no average bubble size in the population. If the exponent d is between 2 and 3 (typical for volcanic rocks as we shall see) then the total volume of the bubbles is controlled mostly by the large bubbles, but the total surface area is controlled by the smallest size fractions (Turcotte 1992). It is therefore impossible to approximate successfully both diffusive bubble growth (surface area controlled) and decompressive growth (volume controlled) by assuming a monodisperse distribution.

Note that for everything except mathematical fractals, the power law form is only valid for a range of bubble sizes; for the largest and smallest bubbles in a population the power law fit does not in general apply.

2.2.5 Exponential and power law BSDs

The studies so far have mainly reported BSDs in two forms: exponential (as predicted by the Marsh 1988 model) and power law (as predicted by Gaonac'h et al. 1996a). The different distributions have been explained by two distinct mechanisms, namely steady-state nucleation and growth and cascading coalescence. It is often practically difficult to distinguish reliably the two forms of BSD with real data— the BSD may be fitted well by either model (section 2.4.3). The manner in which the data are separated into size classes to produce a histogram can also have a large influence on the apparent form of the BSD.

In this chapter, I shall describe the formulation of a new model which relates BSDs to eruption processes. This model is distinct from all those so far discussed, and has the important feature that it can explain the generation of *both* exponential and power law BSDs with the same physical mechanism, that of continuous bubble nucleation. The reader is also referred to Blower et al. (2001), in which the main findings of this chapter are published.

2.3 BSDs of volcanic rocks

We have seen that Gaonac'h et al. (1996b) have measured power law BSDs in basaltic lavas and that Simakin et al. (1999) investigated scoria from Etna and pumice from Vulcano and also discovered power law distributions. A re-analysis of the images in figure 1b of Toramaru (1990) reveals power law BSDs in scoria samples from a basaltic sub-Plinian eruption of Izu-Oshima, Japan (table 2.1). The BSDs of pumices from the same figure were found to be generally better described by an exponential distribution.

Recent, unpublished data (kindly supplied by Dr Ian Wright of the National Institute of Water and Atmospheric Research, Wellington, New Zealand) reveal power law BSDs in samples of pumice from the Healy submarine volcano, Southern Kermadec arc, SW

Image	rock type	R^2 (power law)	R^2 (exponential)	form of BSD
a	pumice	0.87	0.92	exponential
c	pumice	0.84	0.97	exponential
d	pumice	0.81	0.98	exponential
e	pumice	0.85	0.75	inconclusive
f	pumice	0.91	0.89	inconclusive
g	pumice	0.66	0.90	exponential
h	scoria	0.94	0.68	power law ($d \sim 2.5$)
i	scoria	0.67	0.95	exponential
j	scoria	0.92	0.67	power law ($d \sim 2.5$)
k	scoria	0.94	0.65	power law ($d \sim 2.5$)

Table 2.1: BSD analysis of images from figure 1b of Toramaru (1990). Pumice samples came from Towada volcano and scoria samples originated from a basaltic sub-Plinian eruption of Izu-Oshima. The fit of the BSDs to both an exponential and power law form was investigated; the correlation coefficient R^2 is given in each case. If the values of R^2 are similar (within 0.03) or if they are both less than 0.90 then the analysis was deemed to give an inconclusive result. The scoria samples generally displayed power law BSDs, all with exponents close to 2.5, with one exception (sample i). The pumice samples gave exponential BSDs except for two (e and f) for which the BSD was well-fitted by neither an exponential nor a power law form. It is important to note that both exponential and power law BSDs have originated from the same eruption.

Pacific (figure 2.3). The data in fact show two power laws, one for small bubbles and one for larger ones. These data are of very high quality, representing the largest number (2242) of bubbles analyzed in a single sample that I have seen so far. This allows the form of the BSD to be tightly constrained, at least for the smaller bubbles. Note that the form of this graph shows the reverse trend of that predicted by Gaonac'h et al. (1996a). They also predict two power laws, but in their model, the power law describing the small bubbles has an exponent *smaller* than that describing the large bubbles.

2.4 BSDs of foam from analogue experiments

I have discussed (section 2.2.2) that experimental studies of the degassing of silicate melts (natural or synthetic) rarely reproduce the bubble size distributions of volcanic tephra. An avenue which has yet to be explored is the examination of BSDs generated in *analogue*
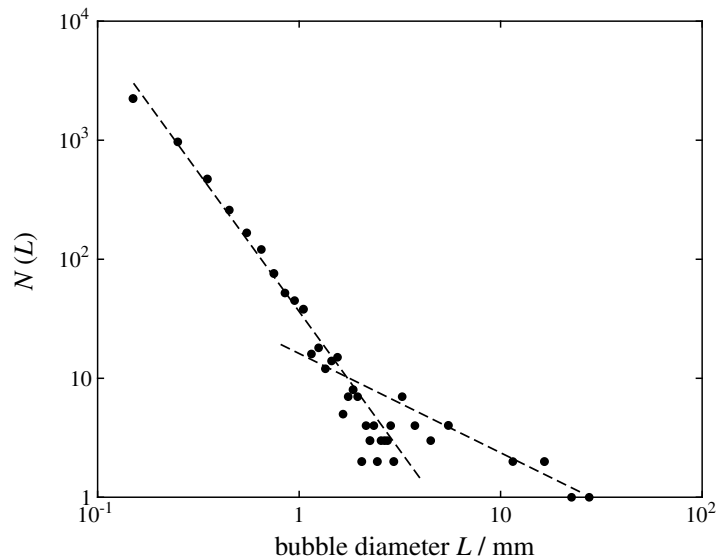
Figure 2.3: BSD of pumice from the Healy submarine volcano, SW Pacific (I.C. Wright, unpublished data). This is a histogram (N.B. not a cumulative histogram) of apparent bubble diameters in a thin section. The data are described by two power laws, one for bubbles with diameters less than ~ 1 mm ($d = 2.5$), and one for bubbles with diameters greater than ~ 3 mm ($d = 0.8$) (Regression lines provided by I.C. Wright.) The data are widely scattered near the intersection of the two regression lines. It is not clear how the data in this region can be interpreted as they lie *below* both regression lines. Perhaps the power law describing the large bubbles should have a shallower slope.

experiments. Many laboratory analogue systems have been devised to investigate the dynamics of explosive two-phase flows. These include the explosive boiling of freon liquids (Hill and Sturtevant 1989; Hill 1991), the rapid exsolution of CO_2 from aqueous solution (Mader et al. 1994, 1997; Zhang et al. 1997) and the reaction of concentrated acid and carbonate solutions (Mader et al. 1994; Mader et al. 1996). Although these experiments have revealed valuable information about the dynamics of vapour-driven flows, none of these systems are suitable for the study of foam textures as they do not produce a solid end-product.

2.4.1   The gum rosin/acetone analogue system

The only current analogue system capable of generating solid foam through explosive degassing is the gum rosin and acetone (GRA) system. First presented by Phillips et al. (1995), this system has many important features which ensure its suitability for modelling volcanic degassing processes:

- In common with the above analogue systems, GRA solutions are workable under laboratory temperatures and pressures; experiments can therefore be conducted in glass tubes and the rapidly-evolving flows which are generated can be recorded and analyzed using high-speed video cameras. The physical properties of GRA solutions are detailed in appendix B.

- Solutions of gum rosin in acetone are Newtonian viscous liquids whose viscosity is strongly dependent on their acetone content (figure 2.4 and appendix B), mimicking the analogous dependence of magma viscosity on its water content. During degassing, therefore, the liquid viscosity increases through several orders of magnitude: at 30 wt.% acetone the viscosity of the liquid is 0.04 Pa s (appendix B); pure, degassed gum rosin has a viscosity of $\sim 10^{13}$ Pa s (Phillips et al. 1995). This large viscosity increase exerts a strong control on the flow dynamics during degassing

(Mourtada-Bonnefoi and Mader 2001). In contrast, the analogue systems mentioned above mostly employ aqueous liquids of very low viscosity (the viscosity of water is 10^{-3} Pa s). Zhang et al. (1997) used solutions of carbonated water in which they dissolved various polymers to increase their viscosity. Liquids with viscosities of 0.005 to 0.7 Pa s were created in this way. The viscosity of the liquid was not dependent on the volatile (CO_2) content.

- The diffusivity of acetone in GRA solutions is of the order 10^{-11} m^2 s^{-1}, similar to measured diffusivities of water in hydrated magmas (Watson 1994; Zhang and Behrens 2000) and is dependent on the concentration of acetone (appendix B), just as the diffusivity of water in magma is concentration-dependent (Zhang and Behrens 2000).

- In terms of the study described in this chapter, the most important property of the GRA system is that, once degassing is complete, a solid gum rosin foam is produced. Figure 2.5 illustrates that, to casual inspection at least, the gum rosin foam appears texturally very similar to pumices derived from explosive volcanic eruptions. I shall show in this chapter that the BSDs of the artificial foam are also very similar to those of volcanic tephra.

2.4.2   Experimental procedure

Experiments are performed in a standard shock-tube apparatus (figure 2.6). GRA solutions are made by dissolving a known mass of gum rosin powder in a known mass of acetone. The GRA solution is poured into a cylindrical Pyrex test cell of internal diameter 38 mm and length 300 mm. The test cell is bolted to a Pyrex shock tube of length 1 m and the same internal diameter, and the two tubes are separated by a diaphragm which is made of thick plastic tape (Sellotape® all-weather tape of width 50 mm). The shock tube is bolted to a cylindrical vacuum chamber of height 1 m and diameter 0.5 m.
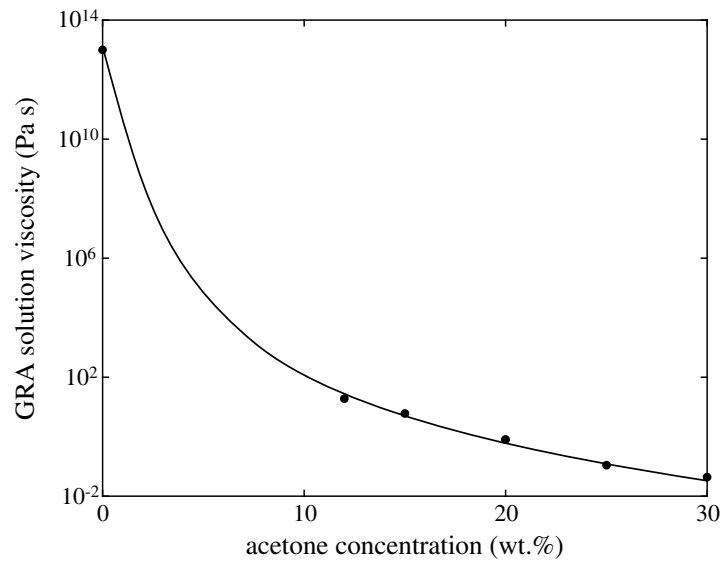
Figure 2.4: The viscosity of GRA solution as a function of its acetone concentration at 20°C. Further details of the measurement of these data are given in appendix B.

The experiments are controlled by two parameters; the initial acetone content of the GRA solution and the pressure in the vacuum chamber. Chamber pressures lower than 200 mbar are required to cause violent degassing on decompression. The initial acetone content controls both the viscosity of the solution and the amount of volatiles available for expansion. The explosivity of the 'eruption' can be increased by increasing the initial acetone content or by decreasing the chamber pressure.

The diaphragm is burst by passing 10 A of current through a length of NiChrome wire attached to the diaphragm around its circumference. The wire heats up rapidly, the plastic tape melts and the pressure differential ruptures the diaphragm all around its circumference. Typically the diaphragm itself is projected up the shock tube and into the vacuum chamber. In this way the GRA solution sample is decompressed in less than 1 ms.

Upon decompression to less than 200 mbar the acetone boils explosively and drives a two-phase flow up the shock-tube. Boiling proceeds as an evaporation wave (Hill and Sturtevant 1989; Hill 1991); bubbles nucleate only on the surface of the solution and this
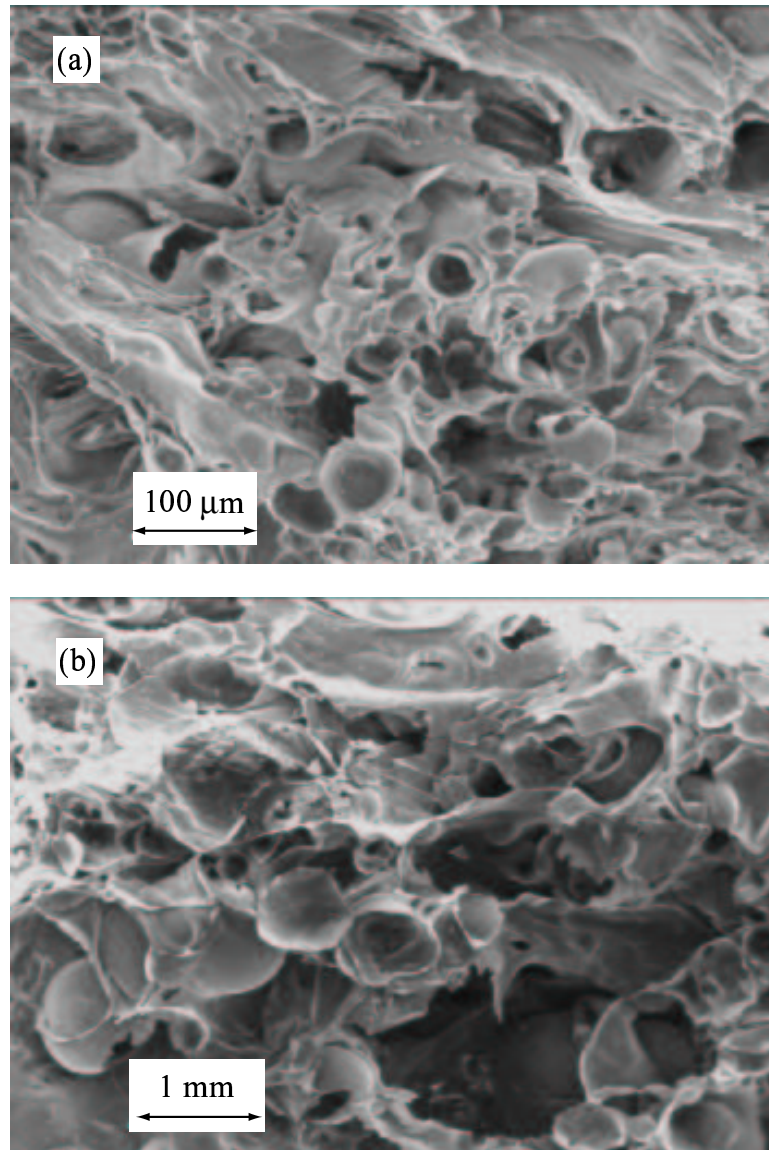
Figure 2.5: SEM images of (a) pumice sample from the Minoan Phase One Plinian eruption of Santorini, Greece and (b) gum rosin foam. Despite the difference in scales, the images are very similar, depicting highly disordered foams with some spherical and some strained bubbles.
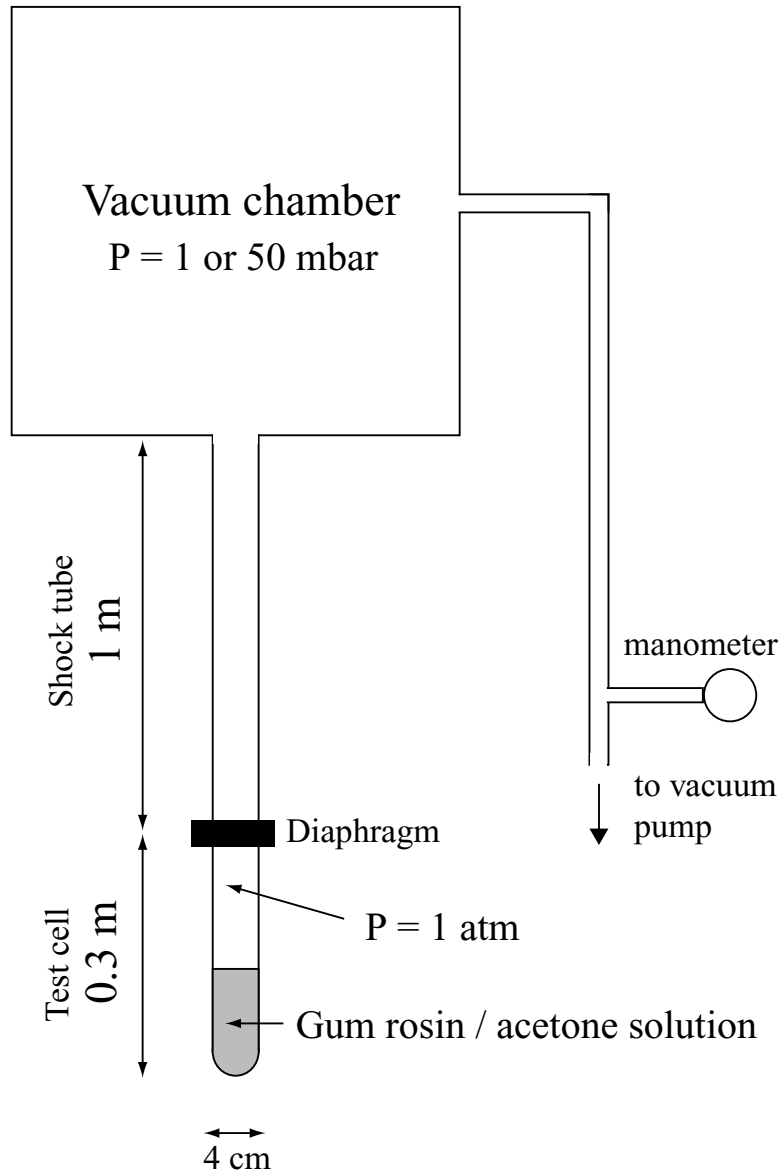
Figure 2.6: Schematic diagram of the apparatus used in the GRA decompression experiments. The boiling of the acetone in the GRA solution is initiated by bursting the diaphragm, decompressing the solution beneath its boiling pressure (~ 200 mbar).
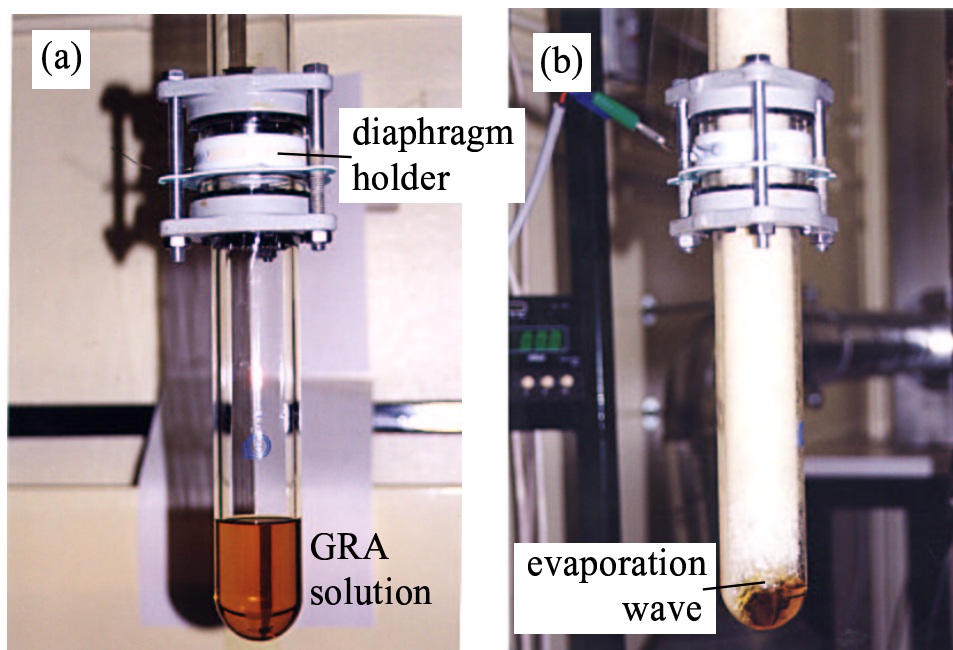
Figure 2.7: The test cell (a) before and (b) during an experiment. Note that nucleation occurs only on the surface of the liquid as an evaporation wave.

nucleation surface propagates downward with time (figure 2.7). The bubbly liquid may fragment, depending on the experimental conditions (figure 2.8).

After the foam has ceased to expand it is left in the shock tube under vacuum until all the acetone has been removed. The bulk vesicularity of the foam is estimated by measuring the final length L_f of the foam from the base of the test cell to the flow front. The vesicularity of the foam is $(L_f - L_0)/L_0$ where L_0 is the initial depth of solution in the test cell. Cores of dry foam are recovered from the shock tube using a stiff wire (figure 2.9). Not all experiments succeed in producing dry foam. If the initial acetone content is less than 20 wt.% then the foam does not become permeable enough to lose all its acetone. For textural analysis the foam must be completely dry.

In order to extract textural data from the cores the following procedure is followed. The gum rosin foam cores are cut into slices around 5 mm thick and 30 mm in diameter using a razor blade and affixed to stiff, white cardboard using PVA glue. The slices
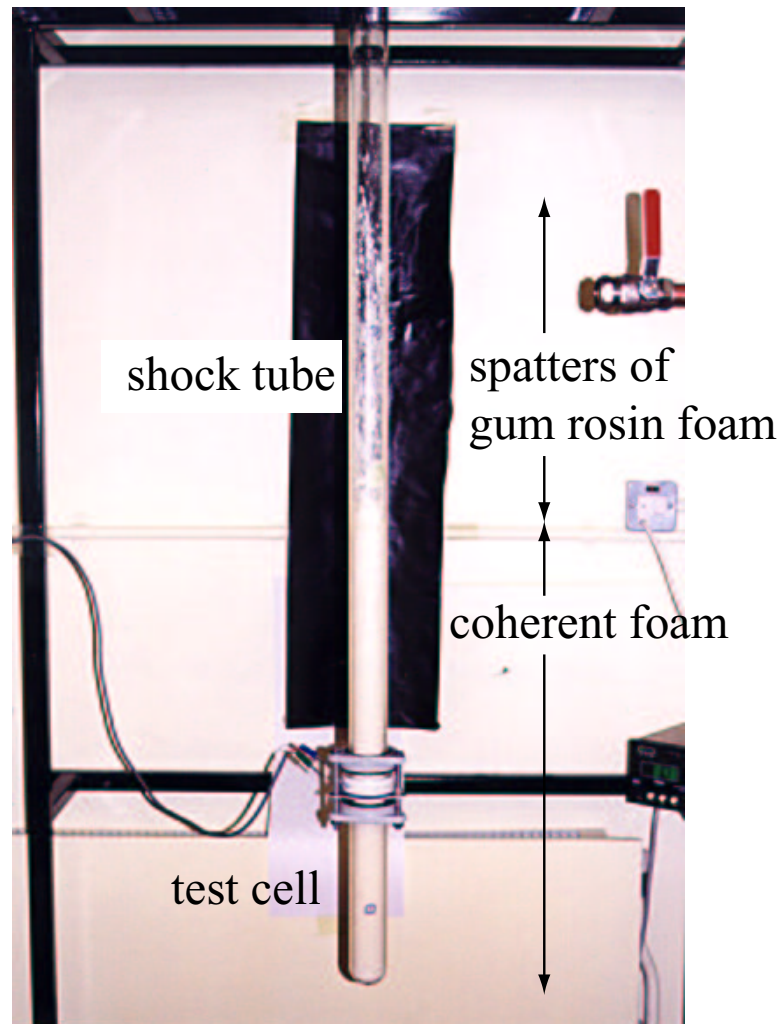
Figure 2.8: The shock tube apparatus after an experiment (initial acetone content=25 wt.%, chamber pressure=1.5 mbar). The test cell and the lower ~ 40 cm of the shock tube are filled with coherent (unfragmented) foam. Above this height the foam has fragmented into spatters which extend to around 20 cm from the top of the shock tube. Different fragmentation styles are observed with different experimental conditions (table 2.2)

Figure 2.9: Cores of gum rosin foam produced in the GRA decompression experiments.

are then placed in a gold sputter coater (normally used for coating samples for scanning electron microscopy) for 30 seconds. This coats the surface of the slice with a thin layer of gold powder which is dark and contrasts visually with the pale, straw-coloured foam, bringing out the shapes of the bubbles. Photographs are taken of the coated slices using monochrome 35 mm film and printed onto A4-sized pieces of high-contrast (grade 4) photographic paper. In this way, images of the slices at a magnification factor of ~ 6 may be generated (figure 2.10). The bubbles in the photographs are traced onto acetate sheets using a thin, black, permanent marker. These hand tracings are scanned into a computer at 150 dots per inch to create binary images suitable for computerized image analysis. The software package Visilog$^{\circledR}$ is used to measure the cross-sectional area A of each bubble in the binary images. The equivalent circular radius r of each bubble is then calculated ($r = \sqrt{A/\pi}$).

Note that it was not found to be possible to impregnate the foam to increase its strength and allow the production of a thin section. The foam is highly soluble in all organic solvents (including alcohols) and therefore standard low-viscosity resins could not be used. Water-
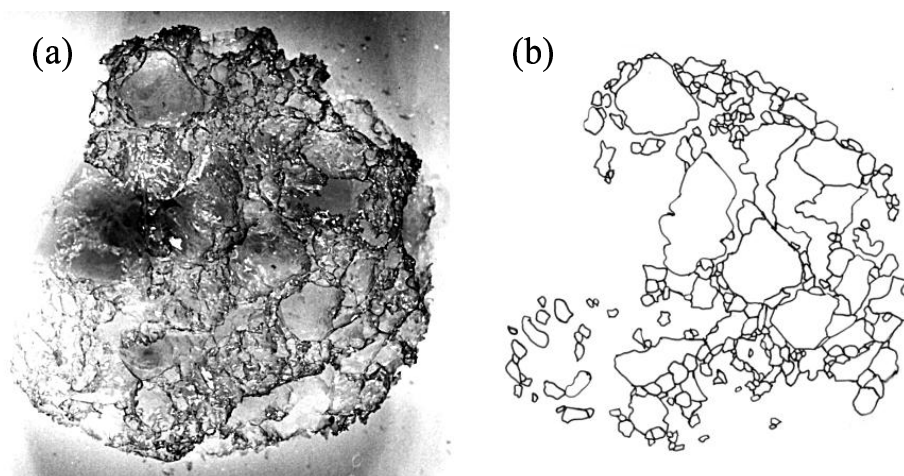
Figure 2.10: A slice of gum rosin foam, taken from an experiment in which the initial acetone content was 25 wt.% and the chamber pressure was 1 mbar. (a) Image of the slice after partial coating using a gold sputter coater for 30 seconds; (b) Hand tracing of the image. Width of each image is 3 cm. Note that due to the extreme fragility of the foam many bubble walls have broken during the sectioning process and could not be traced. The hand tracing (b) is scanned into a computer for image analysis.

based resins were found to be too viscous, and the surface tension of water too high, to impregnate the foams successfully; furthermore the drying time of these water-based resins was found to be extremely long (several days to weeks).

2.4.3 Results

In order to generate foam from a wide range of experimental conditions, a series of GRA decompression experiments were performed with a range of initial acetone contents (20, 25 and 30 wt.%) and chamber pressures (1 and 50 mbar). Foam from six of these experiments was successfully recovered and analyzed. The experimental conditions, foam vesicularities and fragmentation behaviour are summarized in table 2.2.

A total of 18 foam slices were made from the foam produced in these experiments; 6 for each set of experimental conditions. The binary images of the foam slices and their bubble size distributions are shown in figures 2.11, 2.12 and 2.13. In the calculation of the BSD,

Run #	Initial acetone content / wt.%	Chamber pressure / mbar	Foam vesicularity (%)	Fragmentation style
1	30	1.2	89	fragments/spatters
2	30	1.0	89	fragments/spatters
3	25	1.2	91	spatters
4	25	1.0	92	spatters
5	20	50	93	no fragmentation
6	20	50	93	no fragmentation

Table 2.2: Summary of experimental conditions results from the GRA explosive degassing experiments. No fragmentation was observed in experiments 5 and 6. In experiments 3 and 4 the liquid fragmented into 'spatters'— small elongate droplets of bubbly liquid which adhered to the tube walls. Experiments 1 and 2 generated both spatters and fragments; 'fragments' are lapilli-sized (1-2 cm in diameter) sub-equant sections of foam which have separated from the main flow.

only bubbles with an area greater than 0.1 mm^2 were used; bubbles smaller than this could not be resolved accurately on the images. Only values of $N(> A)$ greater than 5 were included to ensure that each size class in the analysis was adequately represented.

In figures 2.11, 2.12 and 2.13 the power law distributions are expressed in terms of bubble area, $N(> A) \propto A^{-\lambda}$. Since $A \propto r^2$, the distribution of equivalent circle radii is $N(> r) \propto r^{-2\lambda}$. We have seen that the exponent of the three-dimensional distribution of bubbles is one greater than that of the two-dimensional distribution of equivalent circle radii (section 2.2.3). Therefore $N(> R) \propto R^{(-2\lambda+1)}$, i.e. the power law exponent $d = 2\lambda+1$. The error on d is difficult to constrain accurately. Some indication of the error can be gained by a bootstrapping method, in which random points from the BSD plot are removed to see how the best fit curve is affected. By this method, the error on the exponent λ was found to be around ± 0.1, giving an error on d of $\sim \pm 0.2$.

The results of the analysis are summarized in table 2.3.
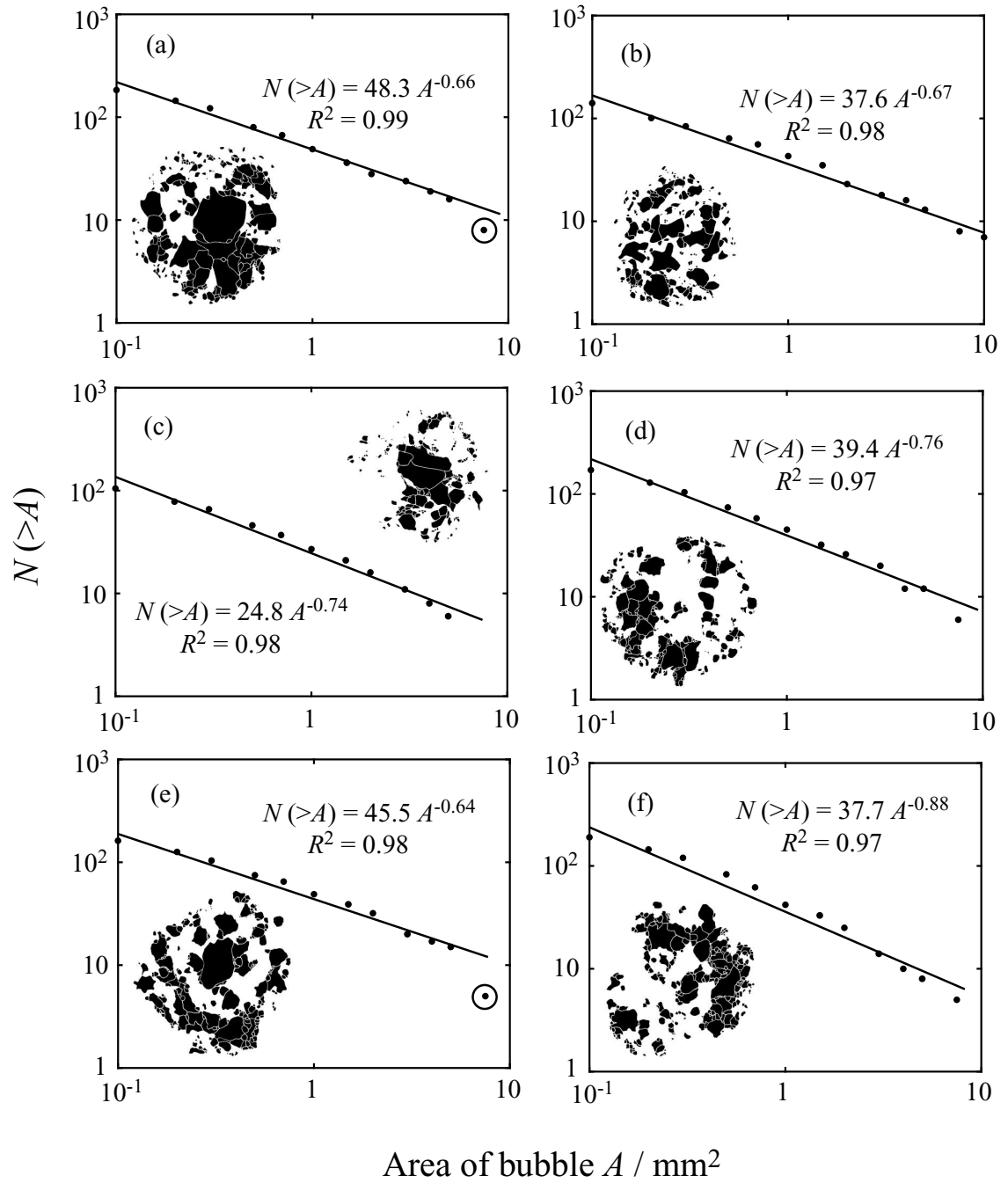
Figure 2.11: Bubble size distributions of 6 samples from experiments with an initial acetone content of 20 wt.% and a chamber pressure of 50 mbar. Samples (a), (b) and (c) are from run 5 (table 2.2) and samples (d), (e) and (f) are from run 6. The binary images of the samples are also shown. All 6 BSDs are well fit by a power law distribution. Circled points were not included in the calculation of the best fit power law distribution.
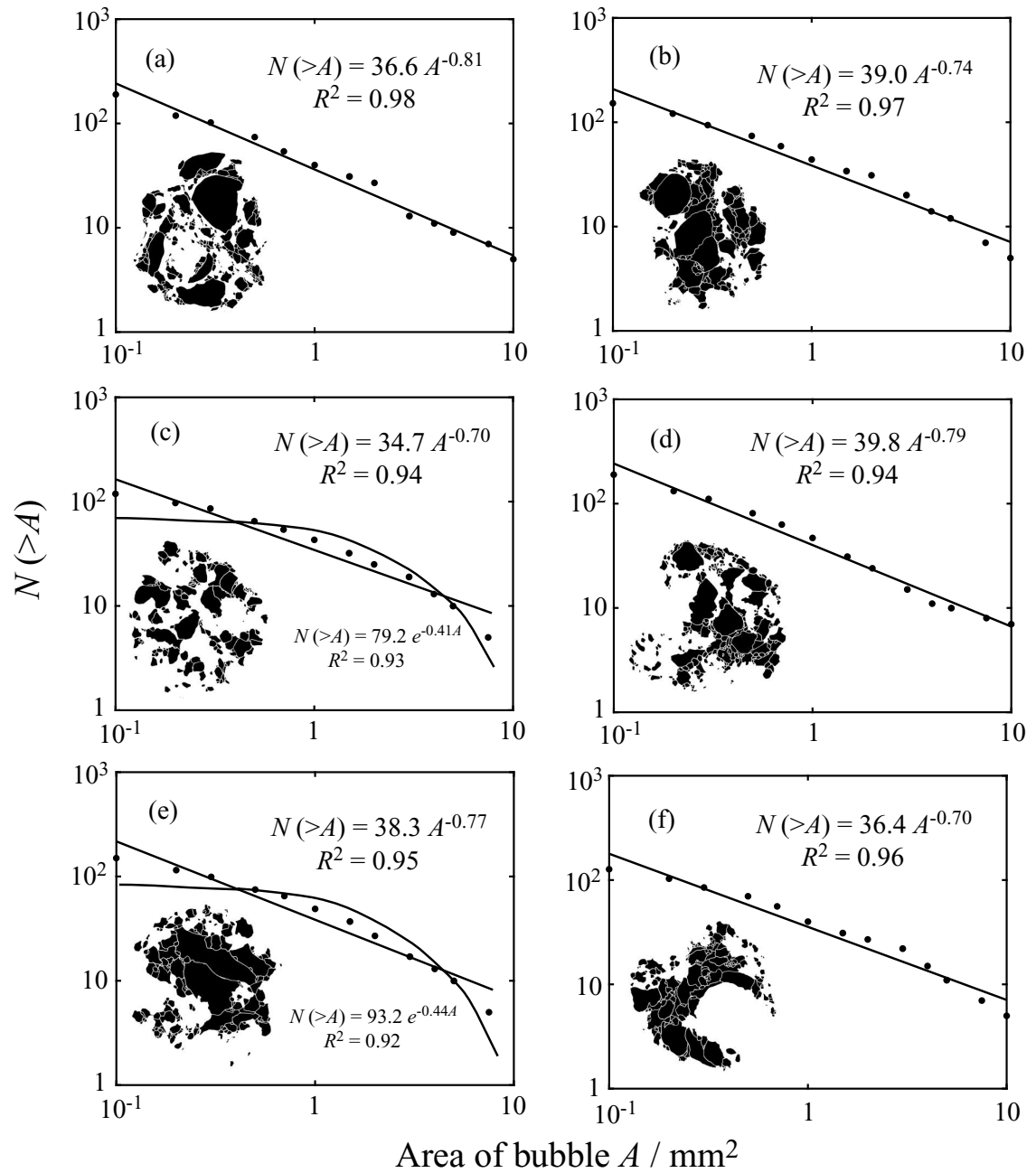
Figure 2.12: Bubble size distributions of 6 samples from experiments with an initial acetone content of 25 wt.% and a chamber pressure of 1 mbar. Samples (a), (b) and (c) are from run 3 (table 2.2) and samples (d), (e) and (f) are from run 4. The binary images of the samples are also shown. All 6 BSDs are well fit by a power law distribution, but the fit of the BSDs of samples (c) and (e) to an exponential distribution is also reasonable.
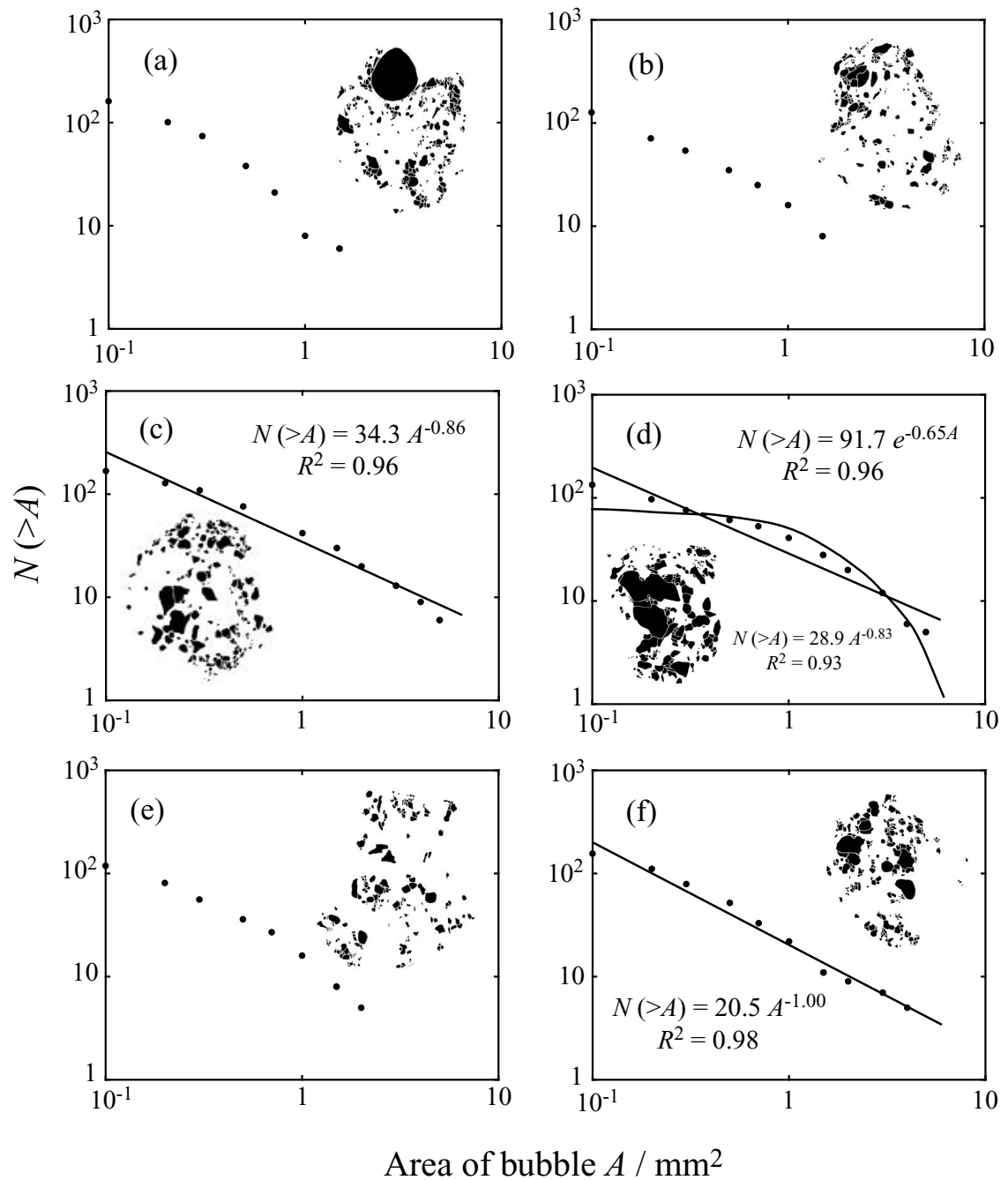
Figure 2.13: Bubble size distributions of 6 samples from experiments with an initial acetone content of 30 wt.% and a chamber pressure of 1 mbar. Samples (a) and (b) are from run 1 (table 2.2) and samples (c), (d), (e) and (f) are from run 2. The binary images of the samples are also shown. The BSDs of samples (c) and (e) are well fit by a power law distribution. The BSD of sample (d) was better fit by an exponential distribution. The images of samples (a), (b) and (f) were judged to be inadequate for the reliable determination of a BSD. The highly explosive nature of the experiments appears to have led to the production of an extremely fragile foam and many bubble walls were broken on sectioning.

Figure	Sample	R^2 (power law)	R^2 (exponential)	form of distribution	power law exponent d
2.11	(a)	0.99	0.83	power law	2.3
2.11	(b)	0.98	0.83	power law	2.3
2.11	(c)	0.98	0.90	power law	2.5
2.11	(d)	0.97	0.87	power law	2.5
2.11	(e)	0.98	0.90	power law	2.3
2.11	(f)	0.97	0.87	power law	2.8
2.12	(a)	0.98	0.80	power law	2.6
2.12	(b)	0.97	0.88	power law	2.5
2.12	(c)	0.94	0.93	(power law)	(2.4)
2.12	(d)	0.98	0.76	power law	2.6
2.12	(e)	0.94	0.92	(power law)	(2.5)
2.12	(f)	0.96	0.89	power law	2.4
2.13	(c)	0.96	0.92	power law	2.7
2.13	(d)	0.93	0.96	(exponential)	N/A
2.13	(f)	0.98	0.83	power law	3.0

Table 2.3: Summary of results of the BSD analysis of the gum rosin foam. For each sample the correlation coefficients (R^2) are shown for both a power law and an exponential fit. For distributions which are well fit by a power law distribution the power law exponent d is calculated, with an estimated error of ± 0.2. There is no systematic variation of d with experimental conditions; the differences between the exponents are comparable to the error on the exponent. It can be seen that in most cases a power law distribution gives a much better fit to the data than does an exponential distribution. Brackets denote that the form of the distribution is uncertain, i.e. that the correlation coefficients for power law and exponential fits are similar (within 0.03).

2.5 Modelling the generation of power law BSDs

We have seen that bubble size distributions of experimentally-generated foam and volcanic rocks of many different types are often in the form of a power law. The work of Gaonac'h et al. (1996a) suggested that a mechanism of cascading coalescence could account for the form of these BSDs. However, in the experiments of Simakin et al. (1999) power law BSDs were generated in the *absence* of bubble coalescence.

The subject of the remainder of this chapter is the development of a model which attributes the formation of power law BSDs to nucleation behaviour, not coalescence. The basis of the model is that nucleation is imagined to proceed in a continuous fashion (as in the experiments of Simakin et al., 1999), simultaneous with growth. Bubbles nucleate and grow in response to decompression. As magma ascends through the conduit it is decompressed still further and bubbles continue to nucleate in the pockets of melt between existing bubbles. I shall demonstrate that this simple mechanism can generate both exponential and power law BSDs.

2.5.1 The Apollonian packing

The mechanism of continuous nucleation and growth may be taken to its logical extreme to generate a geometric figure known as the *Apollonian packing*. This is constructed by drawing three equal, mutually tangential circles and then filling the curved triangular space in between them with ever-smaller circles (figure 2.14a). The circle size distribution is in the form of a power law with a well-constrained exponent d of 1.312 (figure 2.14b). The analogous three-dimensional figure (a packing of spheres) has $d \sim 2.45$ (Anishchik and Medvedev 1995). One can imagine readily that these spheres might be bubbles which have nucleated between pre-existing bubbles; in this way the bubbles pack efficiently and fill space.
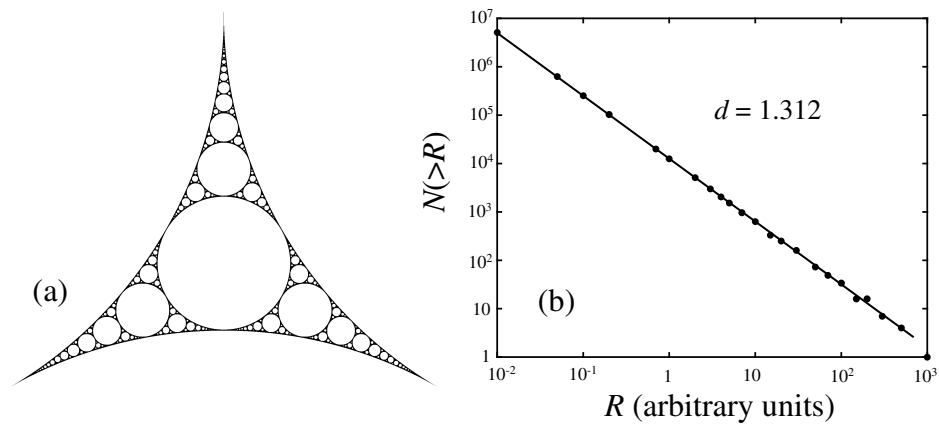
Figure 2.14: The Apollonian packing. (a) Starting with three large, touching circles, space is progressively filled with ever-smaller circles. If this procedure is continued *ad infinitum* then a space-filling fractal is created with no overlap between circles. (b) The distribution of circle sizes in the packing.

The Apollonian packing has found application particularly in the science of granular materials; it is by definition the densest possible packing of circles/spheres. In volcanological terms, the three-dimensional packing represents a hypothetical pumice with 100% porosity and zero permeability— this highlights the important control of the spatial arrangement of bubbles on magma permeability (chapter 4).

2.5.2 Developing the model

Although the Apollonian packing represents a useful paradigm, it cannot in itself reveal information about degassing processes. The numerical model which will now be developed investigates the process of space-filling nucleation and growth in a more volcanologically realistic context. The model contains many simplifications, but serves to highlight the potential of the mechanism for generating the observed BSDs. It will be shown that some of these assumptions (such as a simplified bubble growth law) have little effect on the major conclusions of the study. Like the permeability model in chapter 4 the basis of the model is geometric. It does not, for example, consider the dynamics of bubble nucleation

or growth, and is not constrained by timescales. The geometric nature of the model is not necessarily a weakness. On the contrary the formulation allows results to be revealed which are *independent* of the detailed dynamics of the degassing process.

The model works as follows: A small number of bubble nuclei are placed at random positions within a three dimensional domain. These bubbles are allowed to grow according to a parabolic (diffusional) growth law, $R = \beta t^{1/2}$ (Scriven, 1959). The growth constant β is proportional to the size of the 'zone of influence' of the bubble, i.e. the set of points which are closer to the bubble in question than to any other bubble (the *Voronoi volume*). Thus, bubbles which are relatively isolated grow more rapidly than those which must compete with near neighbours for volatile resources. This growth law is clearly a simplification; in the early stages of growth bubbles feel no influence from their neighbours and so would probably be expected to grow at the same rate. We shall see later, however, that the form of the growth law has little effect on the results. Each successive generation of bubbles nucleates as far as possible from the existing bubbles, at the vertices between Voronoi volumes. These are the locations where the volatile resources are least depleted and hence represent the most favourable locations for nucleation (Lyakhovsky et al. 1996). This behaviour is summarized in figure 2.15. Each addition of a new generation of bubbles is termed a nucleation 'event'. The model uses discrete nucleation events as an approximation to continuous nucleation.

If two bubbles touch, they cease to grow. This highly artificial condition was employed to avoid problems of bubble overlap and to prevent bubble coalescence. This constraint is not as unrealistic as it first appears. Since the bubbles are constrained to nucleate as far from each other as possible, they do not begin to touch until late in their evolution, when they would be expected to be approaching their final radius anyway.
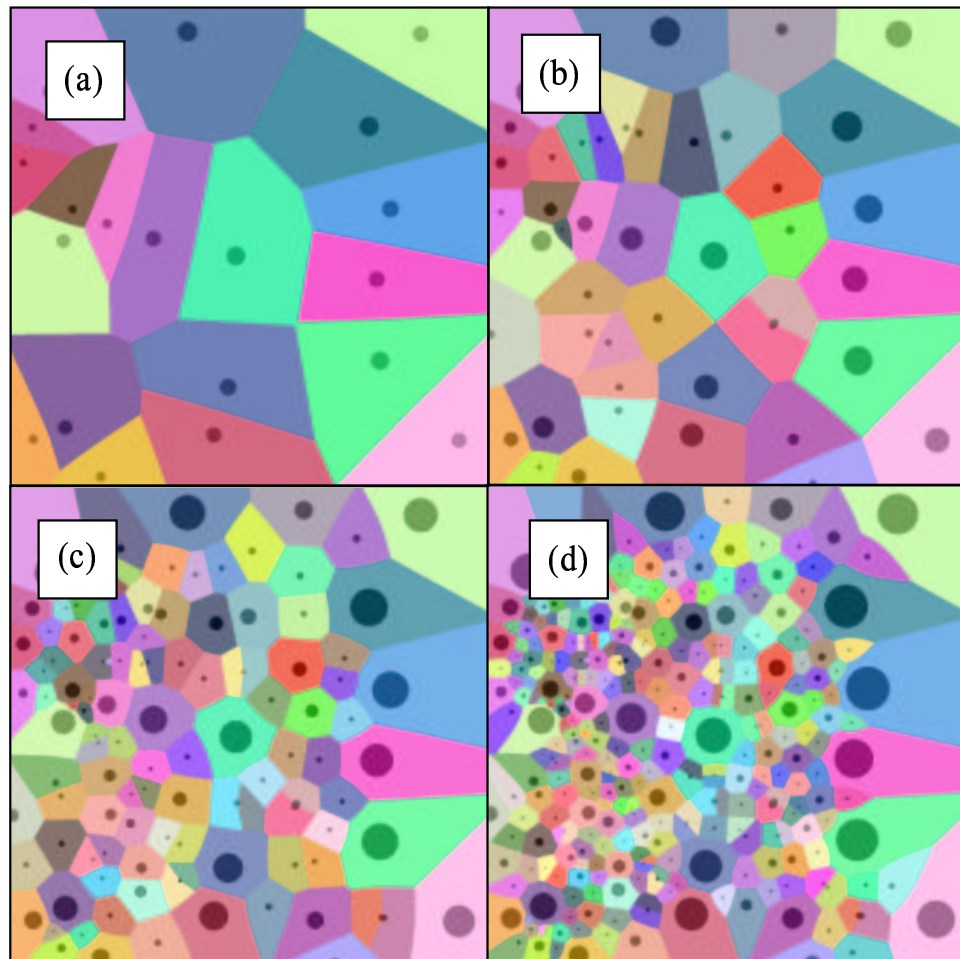
Figure 2.15: The construction of the numerical model. For illustrative purposes this diagram shows the results of a two-dimensional version of the model. (a) The initial nucleation event. The bubbles have been allowed to grow by a small amount. The shades of grey represent the Voronoi volumes of each bubble. (b) The second generation of bubbles have nucleated at the vertices between the Voronoi volumes in the first picture. The Voronoi volumes have been recalculated. (c) and (d) Two more stages in the evolution of the bubble distribution.

2.6   Results of the numerical model

The main result of the model is that the form of the BSD depends most strongly on the number of nucleation events which occur during growth. If there is only one nucleation event a unimodal BSD results (figure 2.16). Because of the dependence of the growth rate β on the Voronoi volume, the size of each bubble depends on the proximity of its neighbours. Under the simplifying assumption that the final bubble size is proportional to the distance to the nearest bubble, a Poisson distribution is expected (Tuckwell 1988):

$$N(R) \propto R^2 \exp(-\lambda R^3) \Rightarrow N(> R) \propto \exp(-\lambda R^3) \qquad (2.9)$$

where λ is a constant related to the number density of bubble nuclei. A Poisson distribution is a near-symmetric unimodal distribution which is close in appearance to a Gaussian (normal) distribution.

After a small number (around 3) nucleation events have occurred, an exponential BSD emerges (figure 2.16):

$$N(R) \propto \exp(-R/R_0) \Rightarrow N(> R) \propto \exp(-R/R_0) \qquad (2.10)$$

(cf. equation 2.2) where R_0 is a characteristic bubble size. Note that the model predicts exponential BSDs without the assumptions of a steady-state BSD or a constant bubble growth rate (cf. Marsh 1988). In the model exponential BSDs always evolve into power law distributions (equation 2.8) with further nucleation events. After a total of 5 events the distribution is consistently power law (figure 2.16). As more nucleation events occur, the distribution remains in the form of a power law, but the exponent d increases with the number of events (figure 2.17).
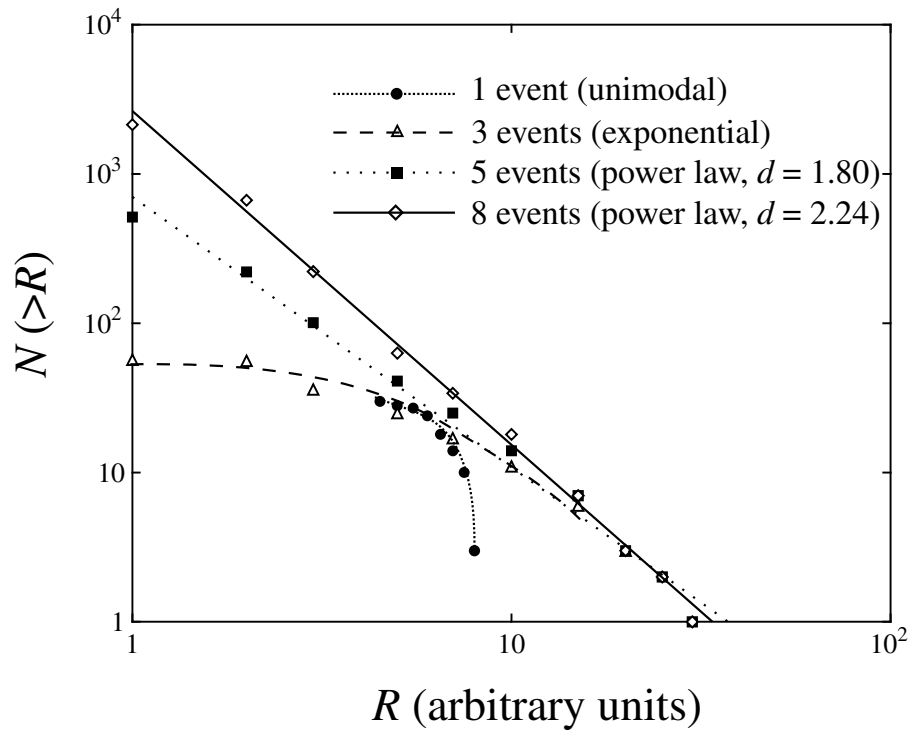
Figure 2.16: Results of a typical model run. Note that the number of bubbles with a radius greater than R are plotted against R on double-logarithmic axes and so some of the BSDs appear unfamiliar. A single nucleation event gives a unimodal BSD. After 3 events the BSD has taken an exponential form (with correlation coefficient 0.97). 5 events give a power law BSD with exponent $d = 1.80$ (with correlation coefficient 0.99) and after 8 events the BSD is still in the form of a power law but the exponent has increased to 2.24 (with correlation coefficient 0.99) . The BSD is evolving throughout the model run and is therefore not in steady state (cf. Marsh, 1988).
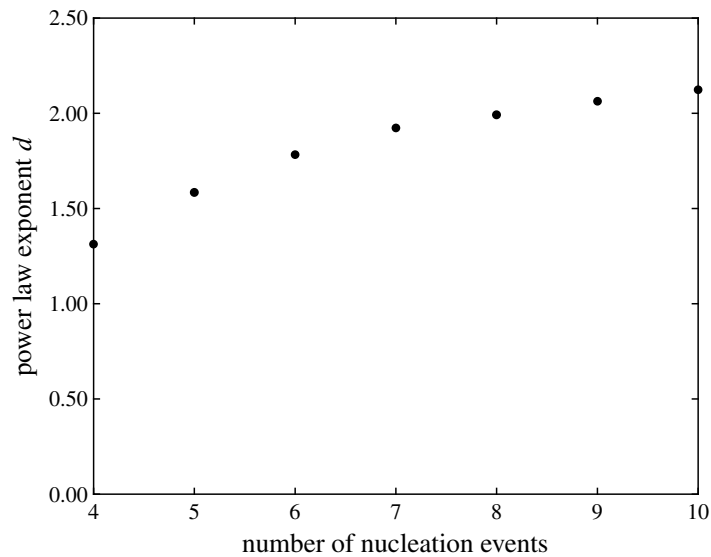
Figure 2.17: The evolution of the power law exponent d with successive nucleation events in a typical model run. After 4 nucleation events the BSD is intermediate between an exponential and power law form. For 5 events and greater the BSD is power law in form; the exponent increases with the number of nucleation events.

2.6.1 The effect of the bubble growth law

So far we have used a parabolic (diffusional) growth law for bubbles. This growth law has been shown (Proussevitch and Sahagian 1993a; Lyakhovsky et al. 1996; chapter 3, this thesis) to be an oversimplification, particularly for high-viscosity melts. Other growth laws may be used in the model, and the major results are unaffected. Figure 2.18 shows the results of a model run in which the bubbles grew according to a linear growth law, $r \propto t$. A single nucleation event gives a unimodal distribution as before. After 4 nucleation events the BSD is exponential in form. A power law distribution is generated after 7 events. Between these times the distribution is intermediate between an exponential and a power law form and the BSD may be equally well fit by either form. This insensitivity of the results to the bubble growth law is due to the fact that the BSD is constrained mainly by the *geometry* of the system; the details of the vesiculation process do not affect this fundamental property.
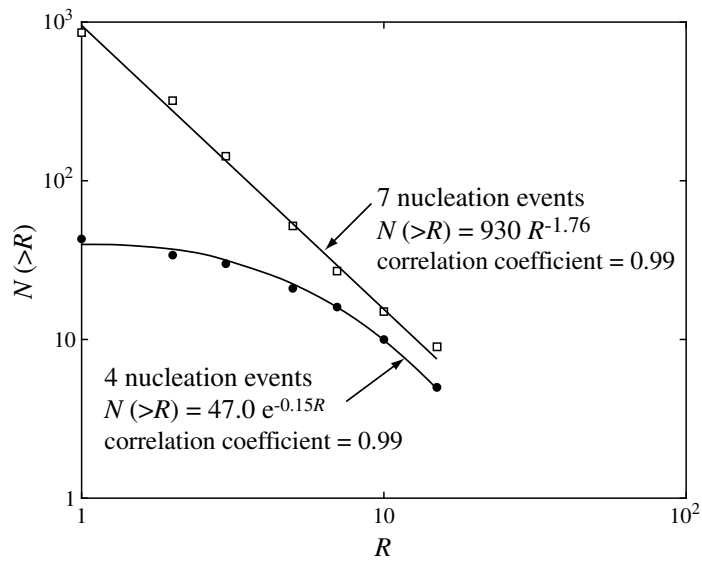
Figure 2.18: The results of a model run in which bubbles grew according to a linear growth law, $r \propto t$. An exponential BSD is produced after 4 nucleation events; a power law distribution is observed after 7 events. The initial unimodal distribution has been omitted from this diagram for clarity.

2.6.2 The effect of the nucleation rate

In the model described so far, each nucleation event populates all Voronoi vertices with new bubble nuclei. The 'nucleation rate' may be altered by only populating a certain fraction of the vertices in each event. Again this has very little effect on the main results of the study. Figure 2.19 shows the results of a model run in which only half of the Voronoi vertices were populated with new nuclei in each time step. A progression through an exponential BSD (4 nucleation events) to a power law BSD (7 events) is once more produced.
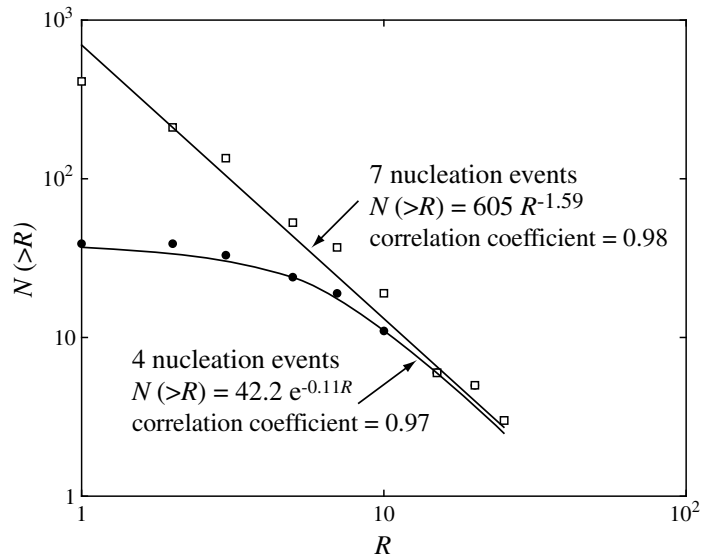
Figure 2.19: The results of a model run in which only half of the Voronoi vertices were populated with new nuclei in each time step, simulating a slower nucleation rate. Once more, an exponential BSD is produced after 4 nucleation events; a power law distribution is observed after 7 events.

2.7   Textural evidence for space-filling behaviour

The numerical model provides strong evidence that a mechanism of continuous nucleation in which the bubbles tend to pack efficiently and fill space can account for the presence of power law BSDs. If this is the case in nature we expect to see a characteristic pattern in textures of natural and experimentally-produced foams. Figure 2.20 shows six such images which illustrate this.

2.8   Interpretation and discussion

The simple numerical model has shown that it is possible to generate exponential and power law BSDs by the mechanism of continuous nucleation, in the absence of bubble coalescence. Analogue experiments (section 2.4) have also succeeded in generating power
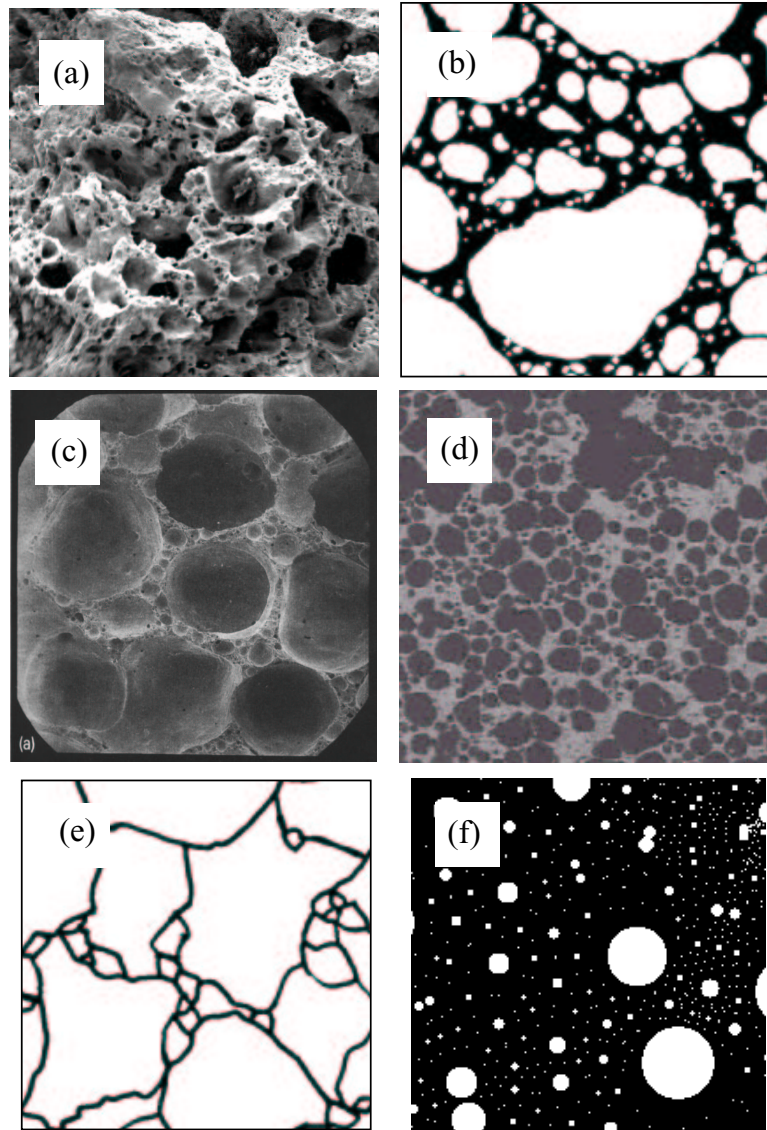
Figure 2.20: Illustration of space-filling behaviour in different systems. In each picture several bubble generations are visible with smaller bubbles filling the spaces between larger ones. (a) SEM image of a sample of scoria from the Kokkino cinder cone, Santorini. Image is 7 mm across. (b) Thin section of scoria from a basaltic sub-Plinian eruption of of Izu-Oshima, Japan (reproduced from Toramaru, 1990). Image is 6 mm across. (c) Sample of experimentally-produced andesitic foam from figure 8 of Proussevitch et al. (1993b). The similarity between this sample and the Apollonian packing (figure 2.14a) is striking. Image is 4 mm across. (d) Sample of experimentally-produced foam from figure 3 of Simakin et al. (1999). Image is 4 mm across. (e) Sample of gum rosin foam. The foam vesicularity is very high ($\sim 90\%$) and so the bubbles are in the form of polyhedral cells. Image is 1.2 mm across. (f) Image of a slice through the 'foam' produced in the numerical model described in the text.

law BSDs. One characteristic of the analogue experiments is that degassing is a highly non-equilibrium process. In the experiments the pressure drop is extremely rapid and the volatile (acetone) content of the solution is high; it is therefore impossible for all the acetone to be lost from the solution on the timescale of decompression. This is borne out by observation; the residual acetone content of the foam immediately after expansion ceases is significant (Mourtada-Bonnefoi and Mader 2001). The foam becomes sufficiently permeable to allow these residual volatiles to escape without any further expansion.

2.8.1   Non-equilibrium degassing and continuous nucleation

The combined results of the analogue experiments and numerical modelling suggest that the presence of a power law or exponential BSD is indicative of a degassing system that cannot maintain equilibrium with its environment. If the diffusive mass transfer of volatile molecules into the first bubble population nucleated is not rapid enough to allow the system to maintain a volatile concentration in the melt which is in equilibrium with the ambient pressure then further bubbles may nucleate in the volatile-rich melt pockets between bubbles (Lyakhovsky et al, 1996). Such nucleation behaviour has been reported in experiments simulating the degassing of silicate melts (Navon et al. 1998; Simakin et al. 1999). As a result of this non-equilibrium degassing continuous bubble nucleation occurs and a power law BSD is generated. Power law or exponential BSDs are to be expected whenever a system is forced far from equilibrium and physical parameters do not favour efficient degassing, i.e. for rapid depressurization, low initial nucleation density, and slow volatile diffusion. The exponent d is a measure of the number of nucleation events, or the length of the nucleation period relative to the timescale of growth.

2.8.2 Coalescence versus continuous nucleation

The mechanism of producing power law BSDs by means of continuous nucleation does not incorporate the effects of coalescence. In an effusive eruption involving low viscosity magma, we might expect that degassing will be close to equilibrium, and so the likelihood of the occurrence of several nucleation events is much reduced. The mechanism of cascading coalescence (Gaonac'h et al. 1996a) may therefore be dominant in generating power law BSDs in basaltic lavas (Gaonac'h et al. 1996b).

By contrast, in the case of explosive eruptions, especially involving acidic, highly viscous magma and rapid magma ascent rates, bubble growth models (Proussevitch and Sahagian 1996; chapter 3, this thesis) predict non-equilibrium degassing and so continuous nucleation may occur. Simakin et al. (1999) observed power law BSDs in samples produced during controlled experiments in which continuous nucleation occurred, but little or no coalescence took place. Toramaru's (1990) analysis led him to conclude that "bubble coalescence does not predominate in sub-Plinian to Plinian explosive eruptions". In our re-analysis of data from Toramaru (1990), we used his 'decoalesced' images (his figure 2) and discovered power law BSDs. We interpret these pre-coalescence power law BSDs to be the result of multiple nucleation events.

Gaonac'h et al. (1996a) predict that cascading coalescence will generate a BSD of the form $N(V) \propto V^{-2}$. In terms of a cumulative histogram, this gives $N(> V) \propto V^{-1}$. Since $V \propto R^3$, we have $N(> R) \propto R^{-3}$. In other words, we expect $d = 3$ for a process of cascading coalescence. The above analysis has shown that the mechanism of continuous nucleation gives exponents close to 2.5; the re-analysis of Toramaru's (1990) images gave $d = 2.5$ for his scoria samples; the Healy data give $d = 2.5$ for most of the bubble population, the three-dimensional Apollonian packing has $d \sim 2.45$ and the foam generated in the analogue experiments gave values of d between 2 and 2.5. Furthermore, Gaonac'h et al. (1996b) report that $B \approx 0.85$ for bubbles in the 'coalescence regime'. This translates to

$d = 2.55$ (since $d = 3B$), closer to the values obtained from continuous nucleation than to the predicted value of 3 for cascading coalescence. It appears that an exponent of around 2.5 is indicative of a mechanism of continuous nucleation. This must be treated with caution, however; the accurate measurement of d is notoriously difficult (section 2.4.3)

In the samples of pumice from Healy volcano (figure 2.3) two power laws were observed. I would suggest that the power law describing the smaller bubbles is due to the mechanism of continuous nucleation described above. The BSD of the larger bubbles may be a coalescence signature (cf. figure 2.1); coalescence increases the number of large bubbles in the population.

2.9 Conclusions

This analysis implies that, for conditions of non-equilibrium degassing, bubble nucleation may proceed in a continuous fashion, leading to the evolution of an exponential or power law BSD. A point which is yet to be resolved is the problem of why laboratory experiments concerning the degassing of silicate melts do not in general produce continuous nucleation (e.g. Lyakhovsky et al. 1996; Gardner et al. 1999). This is probably due to a difficulty in nucleation; most laboratory systems investigate crystal-free melt. However, Simakin et al. (1999) allowed crystallization to occur in their experiments and did indeed observe continuous nucleation. The presence of crystals appears to have facilitated bubble nucleation. The experiments of Proussevitch et al. (1993b) are particularly instructive. They investigated the degassing of andesitic and rhyolitic melt. The rhyolitic samples were crystal-free and did not produce a characteristic space-filling pattern of bubbles. However, the andesitic samples contained around 7% quartz particles; the texture of the foam produced (figure 2.20c) strongly implies that continuous nucleation occurred in this case.

The presence of power law BSDs in volcanic rocks has important implications for models

of lava rheology and magmatic degassing, most of which assume that the BSD is monodisperse.

2.9.1   Implications for modelling volcanic processes

These findings may resolve an apparent contradiction in current numerical models of explosive volcanic eruptions. Conduit flow models (Papale et al. 1998; Melnik and Sparks 1999) are usually based on the assumption that degassing is an equilibrium process. By contrast, bubble growth models (Proussevitch and Sahagian 1996) assume a single nucleation event and a monodisperse BSD and predict non-equilibrium degassing under the conditions of an explosive eruption, in agreement with our observations. However, highly non-equilibrium conditions would be expected to lead to continuous nucleation. This would tend to increase the efficiency of the degassing process and allow the system to remain close to equilibrium. The process of continuous nucleation can explain why the assumptions behind conduit flow models can also be consistent with non-equilibrium degassing.

Chapter 3

A numerical model of bubble growth in magma, incorporating volatile-dependent viscosity and diffusivity

3.1 Summary

A numerical model of bubble growth in rhyolitic melts is described and developed. The model incorporates the latest parameterizations of melt viscosity, water diffusivity, solubility and equation of state. The model is used to investigate the sensitivity of the dynamics of bubble growth to factors such as viscosity, diffusivity, temperature and pressure. We focus on the effect of allowing melt viscosity and water diffusivity to vary with water content, and find that this has a profound effect on the growth dynamics. The effects of viscosity and diffusivity are seen to be highly coupled. A high diffusivity causes the melt to dehydrate quickly. The melt viscosity therefore increases rapidly, counteracting the fast mass transfer of volatiles. This leads to the important result that, with concentration-dependent diffusivity, the bubble growth rate is significantly increased compared with constant diffusivities of similar magnitude. The dynamics of bubble growth are insensitive to the choice of the equation of state of water vapour. The choice of the solubility law

is important; slight changes in the water content at the bubble wall lead to significant changes in the effective viscosity of the melt. The viscous resistance to bubble growth is controlled by the bubble radius and the viscosity of the dehydrated melt near the bubble wall; the lower far-field viscosity has little influence. In general, many important features of the dynamics of bubble growth cannot be captured if either viscosity or diffusivity is assumed constant.

3.2 Introduction

The growth of bubbles is the primary driving force behind volcanic eruptions. When a batch of magma containing dissolved volatiles (e.g. H_2O) is decompressed to a pressure below the saturation pressure of the volatiles, bubbles may nucleate and grow. The expansion of these bubbles drives a rapidly-evolving, two-phase flow up the volcanic conduit.

In general, bubble growth is driven by two factors; the diffusion of volatile molecules into the bubble and reduction of the ambient pressure. Growth is resisted by the interfacial surface tension and by the viscous resistance and inertia of the melt. (viscous resistance is by far the most important factor in restricting bubble growth in volcanic eruptions; Sparks 1978) Two main equations, therefore, describe the dynamics of bubble growth. The hydrodynamic equation considers the balance of pressures around a bubble and accounts for the motion of the surrounding fluid (e.g. Proussevitch et al. 1993a):

$$p_g = p_a + \frac{2\sigma}{R} + \frac{4\eta}{R}\frac{\mathrm{d}R}{\mathrm{d}t} + \rho\left[R\frac{\mathrm{d}^2R}{\mathrm{d}t^2} + \left(\frac{\mathrm{d}R}{\mathrm{d}t}\right)^2\right] \tag{3.1}$$

This states that the pressure (p_g) inside a bubble of radius R is balanced by the sum of the ambient pressure (p_a), the surface tension pressure (σ is the surface tension), the viscous pressure (η is the Newtonian dynamic viscosity of the liquid) and the inertial pressure (ρ is the liquid density). The diffusion equation describes the mass transfer of volatiles

through the melt into the bubble:

$$\frac{\partial c}{\partial t} + \frac{\mathrm{d}R}{\mathrm{d}t}\frac{\partial c}{\partial R} = \frac{1}{R^2}\frac{\partial}{\partial R}\left(kR^2\frac{\partial c}{\partial R}\right) \qquad (3.2)$$

The second term on the left hand side accounts for the advective flux of volatiles toward the bubble wall as the bubble grows. All existing theoretical models of bubble growth are based, to some extent, around equations 3.1 and 3.2. The two major assumptions behind these two equations are that the system is spherically symmetric and that the melt viscosity is constant. In this chapter a model is developed which allows viscosity to vary with volatile concentration; in this case the viscosity coefficient η in equation 3.1 is replaced with an *effective* viscosity. No model has yet been developed to describe the growth of bubbles if the system is not spherically symmetric.

The results of studies of bubble growth have fundamental implications for several aspects of volcanology. The growth rate of a population of bubbles can be used to calculate the rate of expansion of a batch of magma. Magma may fragment if the overpressure inside the bubbles ($= p_g - p_a$, equation 3.1) exceeds the tensile stress of the melt (McBirney and Murase 1970; Alidibirov 1994; Melnik 2000). An overpressure in the bubbles in a lava dome may lead to spontaneous disruption of the dome and the formation of pyroclastic flows (Navon et al. 1998). The distribution of dissolved water in the melt (equation 3.2) controls the melt viscosity, which in turn controls how rapidly the magma flows through the volcanic plumbing system. If the rate of magma ascent is high, or diffusivity is low, then the degassing of volatiles may not be sufficiently rapid to keep pace with the falling pressure. This non-equilibrium degassing leads to the build-up of a supersaturation in the magma which can lead to violent explosive activity near the surface (Mangan and Sisson 2000).

The dynamics of bubble growth are therefore highly coupled to the dynamics of large-scale volcanic conduit flow. So far no study has investigated the two processes together; models

of conduit flow typically assume equilibrium degassing (Papale et al. 1998; Melnik and Sparks 1999) whereas models of bubble growth either assume instantaneous depressurization or some highly simplified rate of decompression (e.g. Proussevitch and Sahagian 1996). The two types of model are, theoretically, easily linked— the value of the ambient pressure in equation 3.1 could be taken from a conduit flow model. In turn, the resulting growth rate of the bubble could be used by the conduit flow model to calculate the expansion rate of magma. Such a study will surely be performed in the near future and will represent a significant advance in the field of the modelling of volcanic processes.

The growth of bubbles during an eruption cannot be directly observed. The process has, however, been the subject of both experimental and theoretical investigation. I shall now summarize the principal findings of these studies.

3.2.1 Theoretical studies

The problem of bubble growth is not only of interest to volcanologists. Scriven (1959) investigated the dynamics of phase growth in many different situations, with particular application to nucleate boiling and heat transfer. He considered the growth of a bubble in an infinite liquid, neglecting the effects of surface tension, viscosity and inertia. A parabolic growth law was derived: $R = 2\beta\sqrt{kt}$, where k is the diffusivity (of heat or mass) and β is a growth constant which depends on the superheat (the difference between the ambient pressure and the vapour pressure of the liquid) and the physical properties of the liquid and gas phases. In magmas, however, bubbles do not grow in an infinite liquid; moreover viscous resistance plays a significant role in controlling the growth dynamics. The parabolic growth law is, however, a good approximation for diffusion-driven growth in low-viscosity magmas.

The first model to consider in detail the dynamics of bubble growth in volcanic eruptions was that of Sparks (1978). He considered the dynamics of bubble growth by both diffusion

and decompression. The parabolic growth law of Scriven (1959) was used to model the diffusional component of growth; Sparks selected values of β appropriate to the conditions of a volcanic eruption. The major results of the study are as follows: In basaltic magmas, bubble growth is initially controlled by diffusion, giving decelerating growth. Near the surface, however, decompression begins to dominate, giving accelerating growth. The faster the ascent rate, the smaller the final bubble radius due to the reduced time available for mass transfer. The final radius is very insensitive to the depth of nucleation (i.e. the supersaturation at nucleation); late-nucleating bubbles have fast initial growth rates and nearly catch up with bubbles which nucleated early. For the case of rhyolitic magmas, Sparks discovered the important result that the final size of bubbles is expected to be smaller than for basaltic magmas, a prediction which is confirmed by observations of pyroclasts. This is due to the lower diffusivity of water in rhyolitic melts and the faster ascent rates, not the higher viscous resistance. The overpressure in bubbles is predicted to be significant only for magmas with viscosities greater than $\sim 10^7$ Pa s. The major limitations of Sparks' model are: (i) the bubble is assumed to grow in an infinite liquid; (ii) the diffusion equation is not solved fully but approximated by Scriven's law; (iii) the *advective* flux of volatiles towards the bubble wall as the bubble grows is neglected; (iv) both volatile diffusivity and viscosity are assumed to be independent of water content.

For many years Sparks' model represented the state of the art in terms of the understanding of the dynamics of bubble growth. The complexity of the governing equations of bubble growth and their analytical intractability meant that little progress was made in the subject until Proussevitch et al. published the first version of their model in 1993. This model described the isothermal growth of bubbles in magmas by diffusion only. The diffusion equation (equation 3.2) was solved fully (including the advective flux of volatile molecules) and the bubble was conceived to grow in a *finite* melt shell (figure 3.1), simulating the presence of other bubbles in the system. The hydrodynamic equation for the flow of melt around a bubble (equation 3.1) was also solved, although the inertial term
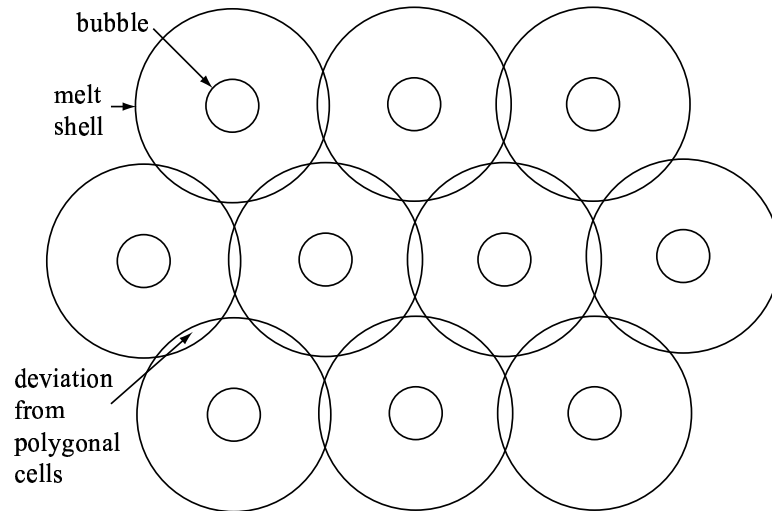
Figure 3.1: In the model of Proussevitch et al. (1993a) bubbles are envisaged to grow in a finite, concentric shell of melt. This gives a reasonable approximation to a multi-bubble system in which the bubbles are close-packed. The deviation between the spheres and close-packed polyhedra is less than 5%.

was neglected (inertia is only likely to be important for very large bubbles in low-viscosity magma, Sparks 1978). The formulation of Proussevitch et al. (1993a) has been used as the basis for many subsequent bubble growth models, discussed below.

The full system of equations solved by Proussevitch et al. (1993a) include equations 3.1 and 3.2, plus the boundary conditions of gas saturation (Henry's law) at the bubble/melt interface and zero volatile flux through the outer boundary of the shell. The system simulates the growth of a bubble in a melt which has become supersaturated due to instantaneous decompression. Their results indicate that the strongest control on bubble growth is the ambient pressure and the resulting volatile supersaturation. A high initial volatile content actually *reduces* the time required for complete bubble growth due to steep concentration gradients at the bubble wall; the steep gradients give fast initial growth and hence a rapid advective flux of volatiles towards the bubble wall. Diffusivity is also important, particularly for basaltic melts. Viscosity limits bubble growth above $\sim 10^4$ Pa s, i.e. for most cases of eruptions of acidic magma. Both diffusivity and viscosity are assumed

constant.

One of the most interesting features of the model is the discovery of an initial period of slow growth in high viscosity melts. This transient effect has been referred to as a "time-lag" or "period of accelerating growth" and was attributed to surface tension effects by Proussevitch et al. (1993a). In a comment to this paper, Sparks (1994) showed that this explanation was unlikely and proposed that the time-lag was due to viscous resistance of a small bubble, coupled with a reduction in diffusive mass transfer due to the small surface area of the bubble. In their reply, Sahagian et al. (1994) conceded that surface tension was not important in creating this time-lag, but also showed that the surface area effect was not a factor. The time-lag was observed in the experiments of Bagdassarov et al. (1996) and so cannot be a numerical artefact. A persuasive explanation of the time-lag was provided by Navon et al. (1998), in which it was shown that the time-lag is indeed a viscous effect. This will be discussed later in this section.

In Proussevitch and Sahagian (1996) the model of Proussevitch et al. (1993a) was extended to deal with coupled diffusive and decompressive growth. They specified fixed ascent rates in order to obtain a constant decompression rate; in volcanic systems the rate of magma ascent is coupled to the growth of bubbles and the expansion of the magma, and so the decompression rate is unlikely to be constant. This study revealed several important results about the processes of equilibrium and non-equilibrium degassing. Basaltic melts are expected to degas in equilibrium for all reasonable magma ascent rates. Rhyolitic melts can degas in equilibrium for ascent rates less than $1 \mathrm{~m\,s}^{-1}$. For velocities greater than this, high supersaturations are expected near the surface, which may lead to explosive activity. Typical ascent velocities for magma in explosive eruptions have been estimated from field measurements at a few metres per second (see examples in Proussevitch and Sahagian 1996). For slow ascent rates, bubble growth is limited by decompression; faster ascent rates lead to diffusion-limited (non-equilibrium) degassing. Magma viscosity and volatile diffusivity are still assumed constant in this study.

The same formulation was further extended in Proussevitch and Sahagian (1998), in which the effects of volatile-dependent viscosity and diffusivity, as well as the energetics of volatile degassing, are incorporated. It was calculated that the parabolic growth law $R \sim \sqrt{t}$ is not appropriate for high supersaturations or low pressures and they proposed a logarithmic law $R \sim \log t$ to describe growth under these conditions. It was also calculated that non-equilibrium degassing is expected for ascent rates greater than $1 - 5 \text{ m s}^{-1}$. Their model is extremely complex and the effects of many parameters are examined. One important factor which was not discussed is the effect on the growth dynamics of incorporating concentration-dependent viscosity and volatile diffusivity. This will form the major part of the discussion in this chapter, in which it shall be shown that the concentration-dependent nature of viscosity and diffusivity is a very important factor in controlling the dynamics of bubble growth.

The model of Toramaru (1995) is one of the only studies to consider a *population* of bubbles (see chapter 2 for discussion of his predictions concerning the size distribution of bubbles). Compared with the analyses of Proussevitch and co-workers, Toramaru's consideration of the dynamics of bubble growth is rather simplified and will not be discussed here in detail (for example, he does not solve fully the diffusion equation). However, in common with the studies discussed so far, Toramaru's analysis reveals that bubble growth may be controlled by viscosity or diffusivity, depending on the decompression rate, the initial saturation pressure and the melt viscosity.

In general, the results of complicated numerical models such as those described above can be hard to interpret due to the large number of parameters involved and the coupling between them. Many workers feel that a greater understanding and intuition can be gained by deriving simplified *analytical* descriptions of bubble growth dynamics. Barclay et al. (1995) derived analytical solutions for bubble growth due to instantaneous decompression in the absence of diffusion. Two cases were examined: bubble growth in an infinite melt and growth in a thin shell of melt. It was calculated that viscosities greater than 10^9 Pa s

(cf. 10^7 Pa s in Sparks 1978) are required to preserve a significant overpressure in the bubble, a result also derived by Thomas et al. (1994). This was used as the basis of a proposal that the typical observed vesicularities of pumice (70%–80%) are the result of the degassing magma reaching a viscosity of 10^9 Pa s. The model developed in this chapter, however, reveals that the effective viscosity of magma at these vesicularities is likely to be much lower than 10^9 Pa s.

3.2.2 Experimental studies

It is clear that the dynamics of bubble growth are extremely complex; the models described above are potentially powerful, but their validity must be tested by comparing their predictions with the results of experimental studies. Although laboratory investigations into the degassing of silicate melts have their restrictions, the data they generate are the result of real physical processes, and are subject to fewer simplifying assumptions than most numerical models.

One of the first studies of bubble growth was that of Murase and McBirney (1973). They investigated the nucleation and growth of bubbles in samples of obsidian initially containing 0.2 wt.% water. The obsidian was heated to 1050°C and the growth rates of bubbles were measured. Average growth rates covered a range from zero to 7×10^{-5} mm s^{-1}. The authors did not propose a reason for observing such a range of growth rates, but it was probably due to an inhomogeneous distribution of water content (Liu and Zhang 2000). In any case, the data illustrate that the bubbles in a population do not grow under identical conditions.

Bagdassarov et al. (1996) performed a more systematic study of bubble growth in rhyolitic melt with an initial water content of 0.14 wt.%. They found that in the temperature range 650–790°C the growth dynamics were controlled by viscosity and for higher temperatures (790–925°C) diffusion becomes the limiting factor, due to the reduction in viscosity at

this increased temperature. The study also suggested that the dynamics of nucleation may also be controlled by melt viscosity, a finding which cannot be addressed by classical nucleation theory.

Lyakhovsky et al. (1996) investigated the dynamics of bubble growth through experimental, numerical and analytical studies. They observed the growth of bubbles in rhyolites with high initial water content (5.3–5.5 wt.%) and fitted the data using existing models of bubble growth. The simple model of Scriven (1959) was only found to be valid for isolated bubbles in the early stages of growth; in most cases the more sophisticated analysis of Proussevitch et al. (1993a) was required to explain their data. Under the conditions of their experiments they found that bubble growth was controlled by diffusion with viscous effects only being important in the very initial stages ($t < 1$ s) of growth. One of the major strengths of the study was that the authors developed *analytical* solutions for bubble growth at small Peclet numbers (Pe $= \Delta P\, R^2/\eta k$ where ΔP is the supersaturation pressure, R is the bubble radius, η is the melt viscosity and k is the volatile diffusivity).

This multi-faceted approach was continued by Navon et al. (1998). They examined the early stages of bubble growth in highly viscous melts, a regime which they showed to be controlled by the melt viscosity. In these early stages of growth in the case of Pe < 1, diffusion is rapid and a steady-state concentration profile can be maintained. This allows an analytical approximation for bubble growth in this regime to be derived. This was shown to be an exponential solution with a characteristic timescale of $4\eta/\Delta P$ and was verified experimentally. This is the "period of accelerating growth" or "time-lag" recorded by Proussevitch et al. (1993a) and later debated by Sparks (1994) and Sahagian et al. (1994), as discussed above. In the same study, the authors modified the model of Lyakhovsky et al. (1996) to incorporate the effects of concentration-dependent viscosity and diffusivity, but did not discuss this in detail.

Gardner et al. (1999) investigated bubble growth in rhyolitic melts under conditions of a

continuous pressure drop. Their melts were saturated in water at 200 MPa and 850°C, giving a much higher initial water content (~ 5.5 wt.%) than in the experiments of Murase and McBirney (1973) or Bagdassarov et al. (1996). Their main finding was that at decompression rates of 0.025 MPa s^{-1}, degassing proceeded in equilibrium with the pressure drop. For decompression rates of 0.25, 0.5 and 1.0 MPa s^{-1} (roughly speaking, magma ascent rates of 10, 20 and 40 m s^{-1}) non-equilibrium degassing was observed, largely in agreement with the predictions of Proussevitch and Sahagian (1996). Furthermore, bubbles which nucleated at high supersaturations were observed to grow more rapidly than those which formed at low supersaturations, in agreement with the models of Sparks (1978) and Proussevitch et al. (1993a).

The effect of high melt viscosities on bubble growth under continuous pressure drop was investigated by Gardner et al. (2000). They used lower temperatures and water contents than did Gardner et al. (1999) in order to raise the viscosity of the liquid. They found that melts ceased to degas efficiently for melt viscosities greater than 10^{7-8} Pa s, but interpreted this to be a result of a lower volatile diffusivity at the low temperatures they used to create melts of this viscosity. For decompression rates of 0.125 and 0.25 MPa s^{-1} (roughly, ascent rates of 5 and 10 m s^{-1}), they find that a viscosity of $\sim 10^{9}$ Pa s is required to arrest bubble expansion, in agreement with the predictions of Thomas et al. (1994) and Barclay et al. (1995).

Liu and Zhang (2000) observed the growth of bubbles in a natural rhyolitic melt at atmospheric pressure and 500–600°C, from initial water contents of 1.4–2.0 wt.%. They compared their results with the predictions of the numerical model of Proussevitch et al. (1998) and claimed that theirs was "the first experimental verification of a bubble growth model in a silicate melt" (the study of Navon et al. 1998 involved fitting parameters for viscosity and diffusivity). As in the study of Murase and McBirney (1973) it was found that bubbles in the same experimental sample grew at different rates. Liu and Zhang attributed this to an initial inhomogeneous distribution of volatiles. Proussevitch and

Sahagian's (1998) model gives an excellent fit to Liu and Zhang's data. To produce these good fits, however, the authors were forced to allow viscosity to vary within a factor of 5 of the predicted value from the study of Hess and Dingwell (1996). This factor is within the error of the Hess and Dingwell's parameterization (equation 3.17), but serves to highlight the fact that the dynamics of bubble growth can be very sensitive to viscosity, even within the bounds of error of the most sophisticated current models. This represents a major limitation in our ability to predict accurately bubble growth rates in eruptions of rhyolitic magma.

3.2.3   Motivation behind this study

Although numerical models of bubble growth now incorporate the dependence of melt viscosity on its volatile content (e.g. Proussevitch and Sahagian 1998, Navon et al. 1998), the details of this effect have not been discussed. During bubble growth, the viscosity of the melt will vary both temporally and spatially due to the diffusion of volatile molecules down concentration gradients. The model developed in this chapter will investigate the phenomena of concentration-dependent viscosity and diffusivity and their effects on the dynamics of bubble growth.

A second reason for performing this study was to investigate the sensitivity of the bubble growth dynamics to the parameters of the model (e.g. water solubility, equation of state of water vapour). Knowledge of this sensitivity is important when applying the results of bubble growth models to practical situations. Liu and Zhang (2000) have already demonstrated that the dynamics of bubble growth are very sensitive to viscosity, even when viscosity is varied within the range of error of the most sophisticated parameterizations.

The bulk of the material in this chapter has been submitted for publication in Earth and Planetary Science Letters (J.D. Blower, H.M. Mader and S.D.R. Wilson, *Coupling of viscous and diffusive controls on bubble growth during explosive volcanic eruptions*).

3.2.4 Limitations of bubble growth models

Despite the complexity and sophistication of current models of bubble growth in magmas, they are still limited by several major assumptions; (i) spherical symmetry of the system; (ii) no gas is lost from the system; (iii) the rate of decompression is either instantaneous or highly simplified; and (iv) the initial volatile concentration in the melt is uniform. These limitations also apply to the model developed in this chapter.

3.3 Model formulation

Following the treatment of Proussevitch et al. (1993a), we envisage the bubble to grow in a concentric shell of melt (figure 3.1); this simulates the influence of other bubbles in the system. The initial radius of the shell is S_0, and is related to the nucleation density n by the following expression:

$$S_0 = \left(\frac{3}{4\pi n} \right)^{1/3} \tag{3.3}$$

The model contains equations which describe the diffusion of water into the growing bubble, the hydrodynamics of the motion of fluid around the bubble, mass balance of volatile (water) molecules, the internal bubble pressure, the solubility of water and the variation of viscosity and diffusivity with water content. The solution is cast in Lagrangian coordinates. All equations are ultimately cast in the form of time derivatives, and these are integrated simultaneously using well-established, professional library routines. Table 3.1 summarizes the symbols used in the following derivations. Bubble growth is assumed to be isothermal; the validity of this assumption is discussed in Proussevitch and Sahagian (1998), in which the energetics of bubble growth are investigated.
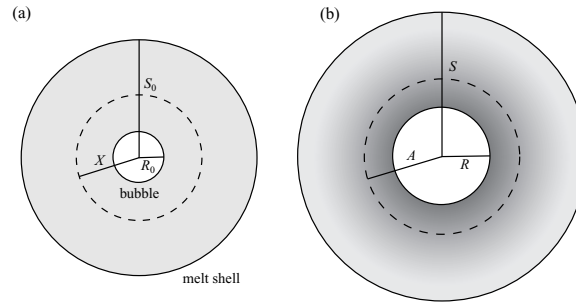
Figure 3.2: The coordinate system used in the model. (a) Initial conditions. The water concentration is uniform throughout the melt shell. (b) Conditions after time t. The shading schematically illustrates the increase in viscosity near the bubble wall due to volatile depletion. The bubble has grown from an initial radius R_0 to a radius R. The melt shell initially between R_0 and X is now contained in the region from R to A. Not to scale.

3.3.1 The coordinate system

The system is radially symmetrical and the Lagrangian coordinate X is employed as the radial coordinate. X is a label for a given shell of fluid; its value is the radius of the shell at $t = 0$. If at time t the radius of that shell is A, and the initial and final bubble radii are R_0 and R respectively then we have, by conservation of volume (figure 3.2):

$$A^3 - R^3 = X^3 - R_0^3 \tag{3.4}$$

3.3.2 The system of equations

The diffusion equation

In this coordinate system, the radial diffusion equation is (Braithwaite et al. 1999):

$$\frac{\partial c}{\partial t} = \frac{1}{X^2} \frac{\partial}{\partial X} \left(k(c) \frac{A^4}{X^2} \frac{\partial c}{\partial X} \right) \tag{3.5}$$

X	radial Lagrangian coordinate (m)
A	radial Eulerian coordinate (m)
R	bubble radius (m)
S	shell radius (m)
n	nucleation density (m^{-3})
c	volatile (water) concentration (mass fraction)
F	volatile (water) concentration (mole fraction)
t	time (s)
k	diffusion coefficient (m^2 s^{-1})
p	pressure (Pa)
m	mass of vapour in bubble (kg)
$\bar{V}$	molar volume of vapour in bubble (m^3 mol^{-1})
f	water fugacity (Pa)
η	dynamic viscosity (Pa s)
η_{eff}	effective dynamic viscosity (Pa s)
ρ	density (kg m^{-3})
β	rate of pressure drop (Pa s^{-1})
T	temperature (K)
α	Henry constant (Pa$^{-1/2}$)
G	molar gas constant (J K^{-1} mol^{-1})
M	molar mass (kg mol^{-1})
N	number of grid points
Subscripts	
g	gas / vapour
m	melt
i	condition at grid point i
0	condition at $t = 0$ or $i = 0$
∞	condition in far-field (at shell wall)

Table 3.1: Explanation of symbols used in the text

where $c = c(X, t)$ is the volatile concentration (mass fraction) at time t and k is the concentration-dependent diffusion coefficient. Due to the Lagrangian reference frame this automatically incorporates the advective flux of water molecules toward the bubble wall as the bubble grows. The boundary condition at the bubble-melt interface is a solubility condition:

$$c_{X=R_0} = f(p_g, T) \tag{3.6}$$

i.e. the concentration of water at the bubble wall is saturated at temperature T and pressure p_g. At the shell wall:

$$\left.\frac{\partial c}{\partial X}\right|_{X=S_0} = 0 \tag{3.7}$$

which is to say that there is no diffusive mass flux of volatiles through the outer boundary of the shell.

The hydrodynamics of the melt

The equation describing the motion of the fluid around the growing bubble is (see appendix C):

$$p_g = p_\infty + 12R^2 \frac{\mathrm{d}R}{\mathrm{d}t} \int_{R_0}^{S_0} \frac{\eta(X)X^2}{(R^3 - R_0^3 + X^3)^2} \, \mathrm{d}X \tag{3.8}$$

where p_∞ is the ambient pressure and $\eta(X)$ is the spatially-dependent melt viscosity ($\eta = \eta(c)$ and $c = c(X)$, equation 3.17). The effects of surface tension and inertia are neglected.

Mass balance

The mass m of water vapour in the bubble is given by:

$$m = m_0 + 4\pi\rho_m \left(\int_{R_0}^{S_0} c(X, 0)X^2 \, \mathrm{d}X - \int_{R_0}^{S_0} c(X, t)X^2 \, \mathrm{d}X \right) \tag{3.9}$$

Since the initial water concentration c_0 in the melt is assumed to be uniform, the first term in the brackets may be simplified to $\pi c_0 (S_0^3 - R_0^3)/3$.

Bubble pressure

In this model, the equation of state for water of Pitzer and Sterner (1994) is used:

$$\frac{p_g}{10^6 GT} = \rho + a_1 \rho^2 - \rho^2 - \frac{a_3 + 2a_4 \rho + 3a_5 \rho^2 + 4a_6 \rho^3}{(a_2 + a3\rho + a_4 \rho^2 + a_5 \rho^3 + a_6 \rho^4)^2}$$
$$+ a_7 \rho^2 \exp(-a_8 \rho) + a_9 \rho^2 \exp(-a_{10}\rho) \quad (3.10)$$

where ρ is the gas density in $mol\,cm^{-3}$ and a_1 to a_{10} are temperature-dependent parameters, given in Pitzer and Sterner (1994). This equation is valid from zero pressure to 10 GPa and from the critical temperature of water (647 K) to 2000 K.

We compare the results using equation 3.10 with results from model runs in which we make the assumption that the water vapour in the bubble behaves as an ideal gas:

$$\frac{p_g R^3}{m} = \frac{p_0 R_0^3}{m_0} \quad (3.11)$$

where p_0 is the initial pressure inside the bubble.

Ambient pressure

In most model runs we assume that the confining pressure outside the melt shell is instantaneously reduced to atmospheric pressure. This is unlikely to happen in a natural system. As magma rises through the conduit the pressure will fall due to the progressive removal of overlying magma. The rate of depressurization is often taken to be a proxy for the ascent rate of magma (Proussevitch and Sahagian 1996). Furthermore, even if a batch of magma containing a large number of bubbles is instantaneously decompressed

(due to the sudden failure of the volcanic edifice, for example), the internal liquid pressure within this magma batch will not fall instantaneously to the ambient pressure because of the internal viscous stresses created by the overall expansion.

We can specify arbitrary rates of change of ambient pressure. For simplicity we choose a linear pressure drop:

$$p_\infty = p_0 - \beta t \tag{3.12}$$

where β is the rate of pressure drop. The ambient pressure ceases to fall once the final pressure (usually atmospheric) pressure is reached.

The solubility of water in rhyolitic melt

We use the solubility law of Zhang (1999b) as this is valid over a very wide pressure and temperature range: it is calibrated from $500 - 1350°\mathrm{C}$ up to 800 MPa and verified by preliminary experimental data (Liu and Zhang 2000) at 0.1 MPa. The mole fraction F of water soluble in rhyolite at a pressure of P bars at T K, with a water fugacity f is:

$$
\begin{aligned}
F &= K_1 f + \frac{K_1 K_2 f (1 - K_1 f)}{K_1 K_2 f + \sqrt{(K_1 K_2 f)^2 + 4 K_1 K_2 f (1 - K_1 f)}} \\
\text{with} \quad \ln K_1 &= -13.869 + 0.0002474 P + \frac{3890.3 - 0.3948 P}{T} \\
K_2 &= 6.53 \exp \frac{-3100}{T}
\end{aligned}
\tag{3.13}
$$

f is calculated using the equation of state of Pitzer and Sterner (1994) (equation 3.10) and the relationship (Sterner and Pitzer 1994):

$$\ln f = \ln \rho + \frac{A^{\mathrm{res}}}{GT} + \frac{P}{\rho GT} + \ln(GT) - 1 \tag{3.14}$$

ρ is the gas density (in $\mathrm{mol\,cm}^{-3}$) at pressure P. Expressions for A^{res}/GT and $P/\rho GT$ are given in Pitzer and Sterner (1994) and in this case, $G = 8314510 \,\mathrm{Pa\,cm}^3\,\mathrm{K}^{-1}\,\mathrm{mol}$.

The mass fraction of soluble water c_{eq} is calculated from the mole fraction F:

$$c_{\mathrm{eq}} = \frac{MF}{W(1-F) + MF} \tag{3.15}$$

W is the mass of dry rhyolite per mole of oxygen and is taken to be $32.6 \, \mathrm{g \, mol^{-1}}$ (Zhang 1999b). $M = 18.015$ and is the molar mass of water in $\mathrm{g \, mol^{-1}}$.

For comparison (section 3.4.2) we also employ the more widely-used and less complex Henry law of solubility:

$$c_{\mathrm{eq}} = \alpha \sqrt{p_g} \tag{3.16}$$

where p_g is the internal bubble pressure and α is the temperature-dependent Henry constant. A comparison between Henry's law and Zhang's (1999b) model of solubility is shown in figure 3.4a.

Variation of viscosity with water content

We use Hess and Dingwell's (1996) model for the variation of viscosity with temperature and water content in hydrous leucogranitic melts. They proposed the following parameterization:

$$\log_{10} \eta = -3.545 + 0.833 \ln(w) + \frac{[9601 - 2368 \ln(w)]}{T - [195.7 + 32.25 \ln(w)]} \tag{3.17}$$

where η is in $\mathrm{Pa \, s}$, w is the water concentration in weight percent ($= 100c$) and T is in K.

Variation of diffusivity with water content

There are now several expressions for water diffusivity in the literature (e.g. Zhang et al. 1991; Nowak and Behrens 1997; Zhang and Behrens 2000). We prefer the model of Zhang and Behrens (2000) as it is calibrated against a wide range of experimental data

for rhyolitic compositions (0.1–7.7 wt.% H_2O, 400–1200°C, 0.1–810 MPa):

$$k = 10^{-12} F \exp(m) \left\{ 1 + \exp \left[56 + m + F \left(-34.1 + \frac{44620}{T} + \frac{57.3P}{T} \right) \right. \right.$$
$$\left. \left. - \sqrt{F} \left(0.091 + \frac{4.77 \times 10^6}{T^2} \right) \right] \right\} \quad (3.18)$$

where $m = -20.79 - 5030/T - 1.4P/T$, k is in $m^2 s^{-1}$, P is in MPa and T is in K. F is the mole fraction of total water (H_2O_t) on a single oxygen basis (equation 3.15).

Initial conditions

The initial volatile concentration c_0 is assumed to be uniform throughout the melt shell. We assume that the initial pressure in the bubble is the saturation pressure. The initial mass of water vapour in the bubble is then given by:

$$m_0 = \frac{4}{3} \pi R_0^3 \frac{M_g}{\bar{V}} \quad (3.19)$$

where $\bar{V}$ is the molar volume in $m^3\,mol^{-1}$ which is calculated using the equation of state of water vapour (equation 3.10).

3.3.3 Numerical Formulation

The grid

In order to ensure an accurate representation of the concentration profile throughout the melt shell, we construct the formulation so that grid points are closely spaced near the bubble wall, which is where the properties of the system change most rapidly. We achieve

this by performing a transformation on the Lagrangian coordinate X:

$$Y = \ln X \quad \Rightarrow \quad \frac{\partial c}{\partial X} = e^{-Y} \frac{\partial \tilde{c}}{\partial Y} \tag{3.20}$$

where $\tilde{c}(Y) = c(X(Y)) = c(e^Y)$. The melt region is divided into N shells of thickness δY:

$$\delta Y = \frac{\ln S_0 - \ln R_0}{N} \tag{3.21}$$

The melt region therefore contains $N + 1$ nodes. The value of Y at the ith node is given by:

$$Y_i = \ln R_0 + i\,\delta Y \tag{3.22}$$

and, from 3.4:

$$A_i = (e^{3Y_i} - R_0^3 + R^3)^{1/3} \tag{3.23}$$

Numerical solution of the diffusion equation

In the transformed coordinate system (section 3.3.3) the diffusion equation (3.5) becomes:

$$\frac{\partial \tilde{c}}{\partial t} = \frac{1}{e^{3Y}} \frac{\partial}{\partial Y} \left(k(\tilde{c}) \frac{A^4}{e^{3Y}} \frac{\partial \tilde{c}}{\partial Y} \right) \tag{3.24}$$

The diffusion equation is solved by the method of lines. In this method, the transformed space variable Y is discretized but the time t is not. This transforms the partial differential equation (equation 3.24) into a set of coupled ordinary differential equations.

At a general node i, an appropriate finite-difference approximation of equation 3.24 is

(appendix D):

$$
\frac{\mathrm{d}\tilde{c}_i}{\mathrm{d}t} = \frac{1}{2\,e^{3Y}\,\delta Y^2} \left\{ (k_{i+1} + k_i)(\tilde{c}_{i+1} - \tilde{c}_i)\frac{A^4_{i+1/2}}{e^{3Y_{i+1/2}}} \right.
$$
$$
\left. - (k_i + k_{i-1})(\tilde{c}_i - \tilde{c}_{i-1})\frac{A^4_{i-1/2}}{e^{3Y_{i-1/2}}} \right\} \quad (2 \le i \le N-1) \quad (3.25)
$$

Note that the right hand side is simply a number giving the rate of change of concentration at each grid point.

At the edge of the outer shell $(X = S_0)$, $i = N$ and the concentration $\tilde{c}_{i+1}$ is not defined. We may obtain this from the boundary condition in equation 3.7; the concentration gradient at this point is zero and so, by symmetry, $\tilde{c}_{N+1} = \tilde{c}_{N-1}$:

$$
\frac{\mathrm{d}\tilde{c}_N}{\mathrm{d}t} = \frac{(k_{N-1} + k_N)(\tilde{c}_{N-1} - \tilde{c}_N)}{2\,e^{3Y_N}\,\delta Y^2} \left\{ \frac{A^4_{N+1/2}}{e^{3Y_{N+1/2}}} + \frac{A^4_{N-1/2}}{e^{3Y_{N-1/2}}} \right\} \quad (3.26)
$$

Numerical solution of the hydrodynamic equation

Equation 3.8 may be rearranged to give the rate of bubble growth:

$$
\frac{\mathrm{d}R}{\mathrm{d}t} = \frac{p_g - p_\infty}{12R^2} \left(\int_{R_0}^{S_0} \frac{\eta(X)X^2}{(R^3 - R_0^3 + X^3)^2} \, \mathrm{d}X \right)^{-1} \quad (3.27)
$$

The integral factor is evaluated numerically (after transforming the grid back in terms of X; $X_i = e^{Y_i}$) using the NAG (Numerical Algorithms Group) library routine D01GAF which employs the Gill–Miller method of integration.

Numerical evaluation of the mass flux into the bubble

Differentiating equation 3.9 with respect to time gives:

$$\frac{\mathrm{d}m}{\mathrm{d}t} = -4\pi\rho_m \int_{R_0}^{S_0} \frac{\partial c}{\partial t} X^2 \, \mathrm{d}X \tag{3.28}$$

The value of $\partial c/\partial t$ at each grid point is given by equations 3.25 and 3.26. (Note that $\partial c/\partial t$ will be everywhere negative and so the mass flux will be positive.) The integral is evaluated numerically in X-space using the NAG routine D01GAF. This approach has the advantage that it does not require evaluation of the concentration gradient at the bubble wall (cf. Proussevitch and Sahagian 1998), which we discovered to be prone to numerical error.

Numerical evaluation of the ambient pressure drop

If we choose a non-instantaneous decompression, equation 3.12 gives:

$$\frac{\mathrm{d}p_\infty}{\mathrm{d}t} = \begin{cases} -\beta & (p_\infty > p_{\mathrm{final}}), \\ 0 & (p_\infty = p_{\mathrm{final}}). \end{cases} \tag{3.29}$$

where p_{final} is usually taken to be atmospheric pressure.

3.3.4 The solution algorithm

Equations 3.25 to 3.29 are a set of $N + 3$ coupled first-order ordinary differential equations (ODEs). Since this is a so-called stiff system (Press et al. 1992), ODE integration routines such as predictor–corrector algorithms (as used by Lyakhovsky et al. 1996) are inefficient. We integrate all $N + 3$ equations simultaneously using the NAG stiff ODE solver routine D02EJF which uses a variable-order, variable-step method implementing

backward differentiation.

Convergence and stability

Since the NAG ODE integration routine ensures that the time-step in the solution is always sufficiently small to ensure convergence, the user needs only to adjust two parameters: the number of grid points N and the fractional tolerance of the ODE solver. (Roughly speaking, the tolerance controls the accuracy of the numerical solution.) We find that a tolerance of 10^{-6} is more than adequate, and, in the vast majority of cases, taking $N = 400$ is appropriate. No change in the results is observed by using greater values of N and so we can be confident that this grid spacing is adequately close. Counterintuitively, it is not necessarily true that a smaller value of N will lead to a shorter run time. Faster convergence may be achieved by increasing N as this gives a more accurate representation of the concentration profile in the melt.

3.3.5 Effective viscosity

Before we discuss the results of the model it is appropriate to introduce a quantity which we shall refer to as the *effective viscosity*, η_{eff}. If we were to imagine the viscosity in the melt shell to be spatially constant, then η_{eff} is that viscosity which would give the observed bubble growth rate at a particular time. From Proussevitch et al. (1993a), the hydrodynamic equation in the case of constant viscosity (ignoring surface tension and inertia) is:

$$p_g = p_\infty + 4\eta \frac{\mathrm{d}R}{\mathrm{d}t} \left(\frac{1}{R} - \frac{R^2}{S^3} \right) \tag{3.30}$$

Melt density	2300 kg m^{-3}
Temperature	$800°\text{C}$
Initial bubble radius	10^{-5} m
Initial shell radius	10^{-3} m
Initial water content in melt	5 wt.%
Final pressure	10^5 Pa
Viscosity model	Hess and Dingwell (1996) (eq. 3.17)
Diffusivity model	Zhang and Behrens (2000) (eq. 3.18)
Equation of state	Pitzer and Sterner (1994) (eq. 3.10)
Solubility model	Zhang (1999b) (eq. 3.13)

Table 3.2: The base model. Parameter space is explored by varying just one or two parameters at a time around these values. These parameters were chosen to represent the typical conditions of an explosive volcanic eruption with rhyolitic melt.

Comparing equations 3.30 and 3.8 we obtain:

$$
\begin{aligned}
\eta_{\text{eff}} &= \frac{3}{R^{-3} - S^{-3}} \int_{R_0}^{S_0} \frac{\eta(X) X^2}{(R^3 - R_0^3 + X^3)^2} \, \mathrm{d}X \\
&= \frac{3 R^3 (S_0^3 - R_0^3 + R^3)}{S_0^3 - R_0^3} \int_{R_0}^{S_0} \frac{\eta(X) X^2}{(R^3 - R_0^3 + X^3)^2} \, \mathrm{d}X
\end{aligned}
\tag{3.31}
$$

using $S^3 = S_0^3 - R_0^3 + R^3$ (equation 3.4).

3.4 Results

In all model runs, we allow bubble growth to proceed to a vesicularity ($= R^3/S^3$) of 99%—in an explosive volcanic eruption we expect that magma will usually have fragmented at between 60 and 80% vesicularity (e.g. Thomas et al. 1994; Gardner et al. 1996). Model runs are based around the set of parameters in table 3.2. Initially, we choose a large, instantaneous decompression from the saturation pressure of 5 wt.% water (140 MPa) to atmospheric pressure. This is unlikely to occur in nature; however, such extreme conditions highlight the important effects which we shall be discussing. We shall show later that these effects are also important for more realistic situations.
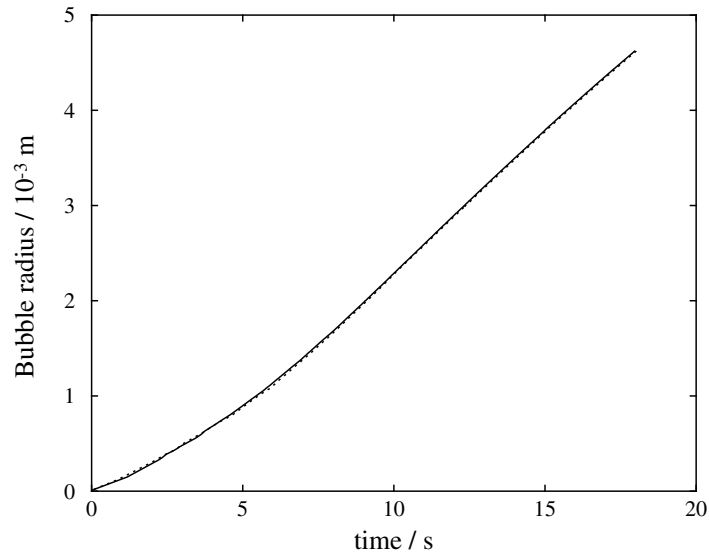
Figure 3.3: Bubble radius as a function of time using the parameters in table 3.2. The system reaches 99% vesicularity after 18.1s. The solid line represents bubble growth using the Pitzer–Sterner (1994) equation of state. The dashed line represents bubble growth assuming that water vapour behaves as an ideal gas. The two lines are very nearly coincident, and so the bubble growth dynamics are insensitive to the choice of equation of state.

Figure 3.3 shows the bubble radius as a function of time with the base parameters of table 3.2. The bubble reaches only 58.5% of its equilibrium radius at 99% vesicularity. We shall now investigate the sensitivity of the bubble growth dynamics to variation in the base parameters.

3.4.1   The influence of the equation of state of water

In the base model, we use the equation of state for water of Pitzer and Sterner (1994). Most previous bubble growth models assume that water behaves as an ideal gas. At high gas densities the ideal gas assumption may be a poor approximation. At a water vapour density of 1.57×10^4 $\mathrm{mol\,m^{-3}}$ at 800°C the ideal gas law predicts that the vapour will exert a pressure of 140 MPa (the saturation pressure of 5 wt.% water), whereas equation 3.10 gives a vapour pressure of 117 MPa. Figure 3.3 reveals that, in fact, the model is very

insensitive to the chosen equation of state.

3.4.2 The influence of the solubility law

We investigate two laws governing the solubility of water in rhyolitic melt. In most model runs we use the Zhang (1999b) model (equation 3.13). Many previous models have used Henry's square-root law (equation 3.16). Indeed the model of Zhang (1999b) gives relationships between solubility and pressure which are very close to a square-root relationship with a temperature-dependent Henry's constant α. For example, at 800°C, equation 3.16 with a value of $\alpha = 4.08 \times 10^{-6}$ Pa$^{-1/2}$ approximates very well Zhang's model from 0.1 to 140 MPa (figure 3.4a); this is very close to the value of 4.1×10^{-6} Pa$^{-1/2}$ which is often used in numerical models (e.g. Jaupart and Allègre 1991; Melnik and Sparks 1999).

Figure 3.4b compares results from runs using equation 3.13 and Henry's law with various values of the Henry constant α. Despite the good fit of the Zhang (1999b) model to a Henry's law curve with $\alpha = 4.08 \times 10^{-6}$ Pa$^{-1/2}$ there is a significant and systematic difference between the bubble growth curves using the two models. The reason for this lies in the difference between the solubilities predicted by the two models at low pressures. At 0.1 MPa and 800°C, equation 3.13 predicts that 0.10 wt.% water is soluble in the melt. Henry's law (equation 3.16) with $\alpha = 4.08 \times 10^{-6}$ Pa$^{-1/2}$ gives a solubility of 0.13 wt.%. This small difference has a relatively large effect on the melt viscosity near the bubble wall. Zhang's model gives $\eta = 2.3 \times 10^{10}$ Pa s at the bubble wall compared with 1.1×10^{10} Pa s for the Henry's law model— a difference of a factor of two. We shall see later (section 3.4.3) that the viscous resistance to bubble growth is strongly controlled by the viscosity near the bubble. Decreasing α decreases the water concentration, and hence raises the viscosity, at the bubble wall, retarding bubble growth.

From figure 3.4 we see that Zhang's model gives a bubble growth rate somewhere between those given by $\alpha = 3 \times 10^{-6}$ and 3.75×10^{-6} Pa$^{-1/2}$. These values, however, are rather
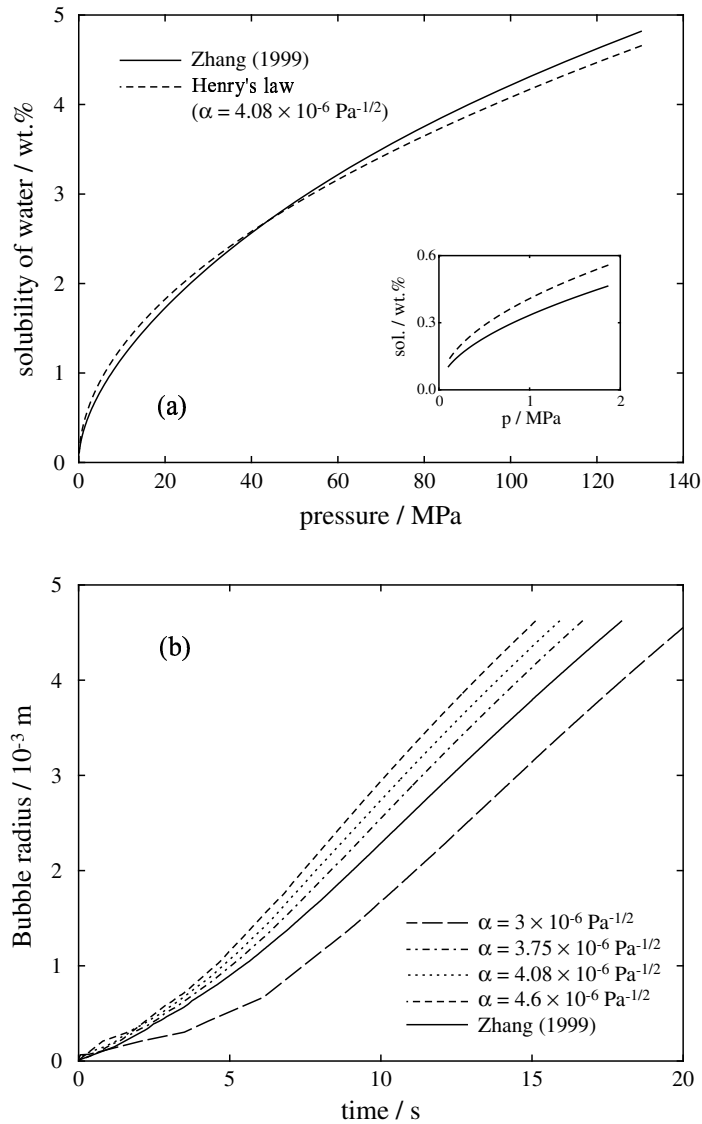
Figure 3.4: (a) Comparison of Zhang's (1999b) model of the solubility of water in rhyolitic melts with Henry's law at 800°C. With a Henry constant of 4.08×10^{-6} Pa$^{-1/2}$ the fit to Zhang's model over the pressure range 0–140 MPa is good. However, at low pressures (inset) the two models deviate: at atmospheric pressure the solubility of water according to Zhang's model is 0.10 wt.%, a value given by Henry's law with $\alpha = 3.21 \times 10^{-6}$ Pa$^{-1/2}$. This low value of the Henry constant gives a poor fit over the rest of the pressure range. (b) The effect of the solubility law on the bubble growth dynamics. Henry's law with $\alpha = 4.08 \times 10^{-6}$ Pa$^{-1/2}$ gives a gives a faster growth rate than Zhang's model, however, due to the slight increase in solubility at low pressure, giving a lower melt viscosity near the bubble wall. As α decreases, the bubble growth rate decreases due to the lower water concentration and higher viscosity near the bubble wall.

lower than typical measured values of α reported in the literature (e.g. 4×10^{-6} $Pa^{-1/2}$ in Proussevitch and Sahagian 1998; $\sim 4.4 \times 10^{-6}$ $Pa^{1/2}$ in Lyakhovsky et al. 1996). This illustrates the importance of using the correct solubility law. It is very important to constrain accurately the solubility of water in rhyolitic melt at low pressures.

3.4.3 The control of viscosity

Previous studies of bubble growth in highly viscous melts (Lyakhovsky et al. 1996; Navon et al. 1998) predict that, during an explosive eruption, viscosity controls the bubble growth dynamics in the initial stages of growth, when diffusion is efficient. This viscosity-controlled period is characterized by accelerating, exponential growth (Navon et al. 1998). After this stage, the pressure in the bubble falls to near-ambient and growth is limited by the diffusive flux of volatile molecules into the bubble. These studies, however, neglect the effect of volatile-dependent viscosity; as volatiles diffuse into the bubble, the viscosity of the dehydrated melt shell around the bubble increases. We might expect, therefore, that the control of viscosity will extend for longer times than is predicted by models which ignore this viscosity increase (Proussevitch and Sahagian 1998).

Figure 3.5 plots the bubble radius as a function of time for various constant viscosities. Above a viscosity of $\sim 10^3$ $Pa\,s$ the bubble growth rate is significantly retarded with increasing viscosity. Figure 3.5 also illustrates the effect of taking volatile-dependent viscosity into account. Although the starting viscosity in this case is 6.5×10^4 $Pa\,s$, the bubble growth rate in the case of variable viscosity is between those given by constant viscosities of 10^5 and 10^6 $Pa\,s$. This is due to the rapid dehydration and stiffening of the melt near the bubble wall. Clearly viscosity exerts a strong control over the bubble growth dynamics, as changing the viscosity law affects not only the rate of bubble growth, but also the overall form of the growth curve. When viscosity is assumed constant, the model reveals a period of accelerating (diffusion-driven, viscosity-limited) growth, followed by
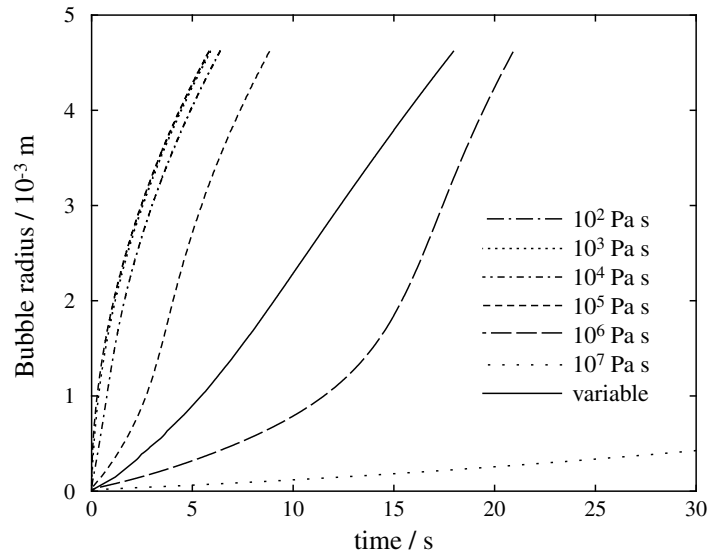
Figure 3.5: Bubble radius as a function of time with variable viscosity and various values of constant viscosity η. If $\eta \gtrsim 10^3$ Pa s viscosity plays a major role in controlling the bubble growth dynamics. If viscosity is allowed to vary with water concentration (equation 3.17) the bubble growth rate is somewhere between those given by constant viscosities of 10^5 and 10^6 Pa s, despite the fact that the starting viscosity is 6.5×10^4 Pa s.

decelerating (diffusion-limited) growth (cf. Proussevitch et al. 1993a, Navon et al. 1998). The effect of introducing volatile-dependent viscosity is to smooth out these inflexions in the curve to give a growth law which is closer to linear in form.

The evolution of effective viscosity

Figure 3.6 plots the evolution of the effective viscosity (section 3.3.5) as a function of time and bubble radius for the base parameters in table 3.2. It can be seen that, from an initial uniform viscosity of 6.5×10^4 Pa s, the effective viscosity rises rapidly to a viscosity of $\sim 3 \times 10^5$ Pa s and remains close to this value for several seconds. This agrees with figure 3.5 which shows that the growth rate under concentration-dependent viscosity is between those given by constant viscosities of 10^5 and 10^6 Pa s.

The form of the curve in figure 3.6 is consistent over a wide range of conditions (e.g.
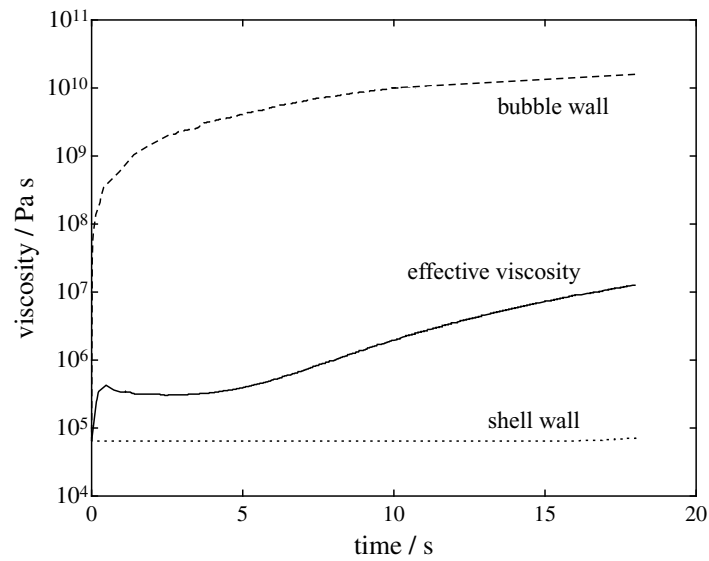
Figure 3.6: The evolution of the effective viscosity η_{eff} (solid line) as a function of time up to 99% vesicularity for the base parameters in table 3.2. The shape of this curve is discussed in section 3.4.3. Generally, η_{eff} increases with time as the melt dehydrates and stiffens. This increase is partially compensated by the increase of the bubble radius R which tends to decrease η_{eff} (equation 3.31). Note the temporary decrease in η_{eff} at $t \sim 2$ s. The viscosities at the bubble wall (dashed line) and the shell wall (dotted line) are also shown.

figure 3.9) and merits more explanation. The effective viscosity increases sharply in the initial stages ($t < 1$ s) of growth. At intermediate times, the effective viscosity is near-constant. Finally the effective viscosity steadily increases. This curve owes its shape to a competition between the dehydration of the melt, which tends to increase η_{eff} (see section 3.4.3), and the increase in bubble radius R, which tends to decrease η_{eff}. The pre-integral factor of equation 3.31 increases strongly with time due to the factor of R^6 in the numerator. The integral factor decreases with time— the increase in $\eta(X)$ is more than compensated for by the factor of R^6 in the denominator. The net result depends on the conditions of bubble growth, leading to the unexpected result that the effective viscosity can actually decrease slightly at certain times in the evolution (figure 3.6).

The influence of the dehydration zone around the bubble

We now examine whether the viscous resistance to bubble growth is caused by the conditions near to or far from the bubble. We define

$$g(X) = \int_{R_0}^{X} \frac{\eta(X)X^2}{(R^3 - R_0^3 + X^3)^2}\, \mathrm{d}X \bigg/ \int_{R_0}^{S_0} \frac{\eta(X)X^2}{(R^3 - R_0^3 + X^3)^2}\, \mathrm{d}X \qquad (3.32)$$

This is the fractional contribution to the integral term of the effective viscosity from $X = R_0$ to X. In figure 3.7a we plot $g(X)$ versus X for bubble growth using the base parameters at $R = 1$ mm. (See the solid line on figure 3.10b for the corresponding viscosity profile.) It is clear that the dehydrated, highly viscous ($\eta = 4.6 \times 10^9$ Pa s) melt near the bubble exerts the major control on the integral term. The melt in the far field has a viscosity of 6.5×10^4 Pa s and makes little contribution. By contrast, in the case of constant viscosity at the same bubble radius (figure 3.7b), the melt near the bubble contributes little to the integral factor. (This will depend on the bubble radius. If X is larger than R and η is constant then the integrand will decrease with increasing X due to the X^6 term in the denominator.)
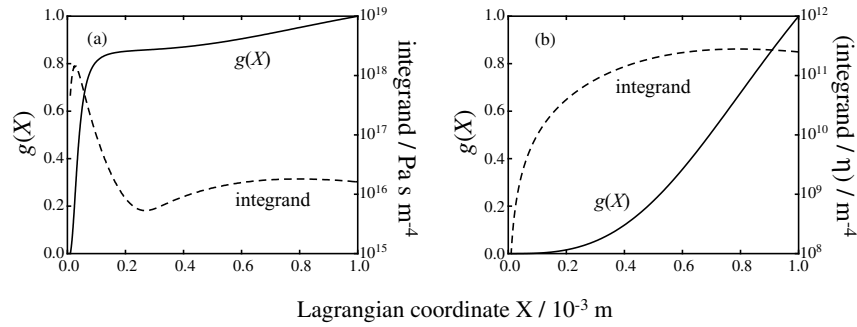
Figure 3.7: The contribution of parts of the melt shell to the integral term in the case of (a) variable viscosity and (b) constant viscosity. $g(X)$ (equation 3.32) is the fractional contribution to the integral term of the effective viscosity (equation 3.31). The integrand $\left(\frac{\eta(X)X^2}{(R^3-R_0^3+X^3)^2}\right)$ of $g(X)$ is also plotted. With variable viscosity the viscous melt near the bubble dominates the integral term. This shows that, in the case of variable viscosity, the largest contribution to the integral term comes from the melt near to, but not directly adjacent to the bubble (at $X \sim 0.03 \times 10^{-3}$ m in this case).

The thin, dehydrated melt shell around the bubble therefore has a large influence on the viscous resistance experienced by the bubble. This is compensated for by the increase in the bubble radius— the larger the bubble, the smaller the effect of the viscous resistance related to the dehydrated region.

3.4.4 The control of diffusivity

Figure 3.8 shows bubble growth curves for different values of (constant) diffusivity. As expected, choosing a high value of diffusivity leads to faster bubble growth. We must conclude from figures 3.5 and 3.8 that bubble growth dynamics are controlled by *both* viscosity and diffusivity in the parameter regime given in table 3.2.

This dependence of the growth rates on both viscosity and diffusivity leads to an unexpected and hitherto undocumented feature of the growth dynamics. When variable diffusivity according to equation 3.18 is specified (figure 3.8), the bubble growth rate is somewhere between those given by constant diffusivities of 1×10^{-11} and 3×10^{-11} m^2 s^{-1}.
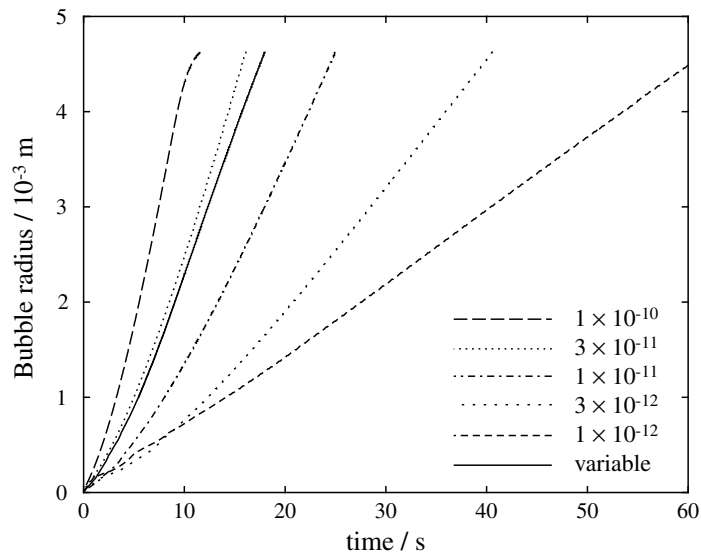
Figure 3.8: The effect of diffusivity on the dynamics of bubble growth. All other parameters and models are those given in table 3.2. Concentration-dependent diffusivity (solid line) gives a bubble growth rate somewhere between those given by constant diffusivities of 1×10^{-11} and 3×10^{-11} m^2 s^{-1}, despite the fact that the actual diffusivity during the run varied from 2.4×10^{-13} to 7.4×10^{-12} m^2 s^{-1}. This apparently anomalously high bubble growth rate is due to a lower effective viscosity in the case of concentration-dependent diffusivity (figure 3.9).

We might, on first inspection, define an 'apparent diffusivity' of, say, 2×10^{-11} m^2 s^{-1}. This apparent diffusivity, however, bears no relation to the actual diffusivity of water in the melt which is much lower, ranging between 7.4×10^{-12} and 2.4×10^{-13} m^2 s^{-1}.

The explanation of this counterintuitive result lies in the interplay between diffusivity and viscosity. The higher the value of diffusivity, the faster the dehydration of the melt shell. In terms of bubble growth rates, therefore, slow diffusion rates tend to be compensated by a low melt viscosity. In the case of constant diffusivity (figure 3.8) choosing a lower diffusivity leads to a decrease in bubble growth rate; the decrease in mass transfer rate 'wins' over the decrease in melt viscosity. With variable diffusivity, however, low values of diffusivity are more than compensated by the low melt viscosity and the bubble growth rate is unexpectedly high.

We may investigate this further by examining the effective viscosity (equation 3.31) during the model runs in figure 3.8. Figure 3.9a plots the effective viscosity as a function of time and shows that, indeed, the effective viscosity of the melt shell is relatively low in the model run using the variable diffusivity law of equation 3.18. The effective viscosity depends not only on the concentration profile in the melt, but also on the bubble radius. A plot of η_{eff} versus bubble radius (figure 3.9b) is more instructive for comparison of the conditions at a particular stage of growth. With variable diffusivity, the effective viscosity at a given bubble radius is reduced by between half and one order of magnitude compared with all investigated values of constant diffusivity. We see that all values of constant diffusivity give very similar curves, but this is a coincidence and only occurs with an initial water content of 5 wt.%— at lower initial water concentrations these curves become distinct.

Figure 3.10 plots the concentration and viscosity profiles in the melt with variable diffusivity, and various values of constant diffusivity, at a bubble radius of 1 mm. In the case of variable diffusivity, the water concentration (figure 3.10a) near the bubble wall is higher than for any of the plotted values of constant diffusivity. Since viscosity is very sensitive
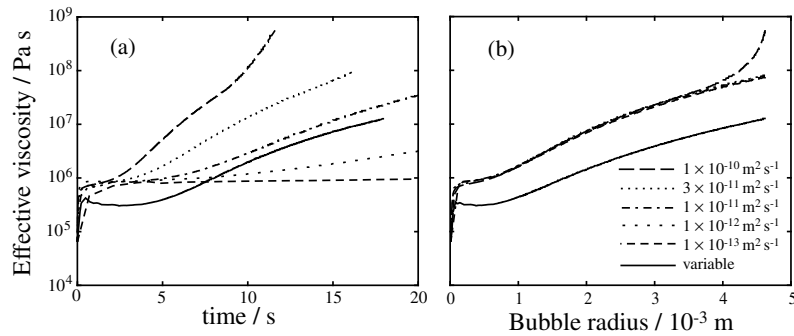
Figure 3.9: (a) The evolution of effective viscosity (equation 3.31) with time during the model runs of figure 3.8, showing the first 20 seconds of growth. (b) Effective viscosity versus bubble radius. In the case of variable diffusivity (equation 3.18) the effective viscosity is held at a lower value than with any value of constant diffusivity.
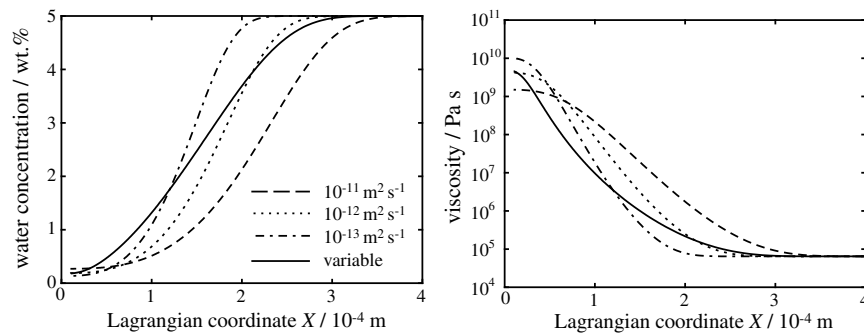
Figure 3.10: Profiles of (a) water concentration and (b) viscosity in the melt shell with variable diffusivity and various values of constant diffusivity. The bubble radius is the same (1 mm) for all curves, giving a vesicularity of 50%.

to water content, especially at low water contents (Hess and Dingwell 1996), the viscosity near the bubble is significantly reduced (figure 3.10b), leading to an overall reduction in η_{eff}.

3.4.5 The effect of temperature

Many parameters of the model — solubility (equation 3.13), diffusivity (equation 3.18) and viscosity (equation 3.17) — are temperature-dependent. We have seen how varying
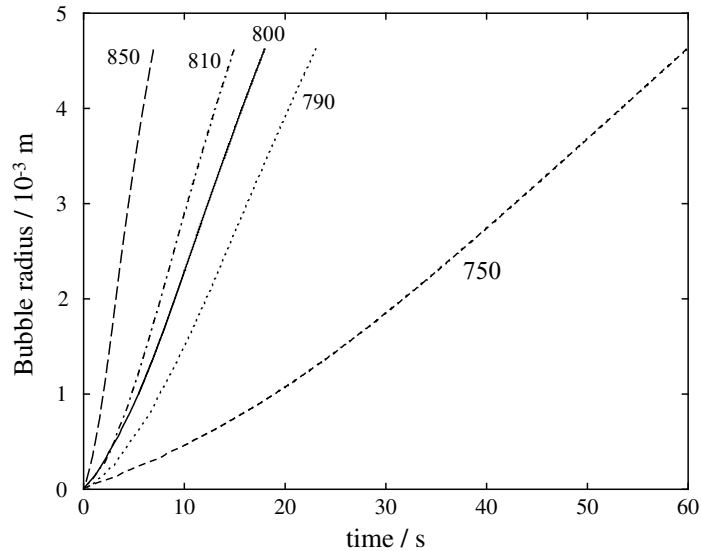
Figure 3.11: The effect of temperature on the bubble growth dynamics. Labels are the temperature in Celsius. The sensitivity to temperature of the melt viscosity leads to a significant variation in the bubble growth rate over a relatively narrow temperature range.

each of these parameters individually affects the results of the model. It is instructive to investigate to what extent the model as a whole is sensitive to temperature. Figure figure 3.11 shows results from runs performed at temperatures from 750 to 850°C. At 750°C, the system reaches 99% vesicularity after 59.9 seconds. Growth at 850°C is nearly an order of magnitude more rapid, with the system reaching 99% vesicularity after 6.9 seconds.

3.4.6 The effect of the initial pressure

So far we have simulated an instantaneous decompression from the saturation pressure of 5 wt.% water ($\sim$ 140 MPa) to atmospheric. This is an unrealistically rapid and extreme depressurization. We investigate the effects of smaller, yet still instantaneous, pressure
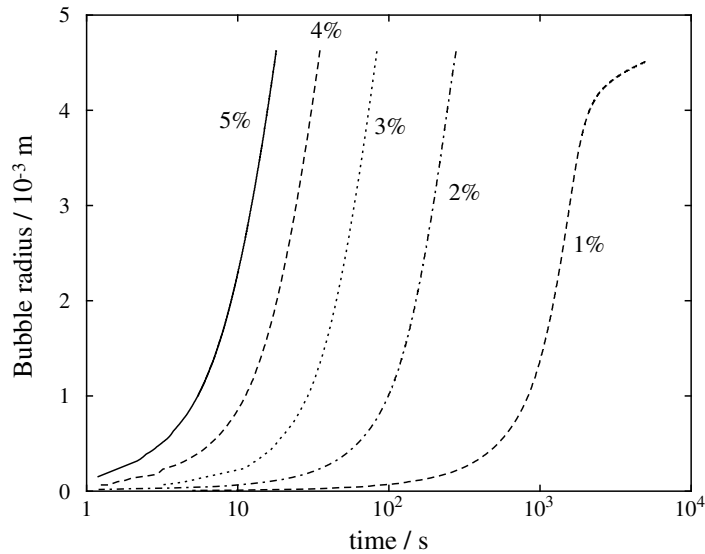
Figure 3.12: The effect of the initial water content on bubble growth dynamics. The curves are labelled with the initial water content in weight percent. Note the logarithmic time axis. All other parameters are given in table 3.2.

drops by varying the initial water concentration in the melt. We investigate initial water contents of 3 wt.% (saturation pressure $\sim$ 53 MPa) and 1 wt.% (saturation pressure $\sim$ 7.6 MPa).

The analysis of Proussevitch et al. (1993a) revealed the counterintuitive result that the higher the initial water concentration in the melt, the shorter the time required to reach the equilibrium bubble radius. This was attributed to steep concentration gradients near the bubble wall — and hence fast mass transfer — in the case of high volatile contents. This general result is also revealed by our model (figure 3.12), but the effect is even more marked due to the incorporation of concentration-dependent viscosity. High water contents not only give steep concentration gradients but also lower melt viscosity and hence faster growth.

The initial water content has a large influence on the magnitude of the anomalous diffusivity effect discussed in section 3.4.4. The value of the 'apparent diffusivity' decreases with
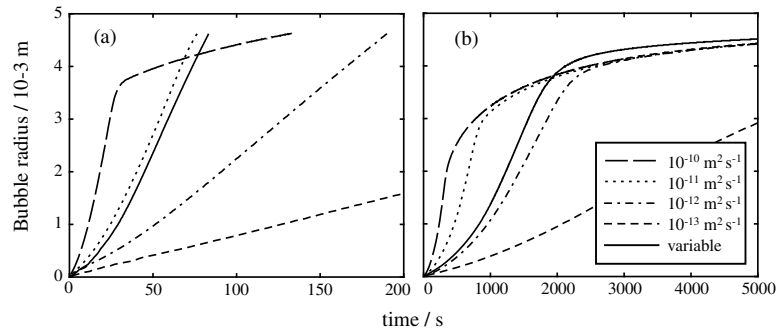
Figure 3.13: Bubble growth curves using concentration-dependent diffusivity and various values of constant diffusivity with initial water contents of (a) 3 wt.% and (b) 1 wt.%. The value of the 'apparent diffusivity' (section 3.4.4) using variable diffusivity decreases with decreasing initial water content.

decreasing initial water content. At 5 wt.% water the apparent diffusivity is just less than 3×10^{-11} m^2 s^{-1} (figure 3.8). If the initial water content is 3 wt.% the apparent diffusivity is just under 10^{-11} m^2 s^{-1} (figure 3.13). An initial water content of 1 wt.% gives an apparent diffusivity of just greater than 10^{-12} m^2 s^{-1}. Examination of the effective viscosity in these cases reveals that the lower the initial water content, the smaller the contrast in η_{eff} between model runs using constant and variable diffusivity. For instantaneous pressure drops of a few megapascals, therefore, the 'anomalous diffusivity' effect is very slight.

3.5   The effect of a finite rate of pressure drop

So far we have assumed that depressurization is instantaneous. We now investigate the effects of a linear pressure drop from the saturation pressure to atmospheric pressure. Several studies (summarized in Proussevitch and Sahagian 1996) suggest that magma ascent velocities can reach several metres per second before fragmentation. Figure 3.14 shows the bubble growth dynamics in the case of a constant ascent rate of 10 m s^{-1} ($= 0.2$ MPa s^{-1}). For much of its ascent, the growth of the bubble is controlled by the decompression. When the bubble nears the surface, however, its growth accelerates
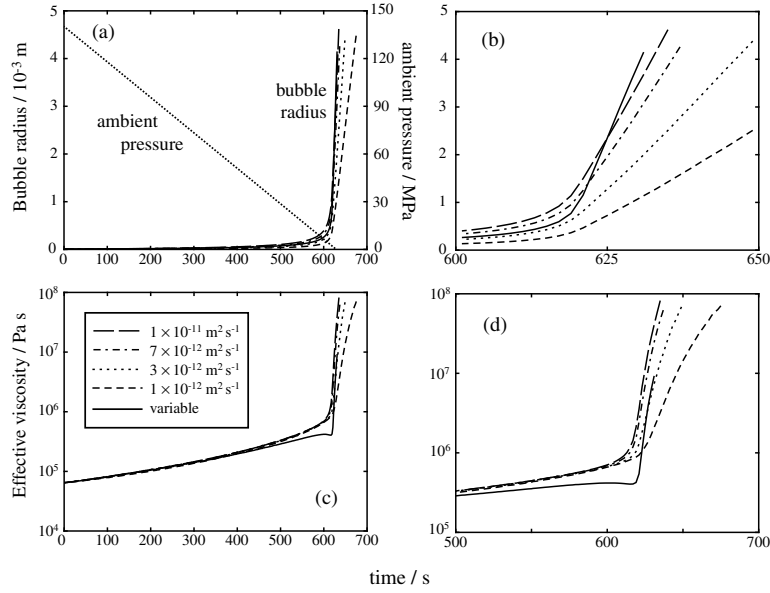
Figure 3.14: Bubble growth due to a linear pressure drop (equivalent ascent rate of $10~\mathrm{m\,s^{-1}}$), comparing growth with various values of constant diffusivity with growth under concentration-dependent (variable) diffusivity. Pressure drops linearly to atmospheric pressure where it remains constant. (a) Bubble radius and ambient pressure as a function of time. Growth rates increase rapidly at low pressures. (b) Closer view of the range $600 \leq t \leq 650$ s. In the case of concentration-dependent diffusivity bubble growth rates are enhanced. This is due to the lower effective viscosity in the case of concentration-dependent diffusivity (c). (d) shows a closer view of the effective viscosity in the range $500 \leq t \leq 700$ s. Note that η_{eff} undergoes a slight decrease at $t \sim 600$ s.

rapidly and the control of diffusion starts to take effect. We now see the same 'anomalous diffusivity' effect as described in section 3.4.4. With concentration-dependent diffusivity bubble growth rates are enhanced compared with values of constant diffusivity of similar magnitude. Figure 3.14 (c and d) shows that this is again due to a lower effective viscosity in the case of concentration-dependent diffusivity.

The same effects of reduced effective viscosity and enhanced bubble growth rates are also observed for an ascent velocity of $1~\mathrm{m\,s^{-1}}$ ($0.02~\mathrm{MPa\,s^{-1}}$) but the magnitude of the effects is much reduced. A slow depressurization means that degassing can remain close to equilibrium with the ambient pressure and so volatile diffusivity exerts a smaller control on the growth dynamics.

3.6 Conclusions

A numerical model has been developed and applied to investigate the dynamics of bubble growth in rhyolitic magmas under the conditions of an explosive eruption. The model has been used to investigate the sensitivity of the dynamics of bubble growth to many model parameters. We have particularly focused on the effects of incorporating concentration-dependent viscosity and diffusivity into the model. The main results of the study are:

- The dynamics of bubble growth are strongly controlled by both viscosity and diffusivity.

- A high value of diffusivity causes a rapid dehydration and stiffening of the melt shell. The resulting high viscosity partially counteracts the high rate of diffusive mass transfer.

- For constant diffusivity, high diffusivities lead to fast growth rates. In the case of concentration-dependent diffusivity, bubble growth rates are enhanced compared with rates given by constant diffusivities of similar magnitude, due to a reduction in effective viscosity. This effect is most pronounced for conditions which favour non-equilibrium degassing, i.e. high initial water contents (high initial pressures) and rapid magma ascent rates.

- The viscous resistance of the melt is dominated by the viscous, dehydrated region near the bubble. As the bubble grows the effect of this viscous resistance decreases.

- The model is sensitive to the boundary condition at the bubble/melt interface (the solubility law condition). Small variations in this boundary condition lead to relatively large changes in the bubble growth rates. This is due to the sensitivity of the melt viscosity to water concentration at low concentrations.

- The dynamics of bubble growth are insensitive to the choice of equation of state for

water vapour.

The model assumes that there are no crystals in the melt and that the melt has zero yield strength (Newtonian viscosity). Another major assumption is that the initial water concentration in the melt is uniform; this is unlikely to be the case in a natural system. Liu and Zhang (2000) investigated bubble growth experimentally and found marked variations in bubble growth rate, which they attributed to an inhomogeneous distribution of volatiles.

3.6.1 Implications for modelling volcanic processes

The most important conclusion of this study is that concentration-dependent viscosity and diffusivity play a major role in the dynamics of bubble growth. The effects of viscosity and diffusivity are highly coupled and many important features of the dynamics of bubble growth in explosive volcanic eruptions cannot be captured if either of these factors is assumed constant. Most models of volcanic conduit flow incorporate a *temporally*-varying viscosity (e.g. Papale et al. 1998; Melnik and Sparks 1999); they assume that degassing proceeds in equilibrium with the falling pressure and calculate the viscosity of the melt based on the equilibrium volatile concentration and the vesicularity. This progressive increase in viscosity on degassing has a profound effect on the large-scale conduit flow; Wilson (1998) showed that the viscosity increase can lead to dynamical instabilities in the flow, causing large-scale overturning of the melt in the conduit. Wylie et al. (1999) discovered an oscillatory regime of magma flow due to volatile-dependent viscosity.

All current conduit flow models, however, neglect the fact that the viscosity will vary *spatially* within the melt due to the dehydration zones around bubbles. In this chapter, an effective viscosity was defined to provide a convenient single parameter which describes the viscous resistance felt by the bubbles in a liquid whose viscosity decreases with distance from each bubble. This cannot, however, be used directly as an effective resistance to large-

scale shear flow in a volcanic conduit. To my knowledge, there has been no examination of the rheology of a bubbly liquid whose viscosity varies with the spatial distribution of volatile molecules around each bubble. The relatively rigid, viscous skins around each bubble might cause the bubbles to behave as hard spheres in the flow, rather than void spaces.

The effects of concentration-dependent viscosity and diffusivity are most marked under conditions of highly non-equilibrium degassing. If decompression rates are slow and the volatile concentration in the liquid is everywhere in equilibrium with the ambient pressure then the viscosity is also uniform and the value of the volatile diffusivity is, by definition, irrelevant. However, there is no way of determining whether degassing can proceed in equilibrium with the falling pressure without implementing a full solution of the diffusion of volatiles through the melt— in other words, a bubble growth model is required.

In a model of large-scale eruption dynamics, therefore, the nature of degassing (equilibrium or non-equilibrium) should not be assumed but calculated. Furthermore, in models of bubble growth, the rate of depressurization should be calculated, not specified *a priori*. Both these goals could be achieved by linking models of conduit flow with a model of bubble growth. The formulation of the bubble growth model in this chapter provides an easy way to join the two models; the ambient pressure (currently specified by equation 3.29) could be the output of a conduit flow model. The bubble growth model could then feed values of the bubble radius and the melt viscosity back to the conduit flow model.

The sensitivity of the dynamics of bubble growth to the melt viscosity leads to a potentially serious obstacle to accurate modelling of volcanic processes. Liu and Zhang (2000) showed that bubble growth rates observed in laboratory experiments could only be reproduced by the numerical model of Proussevitch and Sahagian (1998) if they multiplied the value of the melt viscosity as calculated by the model of Hess and Dingwell (1996) by some arbitrary factor, within the error of the parameterization. This factor was found by fitting

the experimental data; it could not be calculated *a priori*. Furthermore, the 'viscosity factor' was different for each bubble in a given experiment. This illustrates that even the apparently small errors in the best parameterizations of melt properties can lead to large uncertainties in the growth rates of bubbles, and hence the expansion rates of magma.

Chapter 4

Permeability–porosity relationships in volcanic rocks and magma

4.1 Summary

A model has been developed to calculate the permeability k of magma and to test its sensitivity to various parameters. Power-law relationships between k and porosity ϕ are revealed, in agreement with previous experimental and theoretical studies. These relationships take the form $\hat{k} = k/r^2 = a(\phi - \phi_{cr})^b$ where r is the mean bubble radius, ϕ_{cr} is the percolation threshold below which permeability is zero, and a and b are constants. It is discovered that $\hat{k} - \phi$ relationships are independent of bubble size. The percolation threshold was found to lie at about 30% porosity. Polydisperse bubble size distributions give permeabilities about an order of magnitude greater than monodisperse distributions at the same porosity. If bubbles are elongate in a preferred direction then permeability in this direction is increased but, perpendicular to this direction, permeability is unaffected. In crystal-free melts the greatest control on permeability is the ease of bubble coalescence. In viscous magmas, or when the cooling timescale is short, bubble coalescence is impeded and permeability is much reduced. This last effect can cause variations in permeability of

several orders of magnitude.

4.2 Introduction

A common feature of many volcanic eruptions is that they exhibit diverse eruptive styles. The eruption of Mount St. Helens, for example, commenced with a highly explosive phase of Plinian and pyroclastic flow activity on May 18 1980, triggered by a landslide which decapitated the volcanic edifice. This explosive phase was followed by a period of effusive dome growth; the dome was destroyed by another explosive phase and a new dome grew in its place which was also removed by explosive activity. A third phase of dome growth followed which continued until the eruption ceased in 1986. The ongoing eruption of Montserrat has also seen several phases of alternating explosive and effusive activity.

It is clearly of paramount importance for the prediction and mitigation of volcanic hazards to understand the mechanisms which cause these transitions between explosive and effusive activity. An early proposal was that the changes in eruptive style reflect the progressive emptying of a magma chamber which is stratified with respect to volatile content (e.g. Fink 1983). Explosive activity occurs when volatile-rich magma is sampled from the chamber; the eruption of volatile-poor magma leads to effusive activity.

The explanation of volatile stratification is not, however, supported by petrological evidence. It is commonly discovered that the products of explosive and effusive phases of the same eruption are petrologically identical, even if they are texturally different. For example, Barclay et al. (1996) measured the volatile contents of melt inclusions within quartz and feldspar phenocrysts in rhyolites from Mayor Island, New Zealand. Despite the fact that the samples represented a wide variety of eruptive styles, the water content of all the inclusions was ~ 4.4 wt.%. Samples from both explosive and effusive phases of the Mount St. Helens (1980–1986) eruption contain phenocrysts of amphibole (Ruther-

ford and Hill 1993); amphibole is only stable in magmas with high water contents (greater than ~ 4 wt.% for Mount St. Helens dacite, Rutherford and Hill 1993). Amphibole is also present as phenocrysts in samples of both explosion-derived pumice and dome lava from the ongoing eruption of Montserrat (Barclay et al. 1998) and is indicative of initial water pressures of > 115 MPa, in agreement with measured water contents of ~ 4.4 wt.% in melt inclusions.

There is therefore very strong evidence that the changes in the eruptive style in these eruptions were not controlled by variations in the pre-eruptive volatile content of the magma. It is now widely accepted that gas can escape from the volcanic system during an eruption (Jaupart 1998), thus reducing the volume fraction of gas in the ascending magma and preventing fragmentation. This is *open-system* behaviour and contrasts with many numerical models of conduit flow (e.g. Papale et al. 1998; Melnik 2000) which assume that no gas is lost from the magma during an eruption (*closed-system* behaviour).

A simple calculation reveals that closed-system degassing is unlikely to result in effusive activity. We shall estimate the maximum amount of dissolved water which is expected to result in an effusive eruption with closed-system degassing. Let us assume that magma is initially saturated in water at pressure P_1. The magma reaches the surface at atmospheric pressure P_{atm}, vesiculating as it ascends. Assuming that degassing proceeds in equilibrium with the falling pressure according to Henry's law, the mass fraction of water c in the melt at pressure P is given by $c = \alpha\sqrt{P}$ where α is the Henry constant. The mass fraction of water released on depressurization is therefore $\alpha(\sqrt{P_1} - \sqrt{P_{atm}})$. Assuming that the water vapour behaves as an ideal gas, the volume V of water vapour released per cubic metre of melt is:

$$V = \frac{\rho\alpha RT(\sqrt{P_1} - \sqrt{P_{atm}})}{M_g P_{atm}} \quad (4.1)$$

where ρ is the melt density, R is the gas constant, T is the temperature in Kelvin and M_g is the molar mass of water. The vesicularity ϕ of the melt is $V/(1+V)$. Let us assume that

the magma fragments and explosive activity occurs if magma reaches the surface with a vesicularity greater than 75%. This gives $V = \phi/(1 - \phi) = 3$. We may then calculate the initial saturation pressure (P_1) required to lead to explosive activity:

$$P_1 = \left(\frac{V M_g P_{\text{atm}}}{\rho \alpha R T} + \sqrt{P_{\text{atm}}} \right)^2 \tag{4.2}$$

For $V = 3$, $M_g = 0.018$ kg mol^{-1}, $P_{\text{atm}} = 0.1$ MPa, $\rho = 2300$ kg m^{-3}, $\alpha = 4.1 \times 10^{-6}$ Pa$^{-1/2}$, $R = 8.31$ J K^{-1} mol^{-1} and $T = 1073$ K, we obtain $P_1 = 0.14$ MPa, corresponding to an initial water content of 0.16 wt.%. This result was also calculated by Jaupart and Allègre (1991). Under closed-system degassing, therefore, explosive activity is expected even for relatively low initial water contents. It is observed, however, that effusive activity can arise from magma with much larger pre-eruptive water contents (e.g. 4.4 wt.% for the Mayor Island rhyolites, Barclay et al. 1996; 4.4 wt.% for Montserrat magma, Barclay et al. 1998). The most likely explanation of this discrepancy is that some gas is lost from the magma between the onset of vesiculation and eruption.

The above calculation is clearly over-simplified; there is no consideration of the fragmentation mechanism, for example, a key control on the transition between effusive and explosive activity. However, there are many other lines of evidence which support the existence of open-system behaviour in effusive volcanic eruptions:

- Field observations of volcanic activity often reveal that periods of effusive activity are associated with episodes of gas venting from the volcanic edifice (e.g. Casadevall et al. 1983).

- The systematics of deuterium (D) and hydrogen degassing are such that D and H are fractionated to different degrees under closed-system and open-system conditions. D:H ratios have been measured in samples from Little Glass Mountain, California by Taylor et al. (1983). Samples from pyroclastic deposits exhibited trajectories of

D:H versus H_2O which were consistent with closed-system degassing. By contrast, samples from effusive, dome-building phases were characterized by D:H data which indicated open-system degassing.

- Rutherford and Hill (1993) studied reaction rims in phenocrysts of amphibole in dacites from the 1980–1986 eruption of Mount St. Helens. These reaction rims were present in dome lavas, indicating that they had spent significant amounts of time outside their stability field before cooling. The presence of amphiboles is an indication of high (> 4 wt.%) initial water contents. As exsolution occurred and the water content of the melt dropped, the crystals partially redissolved. Since these exsolved volatiles were not present in the erupted magma, they must have escaped during ascent. Amphibole phenocrysts from pumices from Plinian phases show no reaction rims; the magma ascent rate was too rapid for amphibole to be resorbed.

- A rare and important exposure of a fossil conduit and vent at Mule Creek, New Mexico was described by Stasiuk et al. (1996). The rhyolite magma preserved in this conduit had an initial water content of $\sim 2.5 - 3.0$ wt.%, as evidenced by melt inclusions. The depth of conduit exposed was 300 m and simple closed-system models of degassing (such as equation 4.1) imply that the vesicularity of the magma should have been greater than 70% over the whole exposure. However, observed values of vesicularity were $\sim 20\%$ at 300 m depth and $\sim 40\%$ at depths shallower than 200 m. Vesicularities also decreased from the interior of the rhyolite to the edge, reaching zero at the conduit walls. The country rock was fractured and it appears very likely that gas was lost from the magma to the permeable walls of the conduit during the eruption. Bubbles near the conduit walls were observed to be aligned and connected, providing a path for gas flow from the interior of the magma to the conduit walls. The exposure at Mule Creek also preserves pumice fall deposits from an explosive phase which preceded the effusive eruption of lava. These pumices were petrographically similar to the samples of obsidian lava.

4.2.1 Models of gas loss during conduit flow

There are many lines of evidence to suggest that the style of an eruption (explosive or effusive) is largely controlled by whether degassing is an open- or closed-system process. This has been investigated in a more quantitative fashion by several authors, who have performed numerical simulations of conduit flow, incorporating syn-eruptive gas loss. This contrasts with many other numerical models of conduit flow in which degassing is assumed to be a closed-system phenomenon (e.g. Melnik 2000). I shall now discuss the main features and results of three of these models.

Jaupart and Allègre (1991)

The study of Jaupart and Allègre (1991) was the first to investigate the effects of gas loss on large-scale conduit flow dynamics and the eruptive style. They developed a numerical model in which the erupted mass flux of magma is calculated under the condition that the conduit wall is permeable. The main assumptions of the model are that the amount of volatiles degassed is given by a solubility condition (equilibrium degassing)— no attempt is made to model the kinetics of degassing (chapter 3); that the conduit is cylindrical and that fragmentation occurs at a vesicularity of 75%. The model is one-dimensional, considering only vertical variation in all parameters, and so quantities such as ascent velocity are horizontally averaged. The key equations of the model are now described briefly.

The mass flux of liquid G_l is given by:

$$G_l = \rho_l(1 - \phi)w \tag{4.3}$$

where ρ_l is the liquid density, ϕ is the volume fraction of gas in the bubbly liquid and w is the ascent velocity. The magma rises through a cylindrical conduit of radius a and, as it

rises, loses gas to the conduit walls at a rate (mass flux) q. Considering mass conservation of gas molecules:

$$\pi a^2 \left(\frac{\mathrm{d}}{\mathrm{d}z}[\rho_g w \phi] + \frac{\mathrm{d}}{\mathrm{d}z}[x \rho_l (1 - \phi) w] \right) = -2\pi a q \tag{4.4}$$

where z is the vertical coordinate, ρ_g is the gas density and x is the mass fraction of volatiles dissolved in the melt. The left hand side of equation 4.4 is the change in the total volatile content of the magma, accounting for both dissolved and exsolved gas. Equations 4.3 and 4.4 give:

$$\frac{\mathrm{d}\phi}{\mathrm{d}z} = (1 - \phi)^2 \frac{\rho_l}{\rho_g} \left(-\frac{\mathrm{d}P}{\mathrm{d}z} \left[\frac{\phi}{\rho_l(1 - \phi)} \frac{\mathrm{d}\rho_g}{\mathrm{d}P} + \frac{\mathrm{d}x}{\mathrm{d}P} \right] - \frac{2q}{G_1 a} \right) \tag{4.5}$$

where P is the pressure of the gas in the magma. This states that, as magma rises, the volume fraction ϕ of gas is increased by the exsolution of gas from the melt and the expansion due to decompression, and decreased due to gas loss to the conduit walls. The rate of gas loss is given by a form of Darcy's law of permeable flow:

$$q = \rho_g \phi k (P - P_L) \tag{4.6}$$

where P_L is the far-field pressure, taken to be lithostatic. The factor of ϕ in equation 4.6 accounts for the fact that the rate of gas loss will be proportional to the fraction of the conduit wall which is in contact with the gas phase. The effective permeability k of the conduit walls is a key factor in this equation— this was calculated based on estimates of the size and density of fractures in the conduit walls. Gas loss to the conduit wall can only occur if the conduit is overpressured with respect to the surrounding country rock. The existence of this overpressure is calculated by the model, not assumed *a priori*. The model also includes equations which describe momentum conservation in the cases of laminar flow (pre-fragmentation) and turbulent flow (post-fragmentation). The viscosity of the magma is calculated as simple functions of the dissolved water content and the volume fraction of bubbles.

The most important result of the model is that the eruptive behaviour at the vent is extremely sensitive to small changes in the initial pressure in the magma chamber. This is due to a strong positive feedback between ascent velocity and the rate of gas loss: If the ascent rate of magma slows slightly due to, perhaps, a small decrease in chamber pressure, there is more time for gas loss to the conduit walls. This leads to slower expansion of the magma and hence slower ascent rates. Therefore, the transition between explosive and effusive activity may be due to a gradual decrease in chamber pressure as the magma chamber is emptied. Replenishment of the magma chamber from depth may lead to a sudden transition from effusive to explosive activity.

Woods and Koyaguchi (1994)

Woods and Koyaguchi (1994) develop a model which is in many respects similar to that of Jaupart and Allègre (1991). The main differences between the two models are that Woods and Koyaguchi assume that the far-field pressure is *hydrostatic* and that the conduit permeability k is not constant but decreases with depth. An assumption of hydrostatic pressure in the far field tends to lead to higher gas fluxes than with lithostatic values; for the same depth, hydrostatic pressures are lower than lithostatic pressures.

Like Jaupart and Allègre (1991), Woods and Koyaguchi search for flow solutions for a given chamber pressure. Valid solutions are those which reach either atmospheric pressure (effusive solutions) or the speed of sound (explosive solutions) at the vent. A major feature of the results of this study is that *multiple* flow solutions are found for a given chamber pressure. In general, there are two distinct solutions which lead to effusive flow and one solution which leads to explosive activity. Above a chamber overpressure of 1.4 MPa only explosive solutions are possible. These multiple solutions are a result of the inherent non-linearity of the governing equations, but were not reported by Jaupart and Allègre (1991).

The model was used to investigate the expected eruption sequence if the magma chamber was supplied from depth from an unspecified source. (The ongoing eruption of the Soufrière Hills volcano, Montserrat is thought to have been triggered by an input of mafic magma from depth; Sparks et al. 1998; Murphy et al. 1998.) The pressure in the magma chamber is due to a competition between the input of magma from depth and the output to the conduit. Initially, the magma chamber is replenished from depth and magma is removed slowly, giving an effusive eruption. If the rate of input of magma to the chamber is greater than the rate of removal then the chamber pressure will slowly increase. When a certain overpressure is reached, a sudden transition to explosive activity takes place, rapidly draining the chamber and reducing the overpressure. Effusive activity then resumes. Hence complex cycles of effusive and eruptive activity are predicted, qualitatively similar to those observed at Mount St. Helens in the 1980–1986 eruption.

Melnik and Sparks (1999)

The model of Melnik and Sparks (1999) was developed to investigate the processes of lava dome formation, with particular application to the ongoing eruption of the Soufrière Hills volcano, Montserrat. They considered the dynamics of ascent of viscous magma, incorporating the effects of microlite crystallization and gas loss by permeable flow. The crystallization of anhydrous microlites (e.g. plagioclase) not only significantly increases the viscosity of the melt (Lejeune and Richet 1995) but also increases the concentration of dissolved gas in the residual melt causing further exsolution and increasing gas pressures (Sparks 1997). In contrast to the two models discussed above, Melnik and Sparks considered gas loss in a *vertical* direction only, based on the observation that, at the Soufrière Hills volcano, a vigorous gas plume was observed issuing from the summit of the dome. In their model, therefore, they included an equation describing the permeability of the magma to gas, based on measurements of the permeability of rock samples from the eruption.

The model predicted that the largest pressure in the system is not to be found in the magma chamber (at 5 km depth), but in the conduit at a depth of a few hundred metres. This was in agreement with calculations from ground deformation measurement at the Soufrière Hills volcano (Voight et al. 1998; Shepherd et al. 1998). The depth and magnitude of this conduit overpressure were only slightly dependent on the permeability of the magma. Once more, multiple solutions for discharge rate were discovered for a given chamber pressure which allows for complex switching between explosive and effusive activity.

4.2.2   How is gas transported to the conduit walls?

The above models have demonstrated the great importance of gas loss on the flow dynamics and style of an eruption. The mechanism by which gas is transported from the interior of the rising magma to the conduit walls, however, remains unclear. In the models of Jaupart and Allègre (1991) and Woods and Koyaguchi (1994), the details of the process were not considered. Melnik and Sparks (1999) considered only vertical gas flux by permeable flow through the magma itself.

There are two possible ways in which gas can be transported from the interior of a rising column of melt to the conduit walls. Gas can either be transported as bubbles which migrate laterally, or by permeable flow through interconnected bubbles. The diffusivity D of water in magma is far too low to allow significant lateral diffusive gas transport on the timescale of an eruption; taking $D = 10^{-11}$ $\mathrm{m^2\,s^{-1}}$ with a conduit radius r of 10 m, a characteristic timescale for diffusion is 10^{13} s $(=r^2/D)$.

Migration of gas bubbles

It is very unlikely that small gas bubbles could move relative to a high-viscosity (dacitic or rhyolitic) melt. To illustrate this, let us calculate the Stokes velocity v of a bubble of radius r rising through a fluid of dynamic viscosity η:

$$v = \frac{1}{3}\frac{r^2 g(\rho_l - \rho_g)}{\eta} \tag{4.7}$$

where g is the acceleration due to gravity and ρ_l and ρ_g are the liquid and gas densities respectively. Taking $r = 1$ mm, g=9.81 $\mathrm{m\,s^{-2}}$, $\rho_l = 2300$ $\mathrm{kg\,m^{-3}}$, $\rho_g = 0$ and $\eta = 10^4$ $\mathrm{Pa\,s}$, we obtain $v = 7.5 \times 10^{-7}$ $\mathrm{m\,s^{-1}}$. This value must be considered an upper bound as I have deliberately chosen low values of ρ_g and η and a high value of r in order to maximize v. Even this unrealistically high Stokes velocity is extremely slow compared with the ascent velocity of magma; for example, Rutherford and Hill (1993) estimated magma ascent velocities of 15–50 metres per hour $(4.2 - 14 \times 10^{-3}$ $\mathrm{m\,s^{-1}})$ for the dome growth phases of the 1980–1986 eruption of Mount St. Helens. Motion of gas bubbles relative to the melt phase must therefore be ruled out.

A recent study by Wilson (1998) showed that gas could be transported laterally *with* the melt, carried along by the motion of fluid perpendicular to the main (upward) flow direction. The mechanism for generating this lateral flow is as follows. Wilson considered the upward motion of bubbly, compressible magma in a parallel-sided conduit or dyke. The key behind the analysis is that the viscosity of the melt is very sensitive to its water content (e.g. Hess and Dingwell 1996) and the water content of the melt is dependent on the pressure (Henry's law, $c = \alpha\sqrt{P}$). This leads to the result that the melt viscosity is essentially a function of pressure— a high pressure gives a high water concentration in the melt and a low melt viscosity. As the melt rises through the conduit and degasses, the liquid viscosity increases and a horizontal pressure gradient is created such that the pressure in the centre of the conduit is greater than that at the walls, a result which

arises from a solution of the relevant equations of motion. Hence the melt viscosity at the centre of the conduit is less than that at the walls. Similar vertical stratifications of viscosity were shown to be unstable by Renardy (1987). This instability leads to a large-scale overturning and mixing of the magma, transporting bubbles from the centre of the conduit to the walls.

Gas transport by permeable flow

The second mechanism by which gas can be transported from the interior of the magma to the conduit walls is by permeable flow through interconnected bubbles within the magma. This was first proposed by Eichelberger et al. (1986), based on data obtained from drilling into Obsidian Dome, eastern California. At this locality, both tephra from an explosive eruption and rhyolitic lava were recovered; no petrological difference between these deposits was reported. The dome consists of both vesicle-poor and pumiceous material and the porosity of the lava increases towards the vent. Eichelberger et al. (1986) interpreted this to indicate that the lava had erupted as a highly-porous foam; gas then escaped from this permeable foam as it flowed away from the vent, reducing its porosity and causing it to collapse into vesicle-poor obsidian. Westrich and Eichelberger (1994) showed experimentally that pumices could collapse under pressure to form obsidian with no relict bubble textures. Eichelberger et al. (1986) measured the permeability of six samples from Obsidian Dome and remarked that the permeability of the samples became significant for porosities greater than 60%. Westrich and Eichelberger (1994) reported that their artificially-produced rhyolite foams also became permeable at 60% porosity. Whitham and Sparks (1986) observed that immersed pumices can absorb water and sink, requiring that their vesicles are interconnected.

The permeable foam model of Eichelberger et al. (1986) initially met with opposition from some workers (e.g. Friedman 1989; Fink 1992) who preferred an explanation for effusive

volcanism based on a low initial water content. However, current evidence (discussed above) is now overwhelmingly in favour of the hypothesis that effusive silicic volcanism arises, in many cases at least, from a high initial water content and must therefore be due to open-system degassing. Many studies (Eichelberger et al. 1986; Klug and Cashman 1996; Saar and Manga 1999) have shown that volcanic rocks are permeable to gas. For gas loss by permeable flow to occur, the conduit must become overpressured with respect to its surroundings; models of conduit flow (e.g. Jaupart and Allègre 1991) and field observations of ground deformation (e.g. Voight et al. 1998) reveal that this overpressure does indeed occur. Field observations (Stasiuk et al. 1996) and drilling projects (Eichelberger et al. 1996) reveal that the fractured nature of the conduit walls allows gas to be released into the volcanic edifice.

We can be confident, therefore, that gas can be lost by permeable flow from magma as it rises through the conduit. It is very important to calculate the rate at which this can occur, as we have seen that gas loss to the conduit walls can have a profound effect on large-scale flow dynamics and the style of eruption (effusive versus explosive). The rate of gas flow (at low Reynolds number) through a permeable medium is given by Darcy's law:

$$G = -\frac{k\rho A \Delta P}{\mu l} \tag{4.8}$$

where G is the mass flux of gas, ΔP is the driving pressure differential, l is the downstream length of the domain, A is the cross-sectional area of the domain, μ is the dynamic viscosity of the permeating gas and k is the permeability of the medium. For a volcanic system, l, A and μ can all be estimated with reasonable accuracy, and ΔP can be calculated from a solution of the equations of motion (e.g. Wilson 1998). At present, the greatest unknown in equation 4.8 is the permeability k.

Accurate estimation of k is crucial to the calculation of the rate of gas loss from a volcanic system. It is to be expected that k will depend on the porosity of the rock ϕ; the greater

the volume fraction of bubbles, the more likely they are to become interconnected to form a permeable network. In this chapter, I shall develop and apply a new model to elucidate the relationship between k and ϕ and examine the factors which control this relationship. The bulk of the material in this chapter is reproduced in two papers. In Blower (2001) the formulation of the model is described in detail. The results and implications of the model are discussed in a manuscript (J.D. Blower, *Factors controlling permeability–porosity relationships in volcanic rocks*) which has been submitted for publication in the Bulletin of Volcanology.

I shall now discuss previous studies concerning the evaluation of magma permeability.

4.2.3 Measurements of permeability

Currently, experimental data concerning permeability–porosity relationships in volcanic rocks are scarce, particularly at low porosities. The only published datasets known to the author are those of Eichelberger et al. (1986), Klug and Cashman (1996) and Saar and Manga (1999). The data of Klug and Cashman show very different permeability–porosity relationships to those of Eichelberger et al. (figure 4.1). The difference is most clearly marked at low porosities. The statement of Eichelberger et al. (1986) that magma permeability only becomes significant for $\phi > 60\%$ is not supported by the data of Klug and Cashman. If these measurements are reliable then it is clear that k depends on more than porosity alone. Dingwell (1998) suggested that the difference between the two datasets might be due to samples suffering mechanical damage on cooling. In this chapter an alternative hypothesis will be developed.

In Saar and Manga (1999) the importance of the control of the rock microstructure on the permeability is highlighted (figure 4.2). A $k - \phi$ trend of the form observed in the data of Klug and Cashman (1996) was only reproduced for samples of scoria with sub-spherical bubbles. Samples which had undergone significant strain and distortion of their vesicles
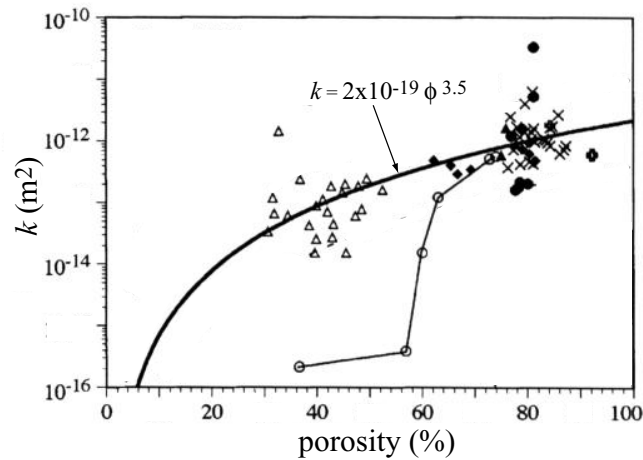
Figure 4.1: Laboratory measurements of permeability-porosity relationships by Eichelberger (1986, open circles and thin trendline) and Klug and Cashman (1996, all other symbols, thick trendline and best fit equation), adapted from Klug and Cashman (1996). Note the very different trends in the two datasets and the large degree of scatter in the data. It should be noted that to make a proper comparison, the permeability values should be normalized to the square of the bubble radius in each sample.

showed very different $k - \phi$ relationships.

Permeability data for granular rocks such as sandstones are much more plentiful (e.g. Bourbie and Zinszner 1985) than for volcanic rocks; the accurate measurement of the permeability of reservoir rocks (commonly sandstones or fractured limestones) is very important for the extraction of underground oil and water. Many theoretical models have been developed to interpret these data (e.g. Bosl et al. 1998; Manwart et al. 2000). These models cannot, however, be directly applied to volcanic rocks as they are based on a very different microstructure. In these models permeability develops through the connection of interstices between grains (Feng et al. 1987; Manwart et al. 2000) or through the connection of fractures (Cravero and Fidelibus 1999). It is usually imagined (Saar and Manga 1999) that permeability in volcanic rocks is due to the interconnection of bubbles (figure 4.3).

Percolation theory (Sahimi 1994) is a powerful tool for investigating fluid permeability in idealized cases. Often, this theory is concerned with regular arrangements of objects
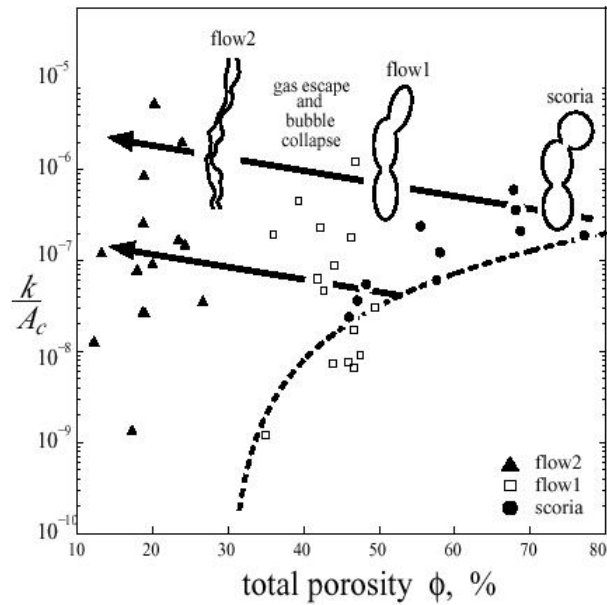
Figure 4.2: Permeability–porosity relationships in vesicular basalts from Saar and Manga (1999). The permeability k has been normalized against the median cross-sectional bubble area A_c. Measurements of permeability are shown for three different rock types; scoria with sub-spherical bubbles and samples whose bubbles have been elongated by flow to different extents. The arrows indicate the evolution of permeability as magma becomes sheared and its bubbles become deformed.
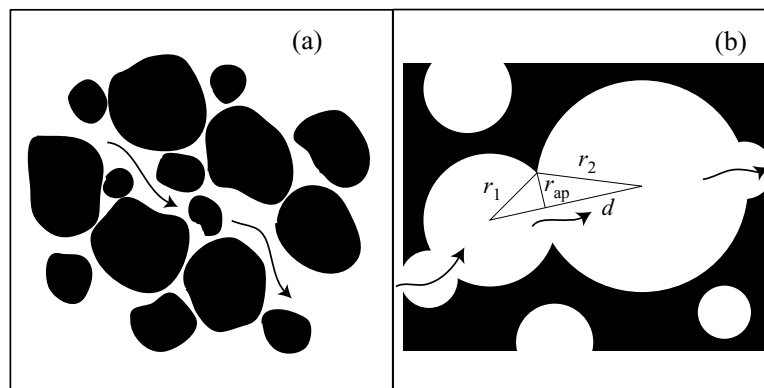
Figure 4.3: (a) Permeability of granular rocks develops through connection of intergranular pore spaces. (b) In volcanic rocks, permeability arises through connections between bubbles. The width of the aperture (r_{ap}) controls the resistance to flow of the bubble–bubble bond. r_{ap} may be calculated given the radius of both bubbles r_1 and r_2 and the bubble separation d (equation 4.10).

(e.g. bubbles or grains) on a lattice. The closest analogue of a volcanic rock within percolation theory is the fully-penetrating sphere (FPS) model (Lee 1990). In the FPS model, permeability develops through interconnection of randomly-placed spherical void spaces which are not confined to a regular lattice. However, the 'bubbles' are spherical and are imagined to be all of the same radius; in volcanic rocks, bubbles are often ellipsoidal or cylindrical and the bubble size distribution is rarely monodisperse.

The above treatments, both theoretical and experimental, give power-law relationships between permeability k and porosity ϕ (Klug and Cashman 1996; Saar and Manga 1999; Sahimi 1994):

$$k = a\phi^b \quad \text{or} \quad k = a(\phi - \phi_{\text{cr}})^b \quad (\phi \geq \phi_{\text{cr}}) \tag{4.9}$$

where a and b are constants and ϕ_{cr} is a critical porosity below which permeability is zero (the *percolation threshold*, section 4.4.1). Another consistent result is that values of permeability span five or six orders of magnitude over the porosity range of volcanic rocks, further emphasizing the importance of understanding $k - \phi$ relationships. Eichelberger et al. (1986) implied that $\phi_{\text{cr}} \sim 60\%$ whereas Saar and Manga (1999) inferred that the critical porosity was much lower, lying at around 30% porosity. The critical porosity defines the onset of permeability and is therefore a very important parameter to constrain; if permeability develops early in the vesiculation process then the potential for gas loss is much greater than if the magma remains impermeable for most of its evolution.

4.3   Development of the model

The simulation of the three-dimensional flow of a liquid or gas in a vesicular material such as volcanic pumice or scoria is, in the general case, an enormously complicated task. In such media, the permeability is developed by interconnection of bubbles, which may be spherical, ellipsoidal, tubular or very much more complicated in form. The path which a
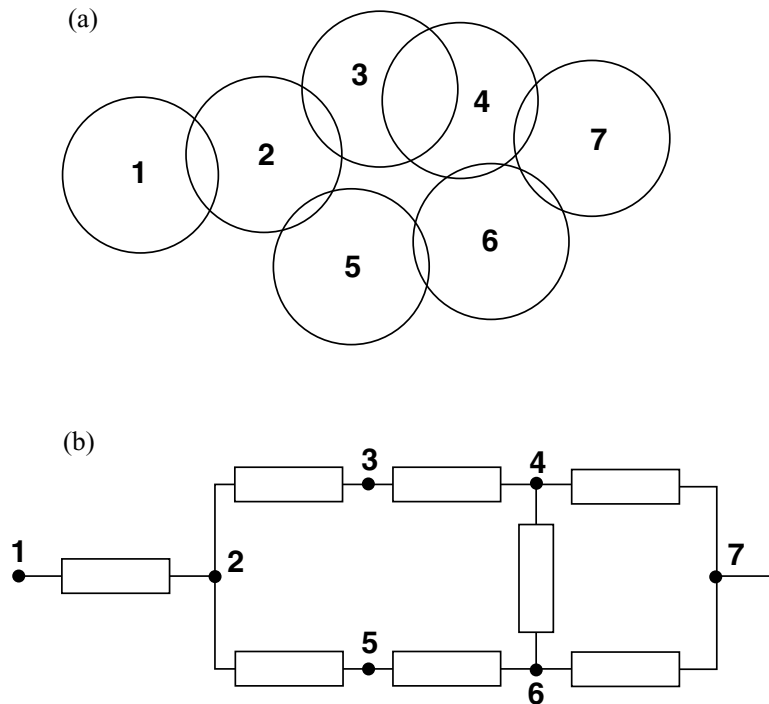
Figure 4.4: (a) A general network of bubbles. The permeability of the network between bubbles 1 and 7 is calculated by drawing an analogy with a network of resistors in an electrical circuit (b).

fluid might take through the material will be very complex and tortuous. In this model, the problem of solving for the fluid flow through a complex pathway in a volcanic rock is simplified by treating the pathway as a network of discrete resistances to fluid flow (figure 4.4). The total resistance to flow is calculated using circuit theory, adapted from Fidler (1988).

In this model, it is assumed that permeability develops through the interconnection of bubbles, and that permeability is limited by the circular apertures connecting pairs of bubbles (figure 4.3b). Each connection between two bubbles is termed a 'bond'.

4.3.1 Bond conductance

The fluid conductance of each bond is controlled by the radius of the aperture r_{ap} connecting the bubble–bubble pair (figure 4.3b). In general, Pythagoras' theorem gives:

$$d = \sqrt{r_1^2 - r_{\mathrm{ap}}^2} + \sqrt{r_2^2 - r_{\mathrm{ap}}^2} \tag{4.10}$$

In the case $r_1 = r_2 = r$, we have $r_{\mathrm{ap}} = \sqrt{r^2 - d^2/4}$. If $r_1 \neq r_2$ there is no analytical solution but r_{ap} may be found numerically.

Feng et al. (1987) state that the permeability of this hole is approximately the same as that of a circular tube of equal radius and of length equal to the diameter of the hole ($2r_{ap}$). Assuming Poiseuille flow in this tube:

$$G = -\frac{\pi \rho \Delta P r^4}{8 \mu l} \tag{4.11}$$

(G is the mass flux of permeating fluid, ρ is its density, μ is its viscosity, ΔP is the driving pressure, r is the radius of the tube and l is its length) we may define the conductance of the bond as:

$$K = \frac{G}{\Delta P} = \frac{\pi \rho}{16 \mu} r_{\mathrm{ap}}^3 \tag{4.12}$$

(cf. conductance = current / voltage for electricity).

A more rigorous fluid dynamical treatment may be required, but is not necessarily justified given that, in the real case, the fluid flow is far from simple and so the boundary conditions for flow entering such an aperture will not be known.

4.3.2 Methodology

To calculate the total permeability of a network of bubbles, a computer program was written. The program is divided into 3 routines: (1) generation of the bubble distribution and calculation of porosity; (2) investigation of the connections between the bubbles; and (3) calculation of the total permeability of the virtual foam.

Bubble generation and calculation of porosity

The user specifies the size of the domain in which the bubbles are to be placed. The domain is cuboidal, with three dimensions x, y and z, measured in pixels: usually $x = y = z = X$ pixels.

The number of bubbles m and their radii are then provided (the bubble size distribution or BSD). To ensure a statistically valid population distribution the radius of the bubbles is always significantly smaller (by a factor of 10) than the size (X) of the domain. The bubble centres are placed at random over the X^3 nucleation sites. The porosity ϕ is calculated by counting the fraction of the X^3 volume elements (voxels) which fall within a bubble. An image of a slice through the foam may be generated— see figure 4.5 for an example.

Bubble connections

This routine tests each bubble pair in the distribution to see if they intersect (i.e. if the distance between their centres is less than the sum of their radii, $d < r_1 + r_2$). Each bond is ascribed a conductance according to equation (4.12) and the bond conductance information is stored in a square matrix of rank m.

Bubbles are then separated into clusters according to their connections: two bubbles are
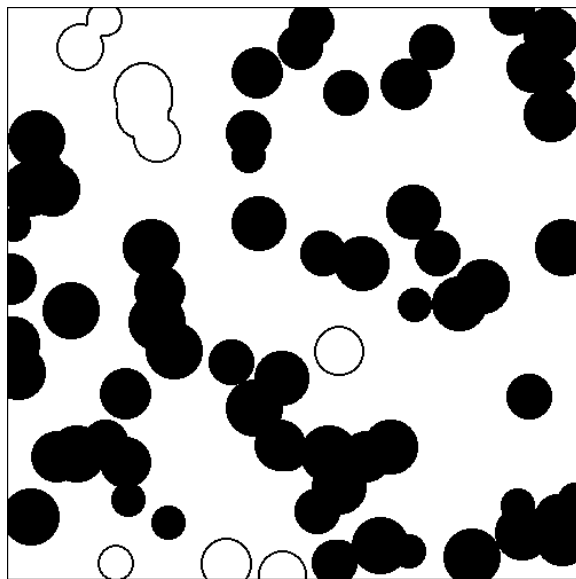
Figure 4.5: A picture of a slice through the virtual foam. Bubbles in black form part of a percolating cluster connecting all six sides of the domain. Bubbles in outline are not part of this cluster. Note that this is a section of a three-dimensional domain and some apparently separate bubbles are connected in the third dimension. The bubbles are all of the same radius and the porosity of the foam ϕ is 38%. (Domain size $X = 1000 \times 1000 \times 1000$ pixel units, using 1000 bubbles of radius 50 pixels.)
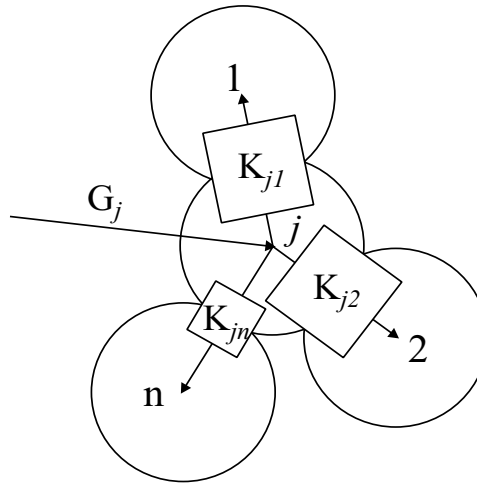
Figure 4.6: A general node in the network of bubbles. The squares represent cross-sections of the tubes used to calculate the conductance of the bond (see equation (4.12)).

deemed to be in the same cluster if they are connected either directly or indirectly (via other bubbles).

Total permeability calculation

This routine is performed if it is found that a cluster of bubbles touches two opposing faces of the domain. There is then a pathway for fluid flow across the domain. The total permeability of the cluster is calculated by nodal analysis, adapted from Fidler (1988). Only bubbles which are part of the percolating cluster are included in this part of the analysis and each of these bubbles is a node in the network.

There are two more nodes (node 1 and node n)— one representing each opposing, connected face of the domain. Therefore, if the percolating cluster contains N bubbles, the number of nodes in the analysis is $n = N + 2$. If a bubble touches the edge of the domain then the radius of the circle described by the intersection of the bubble and the (flat) surface of the domain is used to calculate the conductivity of the bond.

The mass fluid flux through the upstream face (node 1) is G_1 and the flux through the

downstream face (node n) is $-G_1$. The algebraic sum of the fluxes entering and leaving each bubble is zero. By inspection of Fig. 4.6, we have, at a general node j:

$$
\begin{aligned}
G_j &= (P_j - P_1)K_{j1} + (P_j - P_2)K_{j2} + \ldots + (P_j - P_n)K_{jn} \\
&= \frac{\pi\rho}{16\mu}\left\{ P_j \sum_{\substack{i=1 \\ i \neq j}}^{n} r_{ji}^3 + \sum_{\substack{i=1 \\ i \neq j}}^{n} P_i(-r_{ji}^3) \right\}
\end{aligned}
\tag{4.13}
$$

with:

$$
G_j = \begin{cases} 0 & : \quad 2 \leq j \leq n-1 \\ G_1 & : \quad j = 1 \\ -G_1 & : \quad j = n \end{cases}
$$

where r_{ji} is the radius of the aperture connecting bubbles i and j. If there is no bond between these nodes, $r_{ji} = 0$.

Letting

$$
y_{jj} = \sum_{\substack{i=1 \\ i \neq j}}^{n} r_{ji}^3
$$

and

$$
y_{ji} = -r_{ji}^3 \quad (i \neq j)
$$

Equation (4.13) becomes:

$$
G_j = \frac{\pi\rho}{16\mu} \sum_{i=1}^{n} y_{ji} P_i
\tag{4.15}
$$

Writing equation (4.15) for each node in the percolating cluster, we obtain:

$$\begin{bmatrix} G_1 \\ 0 \\ \vdots \\ -G_1 \end{bmatrix} = \frac{\pi\rho}{16\mu} \begin{bmatrix} y_{11} & y_{12} & \dots & y_{1n} \\ y_{21} & y_{22} & \dots & y_{2n} \\ \vdots & \vdots & & \vdots \\ y_{n1} & y_{n2} & \dots & y_{nn} \end{bmatrix} \begin{bmatrix} P_1 \\ P_2 \\ \vdots \\ P_n \end{bmatrix} \qquad (4.16)$$

The set of n equations represented by this matrix equation cannot be solved as they are dependent. However, since node n represents the downstream face of the domain, we may conveniently define the pressure here to be zero ($P_n = 0$, analogous to ground in an electrical circuit). We may now remove the nth row and column of the above square matrix to obtain $n - 1$ independent equations. If we define:

$$\mathbf{Y} = \begin{bmatrix} y_{11} & y_{12} & \dots & y_{1,n-1} \\ y_{21} & y_{22} & \dots & y_{2,n-1} \\ \vdots & \vdots & & \vdots \\ y_{n-1,1} & y_{n-1,2} & \dots & y_{n-1,n-1} \end{bmatrix} \qquad (4.17)$$

and let $\mathbf{Z}$ be the inverse of $\mathbf{Y}$ then we have:

$$\begin{aligned} \begin{bmatrix} P_1 \\ P_2 \\ \vdots \\ P_{n-1} \end{bmatrix} &= \frac{16\mu}{\pi\rho} \begin{bmatrix} Z_{11} & Z_{12} & \dots & Z_{1,n-1} \\ Z_{21} & Z_{22} & \dots & Z_{2,n-1} \\ \vdots & \vdots & & \vdots \\ Z_{n-1,1} & Z_{n-1,2} & \dots & Z_{n-1,n-1} \end{bmatrix} \begin{bmatrix} G_1 \\ 0 \\ \vdots \\ 0 \end{bmatrix} \\ &= \frac{16\mu}{\pi\rho} \begin{bmatrix} Z_{11} \\ Z_{21} \\ \vdots \\ Z_{n-1,1} \end{bmatrix} G_1 \\ \Rightarrow P_j &= \frac{16\mu}{\pi\rho} Z_{j1} G_1 \qquad (4.18) \end{aligned}$$

The matrix inversion is performed by standard Gauss-Jordan elimination with full pivoting (adapted from Press et al. 1992). (Note that $\mathbf{Y}$ is sparse and symmetric and so this algorithm is inefficient. However, the routine is extremely reliable and well-tested and computation speed is not an important issue.) The total conductance of the network

between the two opposing sides of the domain (nodes 1 and n) is then:

$$K_{1n} = \frac{G_1}{P_1} = \frac{\pi\rho}{16\mu} \frac{1}{Z_{11}} \tag{4.19}$$

Applying Darcy's law (equation 4.8) we obtain the total permeability of the domain:

$$k_{\text{tot}} = K_{1n} \frac{\mu l}{\rho A} = \frac{\pi l}{16A} \frac{1}{Z_{11}} \tag{4.20}$$

A is the cross-sectional area of the domain (perpendicular to the flow direction) and l is the length of the domain (parallel to the flow direction). It is usual to specify a cubic domain in the model, giving $l = X$ and $A = X^2$ and:

$$k_{\text{tot}} = \frac{\pi}{16X} \frac{1}{Z_{11}} \tag{4.21}$$

The permeability in each of the three directions $\hat{\mathbf{x}}$, $\hat{\mathbf{y}}$ and $\hat{\mathbf{z}}$ is calculated by changing which pair of opposing faces we choose to be nodes 1 and n. If the bubbles are spherical the problem is isotropic so the three permeabilities k_x, k_y and k_z are found to be equal over a number of analyses. If there exists more than one cluster which connects the same two opposing sides of the domain then the conductance of each is calculated and summed (cf. electrical conductors in parallel) to obtain the total conductance in this direction.

The model allows for variation of the bubble size, the form of the bubble size distribution, the bubble shape and the ease of bubble coalescence. The effects of these factors are now discussed.
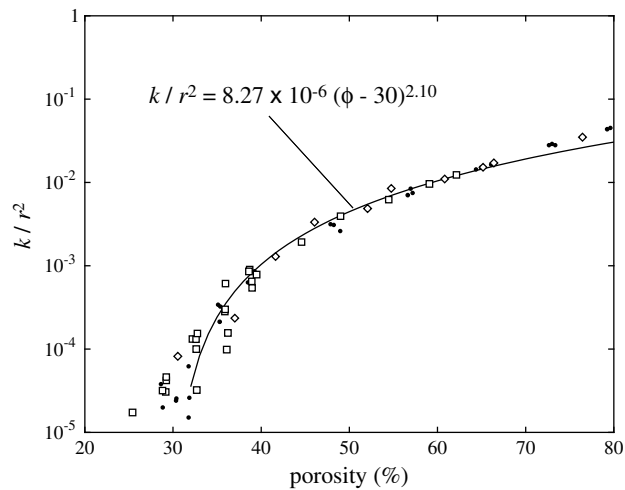
Figure 4.7: The effect of bubble size on the normalized permeability. The results of three experiments are shown here, all using a domain size of $X = 1000$. Black dots: $m = 1000$ bubbles, $55 \leq r \leq 75$. Open squares: $r = 50$, $400 \leq m \leq 2000$. Open diamonds: $r = 100$, $50 \leq m \leq 1000$. The line represents the best fit of equation 4.9 (second equation) over the porosity range $35\% \leq \phi \leq 80\%$.

4.4 Results

4.4.1 Percolation threshold

Percolation theory (Lee 1990; Sahimi 1994; Grimmett 1999) predicts that percolating clusters of bubbles should only exist above a certain critical porosity, ϕ_{cr}. Figure 4.7 shows the results of a large number of numerical experiments and reveals that the percolation threshold lies close to 30% porosity, a result also found by Saar and Manga (1999). The data of Klug and Cashman (1996) contain no measurements of permeability below 30% porosity (figure 4.1). The value of the percolation threshold is slightly affected by the bubble size distribution (section 4.4.3) and bubble shape (section 4.4.4). The threshold may be greatly increased by imposing a barrier to bubble coalescence (section 4.4.5).

4.4.2 Effect of bubble size

The normalized permeability $\hat{k}$ is independent of the bubble size (figure 4.7). This is only violated if the bubble radius r (for a monodisperse distribution) is greater than $0.1X$, where X is the domain side length. The relationship between $\hat{k}$ and ϕ is well-approximated by the following expression:

$$\hat{k} = 8.27 \times 10^{-6}(\phi - 30)^{2.10} \quad (30\% \leq \phi \leq 80\%) \tag{4.22}$$

This represents the best fit of equation 4.9 to the numerical results in figure 4.7 over the porosity range $35\% \leq \phi \leq 80\%$ with $\phi_{cr} = 30\%$. Porosities less than 35% were not included in the best fit calculation due to the large amount of scatter near the percolation threshold— near ϕ_{cr} small variations in the position of the bubbles cause large variations in permeability.

4.4.3 Effect of the bubble size distribution

Any bubble size distribution may be used in the model. Here monodisperse, gaussian, exponential and power law distributions are investigated. The results are summarized in figure 4.8. Polydisperse BSDs lead to a permeability that is approximately one order of magnitude greater than that of a monodisperse distribution at the same porosity. There is very little difference between the $\hat{k} - \phi$ relationships for the different forms of polydisperse BSD. The percolation threshold is reduced slightly to a porosity of $\sim 27\%$.

4.4.4 Effect of the bubble shape

It is common to observe non-spherical bubbles in volcanic rocks. In many cases, vesicles are found to be elongate in a certain direction (figure 4.9). The model demonstrates the
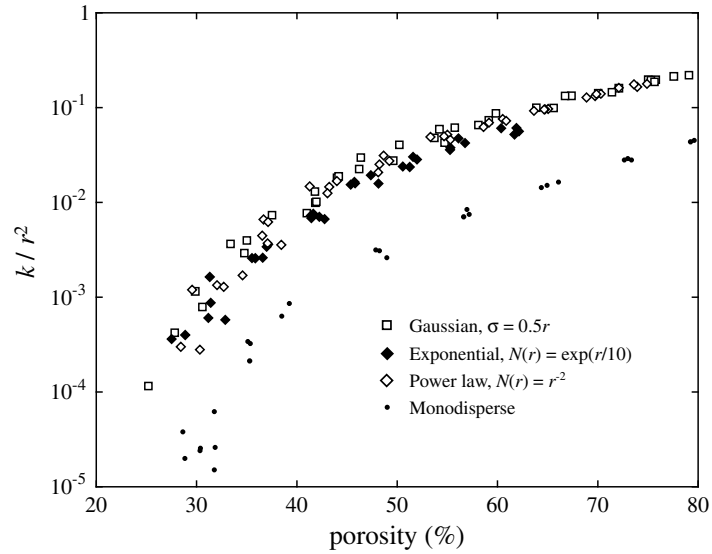
Figure 4.8: The effect of the bubble size distribution on permeability. Polydisperse distributions give a permeability approximately one order of magnitude greater than monodisperse. The differences between $k - \phi$ trends of different forms of polydisperse BSD are relatively small.

effect of this anisotropy on permeability, assuming that bubbles take the form of prolate rotational ellipsoids with aspect ratio α (figure 4.10). When two bubbles overlap, the aperture connecting them is an ellipse. If the long and short axes of this ellipse are a and b respectively, then the equivalent circular radius of the aperture is $r_{\mathrm{ap}} = \sqrt{ab}$ and the calculation of permeability proceeds as above.

As expected, permeability is enhanced in the direction of elongation which is taken to be the z-direction (figure 4.11). The greater the aspect ratio of the ellipsoids, the greater the anisotropy of the permeability. The percolation threshold in this direction is reduced. In the x and y directions, the permeability is the same as the permeability of spheres at the same porosity; it is independent of the aspect ratio of the ellipsoids. Therefore, if the magma in a conduit contains bubbles which are elongate parallel to the axis of the conduit then the rate of gas loss vertically through the magma to the vent is expected to be more rapid than the rate of gas loss horizontally to the conduit walls.
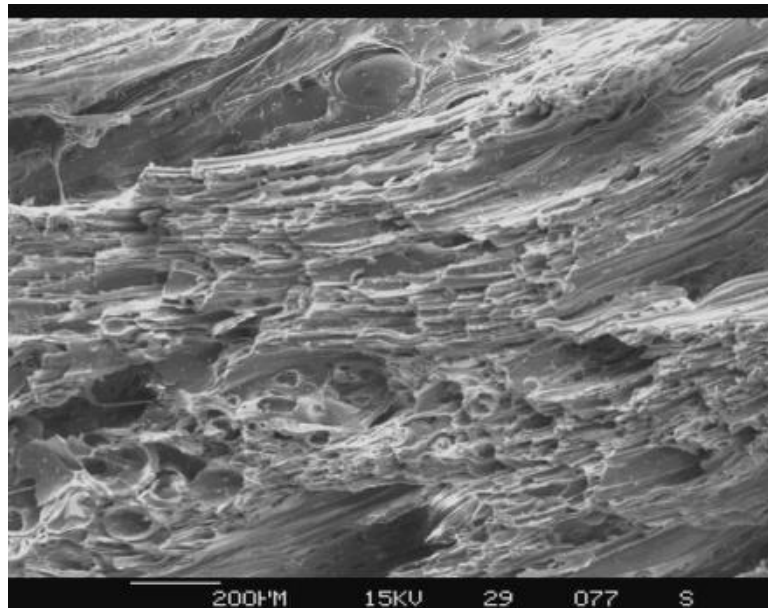
Figure 4.9: SEM image of tube pumice from the Minoan Phase One Plinian eruption, Santorini, Greece.
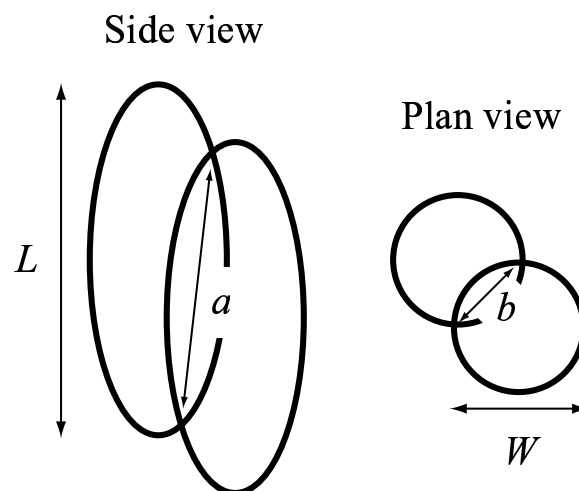
Figure 4.10: Two intersecting ellipsoidal bubbles of aspect ratio $\alpha = L/W$. The equivalent circular radius of the aperture connecting the bubbles is $\sqrt{ab}$.
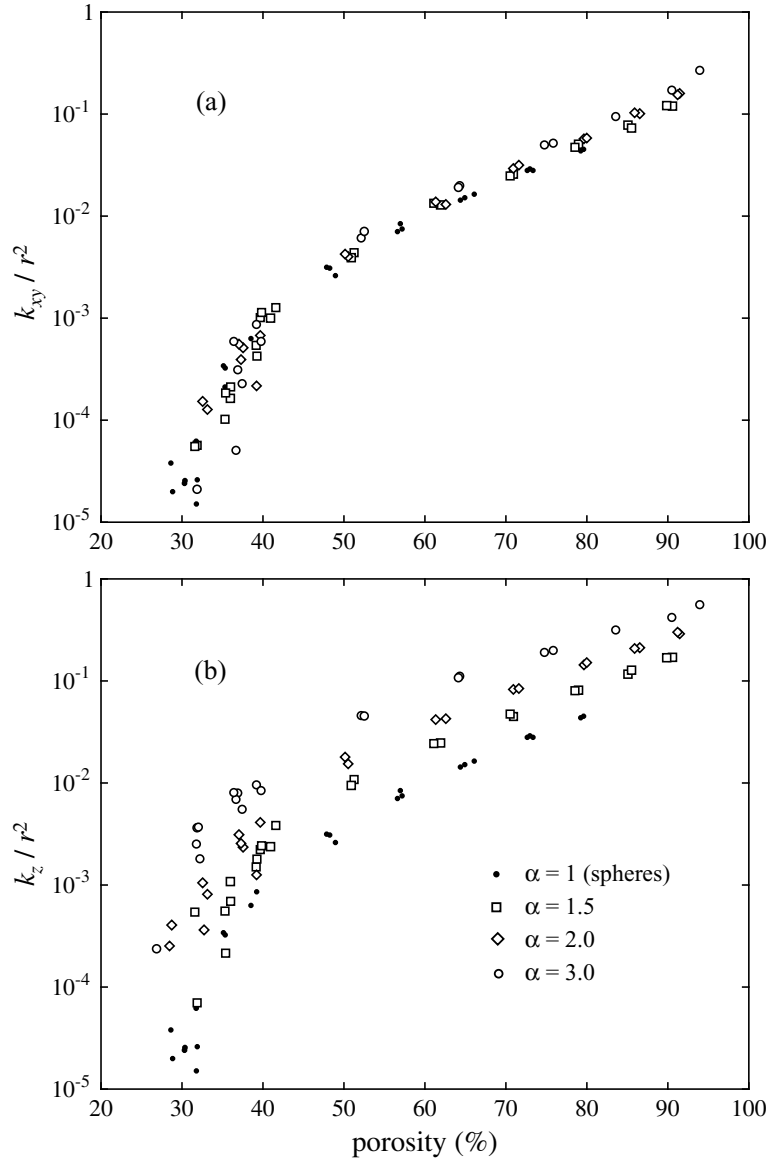
Figure 4.11: $\hat{k} - \phi$ relationships for a monodisperse array of 1000 ellipsoidal bubbles of aspect ratio 1 (spheres), 1.5, 2 and 3. (a) Permeability perpendicular to the elongation direction (the x and y directions) is independent of the aspect ratio. (b) Permeability in the z (elongation) direction increases as the aspect ratio of the bubbles increases. The percolation threshold is reduced.
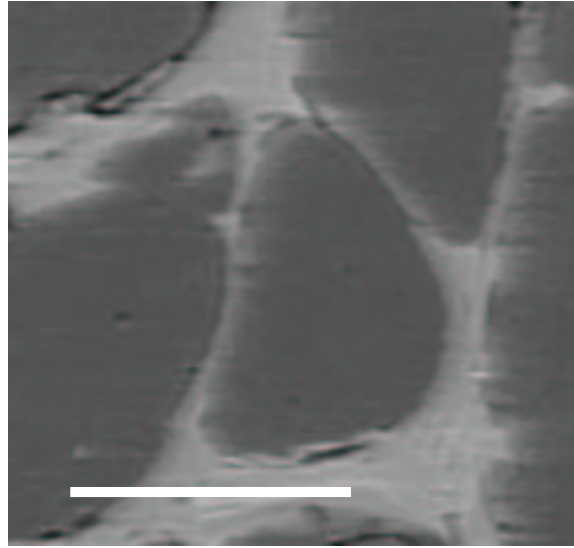
Figure 4.12: Melt films between impinging neighbouring bubbles in a sample of pumice from the Minoan Phase One Plinian eruption of Santorini, Greece. Scale bar is 50 μm. This illustrates that there exists a barrier to bubble coalescence.

4.4.5 Effect of a barrier to coalescence

So far it has been assumed that a connected pathway between bubbles exists if they overlap (i.e. if $d < r_1 + r_2$). There is abundant textural evidence to suggest that the reality is much more complicated than this suggests. The persistence of melt films between impinging bubbles (figure 4.12) attests to the difficulty of bubble coalescence in magmas. The retraction of the melt film, and hence the process of bubble coalescence, is slowest in melts of high viscosity (Proussevitch et al., 1993b).

A full treatment of the dynamics of bubble coalescence is beyond the scope of this model. We may, however, capture some of the features of the process by introducing an artificial barrier between bubbles. We may imagine that, unless a pair of bubbles overlaps by a certain amount, a film of melt remains between the bubbles and gas cannot flow between them. The condition for an open pathway to exist between two bubbles of radius r is then:

$$d < r(2 - \epsilon) \tag{4.23}$$

where ϵ is the 'barrier factor' ($0 \leq \epsilon \leq 1$) and d is the distance between the bubble centres. The higher the value of ϵ, the harder it is for an open pathway to exist between two bubbles. All other factors being equal, ϵ may be thought of as a measure of the melt viscosity. Alternatively, ϵ may be considered to be an indication of the timescale of bubble coalescence relative to the timescale of cooling and solidification; if the magma stiffens rapidly compared with the time required for film thinning to occur, then coalescence will be difficult and ϵ will be high. Proussevitch et al. (1993b) investigated the process of film thinning and rupture and concluded that a melt film between bubbles will rupture when it reaches a certain critical thickness. This thickness depends on the melt viscosity, interfacial surface tension, the timescale of film thinning and the difference in internal pressures between two adjacent bubbles. Based on simple calculations and SEM observations, Klug and Cashman (1996) proposed that a typical value for the critical film thickness in pumice is ~ 1 μm. Navon and Lyakhovsky (1998) suggest that the critical film thickness may be as small as 0.2 μm.

The effect of this barrier is shown in figure 4.13. As ϵ increases, the percolation threshold is shifted to higher porosities and the trend of the $\hat{k} - \phi$ relationship steepens. Comparing figure 4.13 with figure 4.1, we may formulate a hypothesis to explain why the data of Klug and Cashman (1996) and Eichelberger et al. (1986) give such different $\hat{k} - \phi$ trends. If bubble coalescence was more difficult in the samples of Eichelberger et al. than in those of Klug and Cashman, the difference in the trends may be explained. Indeed, the samples of Eichelberger et al. were of very high viscosity, coming from an obsidian dome. This provides an alternative to the suggestion of Dingwell (1998), who proposed that the difference may be due to mechanical damage on cooling. The ease or otherwise of bubble coalescence is a major factor in controlling the development of permeability in magma.
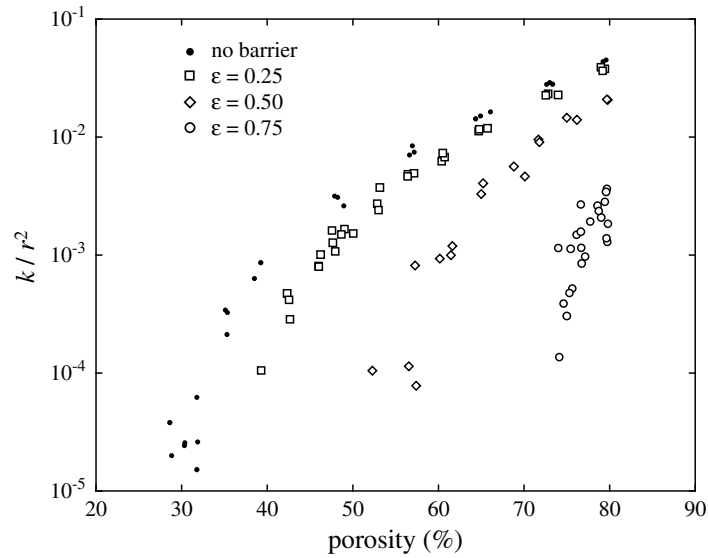
Figure 4.13: The effect of a barrier to bubble coalescence on the relationship between permeability and porosity. As the barrier factor ϵ (equation 4.23) increases, the permeability at a given porosity is much reduced, and the percolation threshold is shifted to higher porosities. This barrier is one of the major controls on $\hat{k} - \phi$ relationships.

4.4.6   Effect of the spatial arrangement of bubbles

So far it has been assumed that the bubble centres are randomly placed and that the radius of each bubble is independent of its position. A more realistic approach is to set the size of each bubble to be dependent on its surroundings. An isolated bubble which is placed far from other bubbles will grow to a relatively large size as it has a large reservoir of volatile resources from which to grow. By contrast, a bubble which is close to a group of other bubbles cannot grow to be as large as it must compete with its neighbours for volatiles.

In the model, this effect is simulated in the following way. The bubble centres are placed at random positions in the domain as before. The *Voronoi volume* of each bubble centre is calculated: this is the number of the X^3 points which are closer to this bubble centre than to any other bubble. Isolated bubbles have a relatively large Voronoi volume. The volume
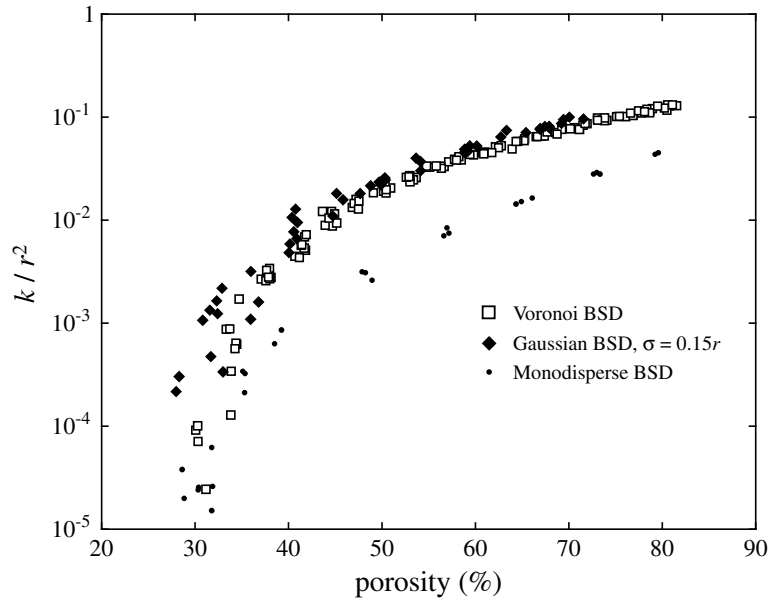
Figure 4.14: Permeability–porosity relationships for a Voronoi bubble population (section 4.4.6). The radius of each bubble is dependent on its surroundings; bubbles which must compete with their neighbours for volatile resources grow to a smaller size than those which are relatively isolated.

of each bubble is set to a specified fraction f of the Voronoi volume V (f is the same for all bubbles), and the radius is calculated ($= (3Vf/4\pi)^{1/3}$) assuming the bubbles are spherical. We shall term the resulting distribution a 'Voronoi' distribution. In this way, unimodal BSDs are generated, which are very well approximated by a Gaussian distribution with a standard deviation σ of ~ 0.15 times the mean radius. The model reveals (figure 4.14) that the effect of this spatial dependence of radius is minor; the $\hat{k} - \phi$ relationship for the Voronoi distribution is very close to that for a Gaussian distribution (with $\sigma = 0.15r$) in which the radius is completely independent of position.

This Voronoi bubble population is what we expect to develop if all bubbles nucleate at the same time. If, however, bubbles nucleate continuously during the growth process, we expect to see exponential or power-law BSDs (chapter 2). Furthermore, the position of each new bubble nucleus will be controlled by the position of the existing bubbles; the bubble centres are not randomly positioned. New bubbles are most likely to nucleate as far

from the existing bubbles as possible as this is where volatile resources are least depleted (Lyakhovsky et al. 1996). By this mechanism, it is theoretically possible to generate a material with nearly 100% porosity and zero permeability— an Apollonian packing of bubbles (Rouault 1999; chapter 2). Therefore, if nucleation proceeds continuously over a period of time it is very difficult to predict $\hat{k} - \phi$ relationships using this model. This is most likely to be a problem for highly non-equilibrium conditions which favour continuous nucleation (chapter 2).

4.4.7 Effect of crystals

The presence of crystals is not considered explicitly in the model. We may, however, qualitatively investigate how crystals might affect $\hat{k} - \phi$ relationships. If the volume fraction of crystals in the melt is β then we have the following relationship between the porosity of the melt ϕ_{melt} and the bulk porosity ϕ_{tot}:

$$\phi_{\text{melt}} = \frac{\phi_{\text{tot}}}{1 - \beta} \qquad (4.24)$$

The $\hat{k} - \phi$ relationships discussed in previous sections relate to *melt* porosity, however, it is more standard to measure and quote *bulk* porosities. The addition of crystals increases the melt porosity — and therefore the permeability — at a given bulk porosity, and will also have the effect of shifting the percolation threshold to lower bulk porosities. Of course, the real effect of crystals is more complex than is expressed in equation 4.24. The tortuosity of the percolating path through the melt region around the crystals will be increased, and this is likely to affect the permeability.

4.5   Conclusions

Using this model, we have gained valuable information about which factors are most important in controlling the permeability of vesiculating magma. It has been shown that, in the case of a single nucleation event and crystal-free melt:

- In order to compare permeability measurements from different samples, permeability must be normalized to the square of the mean bubble radius in the samples ($\hat{k} = k/r^2$).

- The equation $\hat{k} = 8.27 \times 10^{-6}(\phi - 30)^{2.10}$ describes well the relationship between $\hat{k}$ and ϕ from 30% to 80% porosity, for a monodisperse distribution of bubbles.

- The relationship between k/r^2 and ϕ is completely independent of bubble size as long as r is less than 0.1 times the domain size. Therefore, in experimental measurements of permeability, the sample size needs to be greater than ten times the largest bubble radius to provide a meaningful result.

- Below 30% porosity, permeability is zero. This may be reduced by the addition of crystals, or increased by imposing a barrier to coalescence. This means that, during a volcanic eruption, vesiculating magma may start to lose gas by permeable flow when the porosity reaches 30%. As vesicularity increases, permeability rises by several orders of magnitude.

- Permeability is extremely dependent on the ease of bubble coalescence. This might explain the discrepancy between two previously-obtained datasets (Eichelberger et al. 1986; Klug and Cashman 1996).

- The form of the bubble size distribution has relatively little effect on permeability. Polydisperse distributions give a permeability around one order of magnitude greater

than that of monodisperse distributions, and a slightly reduced percolation threshold of $\sim 27\%$.

- If bubbles are elongate in a certain direction, then permeability is increased in this direction. For example, if the bubbles are ellipsoids with aspect ratio 3, the permeability in the elongation direction is increased by an order of magnitude. Normal to this direction the permeability is unaffected.

The results are most readily applicable to low-viscosity magmas with spherical or sub-spherical bubbles. Saar and Manga (1999) investigated $\hat{k} - \phi$ relationships of basaltic rocks with a range of microtextures. They revealed the very important influence of microtexture on the permeability; only scoria samples with sub-spherical bubbles exhibited $\hat{k} - \phi$ relationships of the form discovered in the present study. Samples in which flow had caused the vesicles to become extremely distorted deviate strongly from the $\hat{k} - \phi$ trends of equations 4.9 and 4.22.

A better understanding of the dynamics of coalescence is required to be able to predict $\hat{k} - \phi$ relationships in magmas. Aside from this limitation, the model reveals that, if coalescence occurs readily, permeability may be predicted from the porosity and mean bubble size alone. These are both measurable by means of density measurements and image analysis, and so this model provides a practical tool for calculating the permeability of crystal-free melts at any stage in its evolution. It is not necessary to measure the exact form of the bubble size distribution.

4.5.1 Implications for modelling volcanic processes

This study has provided evidence that magma can become permeable relatively early in its evolution, at 30% porosity. If crystals are present, or bubbles become aligned by shear (as observed at the Mule Creek exposure, Stasiuk et al. 1996) then open pathways for gas

flow may develop at still lower porosities. Under conditions in which bubble coalescence is difficult (for example, a high magma viscosity) the percolation threshold may be increased; this is interpreted to be the reason why Eichelberger et al. (1986) did not measure a significant permeability until a porosity of 60%.

This provokes an important question: if magma becomes permeable so early in its evolution then how does it achieve the high porosities (60–80%) which we observe in pyroclasts? The answer lies in a consideration of the *rate* at which gas loss by permeable flow might occur. Even if an open pathway for gas is achieved at 30% porosity, the model shows that the permeability at this porosity is 3 orders of magnitude lower than that at 60% porosity, *for the same bubble size*. We expect that at 60% porosity the bubbles will be larger than at 30% porosity; this increases the permeability even further since k depends on r^2. I therefore propose that gas loss at low porosities is only important for very slow magma ascent rates.

In the models of Jaupart and Allègre (1991) and Woods and Koyaguchi (1994) the mechanism of gas transport from the magma to the conduit walls was not considered. Both these models assumed that gas loss was controlled (i.e. limited) by the permeability of the conduit walls. This implies that the permeability of the conduit walls is less than that of the magma. Woods and Koyaguchi (1994) calculated the conduit permeability using the expression $k_{\text{conduit}} = 10^{-12.5} \exp(-z/1000)$ m^2 where z is the depth in metres. Table 4.1 gives the values of permeability from this equation for depths from 0.5 to 6 km. For comparison, table 4.2 gives the magma permeability according to the present model (equation 4.22) for porosities from 35% to 80% and bubble radii from 0.001 to 1 mm. A comparison of the values of permeability in the two tables shows that for bubble radii greater than 0.1 mm the magma permeability is indeed greater than that of the conduit. For smaller bubbles, however, depending on the depth and porosity, the limiting (smaller) permeability may be either that of the magma or that of the conduit walls. A full solution of the eruption dynamics must therefore include an evaluation of both the magma perme-

depth z / km	k_{conduit} / m^2
0.5	1.9×10^{-13}
1	1.2×10^{-13}
2	4.3×10^{-14}
3	1.6×10^{-14}
4	5.8×10^{-15}
5	2.1×10^{-15}
6	7.8×10^{-16}

Table 4.1: Values of conduit permeability given by the expression $k_{\text{conduit}} = 10^{-12.5} \exp(-z/1000)$ m^2 (Woods and Koyaguchi 1994).

	Bubble radius / m			
	1×10^{-6}	1×10^{-5}	1×10^{-4}	1×10^{-3}
35%	2.4×10^{-16}	2.4×10^{-14}	2.4×10^{-12}	2.4×10^{-10}
40%	1.0×10^{-15}	1.0×10^{-13}	1.0×10^{-11}	1.0×10^{-9}
45%	2.4×10^{-15}	2.4×10^{-13}	2.4×10^{-11}	2.4×10^{-9}
50%	4.5×10^{-15}	4.5×10^{-13}	4.5×10^{-11}	4.5×10^{-9}
55%	7.1×10^{-15}	7.1×10^{-13}	7.1×10^{-11}	7.1×10^{-9}
60%	1.0×10^{-14}	1.0×10^{-12}	1.0×10^{-10}	1.0×10^{-8}
65%	1.4×10^{-14}	1.4×10^{-12}	1.4×10^{-10}	1.4×10^{-8}
70%	1.9×10^{-14}	1.9×10^{-12}	1.9×10^{-10}	1.9×10^{-8}
75%	2.5×10^{-14}	2.5×10^{-12}	2.5×10^{-10}	2.5×10^{-8}
80%	3.0×10^{-14}	3.0×10^{-12}	3.0×10^{-10}	3.0×10^{-8}

Table 4.2: Values of magma permeability (in m^2) given by equation 4.22 at various bubble radii (columns) and porosities (rows).

ability and the conduit wall permeability. The model described in this chapter provides a convenient method for calculating magma permeability and, if combined with a conduit flow model such as that of Jaupart and Allègre (1991) or Woods and Koyaguchi (1994), could provide a more accurate insight into volcanic eruption dynamics and the transition between effusive and explosive eruptions.

Chapter 5

Conclusions

The preceding three chapters are self-contained and may be read as entirely separate investigations. The purpose of this concluding chapter is to draw together the main findings of all these studies and to discuss how they have contributed to the major problems outlined in chapter 1.

Does degassing proceed in equilibrium with falling pressure?

In chapter 2 it was deduced that power law and exponential bubble size distributions, both commonly observed in volcanic rocks, were indicative of non-equilibrium degassing. For conditions of low initial bubble density, low volatile diffusivity, high melt viscosity or high decompression rates, a supersaturation of volatiles is expected to build in the melt pockets between bubbles. This supersaturation may lead to further nucleation events and hence the generation of a power law or exponential BSD. The formation of these new bubbles would reduce diffusion distances and promote degassing efficiency. The extent of the disequilibrium nature of degassing therefore depends on the supersaturation necessary to induce nucleation. If nucleation occurs readily then the system may never deviate far

from equilibrium.

This problem can also be approached by use of the bubble growth model in chapter 3. This model alone is not sufficient to provide a definitive answer, however, as it is currently based upon unrealistic conditions; it is assumed that pressure is released either instantaneously or linearly with time. As discussed in chapter 3, great progress could be made by linking this model with a model of conduit flow. The rate of pressure drop could then be calculated, not assumed, and the kinetics of degassing could be fully investigated.

How important is the loss of gas from magma by permeable flow?

Chapter 4 described the development of a model which can be used to predict the permeability of magma as it vesiculates. It was discovered that magma can become permeable at around 30% porosity (the percolation threshold), depending mainly on the presence or absence of crystals and the ease of bubble coalescence. If bubbles become aligned due to shear (Stasiuk et al. 1996) then permeability may be achieved at even lower porosities. The magnitude of the permeability is very dependent on the volume fraction of bubbles; magma at 60% porosity was found to be 1000 times more permeable than it is at 30% porosity. The model revealed that values of permeability cannot be predicted accurately without a deeper knowledge of the dynamics of bubble coalescence. If bubble coalescence is difficult (for example, if magma viscosity is high or the time available for coalescence is short), then permeability may not be achieved until the magma reaches a much higher porosity. If nucleation proceeds in a continuous, space-filling fashion (chapter 2), with subsequent bubbles nucleating far from pre-existing ones, then high porosities may be achieved before bubbles begin to coalesce and form a permeable network.

For gas to be lost from magma by permeable flow, three conditions must be satisfied: (i) the magma itself must be permeable, (ii) the walls of the conduit must be permeable and (iii) the pressure in the magma body must exceed the far-field pressure. The model

in chapter 4, together with measurements of permeability of volcanic tephra, shows that magma can indeed become permeable due to the interconnection of bubbles, but it is very difficult to ascertain the exact stage at which permeability is achieved. Field observations (Stasiuk et al. 1996) and drilling expeditions (Eichelberger et al. 1986) have revealed that conduit walls can be highly fractured; condition (ii) is therefore satisfied, at least in some cases. Numerical models of conduit flow (e.g. Jaupart and Allègre 1991; Wilson 1998) and observations of tumescence of the volcanic edifice (e.g. Voight et al. 1998) provide strong evidence for an overpressure in the conduit, fulfilling condition (iii).

It seems almost certain, therefore, that at least some gas will be lost from the system by permeable flow during an eruption. The true importance of this cannot be ascertained without considering the *rate* at which the process can occur. If magma ascends rapidly then there is little time for gas loss. On the other hand, a slow ascent rate may leave adequate time for significant amounts of gas to be released from the magma, further slowing magma expansion in a positive feedback mechanism (Jaupart and Allègre 1991). There is no simple solution of this problem; quantitative investigation of these complex and non-linear processes can only be performed by the development of a sophisticated numerical model, or by laboratory experimentation.

What are the mechanisms controlling bubble nucleation?

A detailed consideration of the physics of bubble nucleation is beyond the scope of the studies in this thesis. However, chapter 2 has provided good evidence that nucleation may occur continuously during an eruption in response to non-equilibrium degassing. This continuous nucleation requires that new bubbles can form with only modest supersaturations. Current estimates (Navon and Lyakhovsky 1998; Mourtada-Bonnefoi and Laporte 1999) of the supersaturation required to induce homogeneous nucleation are of the order of several tens of megapascals. Heterogeneous nucleation, on the other hand, can probably occur

with much lower supersaturations, perhaps less than 10 MPa (Navon and Lyakhovsky 1998). Continuous nucleation is therefore much more likely to occur through heterogeneous nucleation, probably aided by the presence of crystals. This conclusion is supported by the results of experimental studies of the degassing of silicate melts. Experimental systems which employ crystal-free melts (e.g. Lyakhovsky et al. 1996) generally produce a single nucleation event. In the experiments of Simakin et al. (1999) crystals were present in the melt and continuous nucleation was observed.

What are the effects of concentration-dependent viscosity and diffusivity on bubble growth?

The bubble growth model of chapter 3 was used to investigate in detail the dynamics of bubble growth, incorporating the dependence of both melt viscosity and volatile diffusivity on the concentration of water in the melt. It was found that the concentration-dependent nature of both viscosity and diffusivity exerts a strong control on bubble growth. In particular, a strong coupling between the effects of viscosity and diffusivity was revealed. A high diffusivity (which promotes bubble growth) leads to a fast dehydration of the melt and hence a rapid increase in melt viscosity (which inhibits growth). Bubble growth rates are the result of a competition between these two factors.

The incorporation of concentration-dependent diffusivity has an unexpectedly large effect on bubble growth; unexpected considering that diffusivity varies over less than two orders of magnitude during an eruption, whereas the melt viscosity varies over five or six orders of magnitude. If diffusivity is concentration-dependent, the form of the concentration profile in the melt is different from that given by a constant diffusivity. This leads to a lower effective melt viscosity and hence a higher rate of bubble growth.

In general, therefore, many important features of the dynamics of bubble growth cannot be captured if either viscosity or diffusivity is assumed constant. For cases of near-equilibrium

degassing these effects are less important but, as discussed above, the nature of degassing (equilibrium or non-equilibrium) cannot be assumed *a priori*, but must be investigated fully.

What can the textures of volcanic rocks tell us about eruption processes?

There are many textural parameters which could be measured in thin sections of volcanic rocks, including the shape of bubbles and their spatial arrangement. In this thesis (chapter 2) a different parameter, the bubble size distribution (BSD), was investigated. Using evidence from a numerical model, analogue experiments and examination of natural samples, it was shown that the presence of an exponential or power law BSD was indicative of a process of continuous bubble nucleation.

It is much more difficult to relate other textural parameters, such as bubble shape factors, directly to eruption processes. One reason for this is that the shape of bubbles is a product of many poorly-understood processes such as bubble coalescence, the mechanical interactions between bubbles and the distortion of bubbles due to internal strains in the magma. It may be possible to draw empirical correlations between bubble shape factors (e.g. perimeter-area relationships, the fractal dimension of the bubble) and eruption parameters which have been deduced by other means. Such a purely empirical study would, however, be weakened by a lack of a physical mechanism which could explain the observations. The strength of the study in chapter 2 lies in its ability to explain the observed textures (BSDs) in terms of real physical processes of bubble nucleation and growth. Furthermore, the results of the study are insensitive to the details of the vesiculation process which are, in any case, not completely understood.

Concluding remarks

In this thesis, each aspect of magmatic degassing (nucleation, bubble growth and permeability development) has been examined individually in order to gain a deeper understanding of the physics involved. Many important results have been revealed, but their true significance cannot be proven without an investigation of the effects of these processes on the dynamics of volcanic eruptions as a whole. It is hoped that the findings of these investigations will be incorporated into future studies to create ever more realistic simulations of volcanic eruptions.

Chapter 6

References

ALIDIBIROV M. A. (1994) A model for viscous magma fragmentation during volcanic blasts. *Bulletin of Volcanology* **56**, 459-465.

ANISHCHIK S. V. and MEDVEDEV N. N. (1995) Three-dimensional Apollonian packing as a model for dense granular systems. *Physical Review Letters* **75**, 4314-4317.

BAGDASSAROV N. S., DINGWELL D. B. and WILDING M. C. (1996) Rhyolite magma degassing: an experimental study of melt vesiculation. *Bulletin of Volcanology* **57**, 587-601.

BAGDASSAROV N. S. and DINGWELL D. B. (1992) A rheological investigation of vesicular rhyolite. *Journal of Volcanology and Geothermal Research* **50**, 307-322.

BARCLAY J., CARROLL M. R., HOUGHTON B. F. and WILSON C. J. N. (1996) Pre-eruptive volatile content and degassing history of an evolving peralkaline volcano. *Journal of Volcanology and Geothermal Research* **74**, 75-87.

BARCLAY J., RUTHERFORD M. J., CARROLL M. R., MURPHY M. D., DEVINE J. D., GARDNER J. and SPARKS R. S. J. (1998) Experimental phase equilibria constraints on pre-eruptive storage conditions of the Soufriere Hills magma. *Geophysical Research Letters* **25**, 3437-3440.

BARCLAY J., RILEY D. S. and SPARKS R. S. J. (1995) Analytical models for bubble growth during decompression of high viscosity magmas. *Bulletin of Volcanology* **57**, 422-431.

BLOWER J. D. (2001) A three-dimensional network model of permeability in vesicular material. *Computers and Geosciences* **27**, 115-119.

BLOWER J. D., KEATING J. P., MADER H. M. and PHILLIPS J. C. (2001) Inferring volcanic degassing processes from vesicle size distributions. *Geophysical Research Letters* **28**, 347-350.

BOSL W. J., DVORKIN J. and NUR A. (1998) A study of porosity and permeability using a lattice Boltzmann simulation. *Geophysical Research Letters* **25**, 1475-1478.

BOURBIE T. and ZINSZNER B. (1985) Hydraulic and acoustic properties as a function of porosity in Fontainebleau sandstone. *Journal of Geophysical Research, B* **90**, 11524-11532.

BRAITHWAITE M., LYNCH P. M., PARKER I. B., JONES A. F. and WILSON S. D. R. (1999) Compressional heating of isolated gas bubbles in reactive media. *Mathematical Engineering in Industry* **7**, 361-387.

BURNARD P. (1999) Eruption dynamics of "popping rock" from vesicle morphologies. *Journal of Volcanology and Geothermal Research* **92**, 247-258.

CASADEVALL T. J., ROSE W. I. J., GERLACH T., GREENLAND L. P., EWERT J., WUNDERMAN R. and SYMONDS R. (1983) Gas emissions and the eruption of Mount St Helens through 1982. *Science* **221**, 1383-1385.

CASHMAN K. V. and MARSH B. D. (1988) Crystal size distribution (CSD) in rocks and the kinetics and dynamics of crystallization: II. Makaopuhi lava lake. *Contributions to Mineralogy and Petrology* **99**, 292-305.

CRANK J. (1975) *The mathematics of diffusion*, 2nd ed., Clarendon Press, 414p.

CRAVERO M. and FIDELIBUS C. (1999) A code for scaled flow simulations on generated fracture networks. *Computers and Geosciences* **25**, 191-195.

DINGWELL D. B. (1998) Recent experimental progress in the physical description of silicic magma relevant to explosive volcanism. In *The physics of explosive volcanic eruptions* (eds. J. S. GILBERT and R. S. J. SPARKS), pp. 9-26. Geological Society.

EICHELBERGER J. C., CARRIGAN C. R., WESTRICH H. R. and PRICE R. H. (1986) Non-explosive silicic volcanism. *Nature* **323**, 598-602.

EINSTEIN A. (1906) Eine neue Bestimmung der Moleküldimensionen. *Annalen der Physik* **19**, 289-306.

EINSTEIN A. (1911) Berichtigung zu meiner Arbeit: "Eine neue Bestimmung der Molekül-dimensionen". *Annalen der Physik* **34**, 591-592.

FENG S., HALPERIN B. I. and SEN P. N. (1987) Transport properties of continuum systems near the percolation threshold. *Physical Review, B* **35**, 197-214.

FIDLER J. K. (1988) *Introductory circuit theory*, McGraw-Hill.

FINK J. H. (1983) Structure and emplacement of a rhyolitic obsidian flow: Little Glass Mountain, Medicine Lake Highland, northern California. *Bulletin of the Geological Society*

of America **94**, 362-380.

FINK J. H., ANDERSON S. W. and MANLEY C. R. (1992) Textural constraints on effusive silicic volcanism: beyond the permeable foam model. *Journal of Geophysical Research, B* **97**, 9073-9083.

FRANKEL N. A. and ACRIVOS A. (1970) The constitutive equation for a dilute emulsion. *Journal of Fluid Mechanics* **44**, 65-78.

FRIEDMAN I. (1989) Are extrusive rhyolites produced from permeable foam eruptions? *Bulletin of Volcanology* **51**, 69-71.

GAONAC'H H., LOVEJOY S., STIX J. and SCHERTZER D. (1996) A scaling growth model for bubbles in basaltic lava flows. *Earth and Planetary Science Letters* **139**, 395-409.

GAONAC'H H., STIX J. and LOVEJOY S. (1996) Scaling effects on vesicle shape, size and heterogeneity of lavas from Mount Etna. *Journal of Volcanology and Geothermal Research* **74**, 131-153.

GARDNER C. A., CASHMAN K. V. and NEAL C. A. (1998) Tephra-fall deposits from the 1992 eruption of Crater Peak, Alaska: implications of clast textures for eruptive processes. *Bulletin of Volcanology* **59**, 537-555.

GARDNER J. E., HILTON M. and CARROLL M. R. (2000) Bubble growth in highly viscous silicate melts during continuous decompression from high pressure. *Geochimica et Cosmochimica Acta* **64**, 1473-1483.

GARDNER J. E., THOMAS R. M. E., JAUPART C. and TAIT S. (1996) Fragmentation of magma during Plinian volcanic eruptions. *Bulletin of Volcanology* **58**, 144-162.

GARDNER J. E., HILTON M. and CARROLL M. R. (1999) Experimental constraints on degassing of magma: isothermal bubble growth during continuous decompression from high pressure. *Earth and Planetary Science Letters* **168**, 201-218.

GRIMMETT G. (1999) *Percolation*, 2nd ed., Springer-Verlag, 444p.

HERD R. A. and PINKERTON H. (1997) Bubble coalescence in basaltic lava: Its impact on the evolution of bubble populations. *Journal of Volcanology and Geothermal Research* **75**, 137-157.

HESS K.-U. and DINGWELL D. B. (1996) Viscosities of hydrous leucogranitic melts: A non-Arrhenian model. *American Mineralogist* **81**, 1297-1300.

HILL L. G. and STURTEVANT B. (1989) An experimental study of evaporation waves in a superheated liquid. In *Adiabatic waves in liquid-vapour systems- IUTAM Symposium Göttingen, Germany* (eds. G. E. A. MEIER and P. A. THOMPSON), pp. 25-37. Springer-Verlag.

HILL L. G. (1991) An experimental study of evaporation waves in a superheated liquid. Ph.D. Dissertation, California Institute of Technology.

INAMURO T., YOSHINO M. and OGINO F. (1999) Lattice Boltzmann simulation of flows in a three-dimensional porous structure. *International Journal for Numerical Methods in Fluids* **29**, 737-748.

JAUPART C. (1998) Gas loss from magmas through conduit walls during eruption. In *The physics of explosive volcanic eruptions* (eds. J. S. GILBERT and R. S. J. SPARKS), pp. 73-90. Geological Society.

JAUPART C. and ALLÈGRE C. J. (1991) Gas content, eruption rate and instabilities of eruption regime in silicic volcanoes. *Earth and Planetary Science Letters* **102**, 413-429.

KLUG C. and CASHMAN K. V. (1994) Vesiculation of May 18, 1980, Mount St. Helens magma. *Geology* **22**, 468-472.

KLUG C. and CASHMAN K. V. (1996) Permeability development in vesiculating magmas: implications for fragmentation. *Bulletin of Volcanology* **58**, 87-100.

LARSEN J. F. and GARDNER J. E. (2000) Experimental constraints on bubble interactions in rhyolite melts: implications for vesicle size distributions. *Earth and Planetary Science Letters* **180**, 201-214.

LEE S. B. (1990) Universality of continuum percolation. *Physical Review, B* **42**, 4877-4880.

LEJEUNE A. M., BOTTINGA Y., TRULL T. W. and RICHET P. (1999) Rheology of bubble-bearing magmas. *Earth and Planetary Science Letters* **166**, 71-84.

LEJEUNE A. M. and RICHET P. (1995) Rheology of crystal- bearing silicate melts - an experimental study at high viscosities. *Journal of Geophysical Research, B* **100**, 4215-4229.

LIU Y. and ZHANG Y. (2000) Bubble growth in rhyolitic melt. *Earth and Planetary Science Letters* **181**, 251-264.

LYAKHOVSKY V., HURWITZ S. and NAVON O. (1996) Bubble growth in rhyolitic melts: experimental and numerical investigation. *Bulletin of Volcanology* **58**, 19-32.

MADER H. M., BRODSKY E. E., HOWARD D. and STURTEVANT B. (1997) Laboratory simulations of sustained volcanic eruptions. *Nature* **388**, 462-464.

MADER H. M., PHILLIPS J. C., SPARKS R. S. J. and STURTEVANT B. (1996) Dynamics of explosive degassing of magma: Observations of fragmenting two-phase flows. *Journal of Geophysical Research, B* **101**, 5547-5560.

MADER H. M., ZHANG Y., PHILLIPS J. C., SPARKS R. S. J., STURTEVANT B. and STOLPER E. M. (1994) Experimental simulations of explosive degassing of magma. *Nature* **372**, 85-88.

MANGA M., CASTRO J., CASHMAN K. V. and LOEWENBERG M. (1998) Rheology of bubble-bearing magmas. *Journal of Volcanology and Geothermal Research* **87**, 15-28.

MANGAN M. and SISSON T. (2000) Delayed, disequilibrium degassing in rhyolite magma: decompression experiments and implications for explosive volcanism. *Earth and Planetary Science Letters* **183**, 441-455.

MANGAN M. T. and CASHMAN K. V. (1996) The structure of basaltic scoria and reticulite and inferences for vesiculation, foam formation, and fragmentation in lava fountains. *Journal of Volcanology and Geothermal Research* **73**, 1-18.

MANGAN M. T., CASHMAN K. V. and NEWMAN S. (1993) Vesiculation of basaltic magma during eruption. *Geology* **21**, 157- 160.

MANWART C., TORQUATO S. and HILFER R. (2000) Stochastic reconstruction of sandstones. *Physical Review, E* **62**, 893-899.

MARSH B. D. (1988) Crystal size distribution (CSD) in rocks and the kinetics and dynamics of crystallization: I. Theory. *Contributions to Mineralogy and Petrology* **99**, 277-291.

MARTÍ J., SORIANO C. and DINGWELL D. B. (1999) Tube pumices as strain markers of the ductile-brittle transition during magma fragmentation. *Nature* **402**, 650-653.

MCBIRNEY A. R. (1973) Factors governing the intensity of explosive andesitic eruptions. *Bulletin of Volcanology* **37**, 443-453.

MCBIRNEY A. R. and MURASE T. (1970) Factors governing the formation of pyroclastic rocks. *Bulletin of Volcanology* **34**, 372- 384.

MCBIRNEY A. R. (1963) Factors governing the nature of submarine volcanism. *Bulletin of Volcanology* **26**, 455-469.

MELNIK O. (2000) Dynamics of two-phase conduit flow of high-viscosity gas-saturated magma: large variations of sustained explosive eruption intensity. *Bulletin of Volcanology* **62**, 153-170.

MELNIK O. E. (1999) Fragmenting magma. *Nature* **397**, 394- 395.

MELNIK O. E. and SPARKS R. S. J. (1999) Nonlinear dynamics of lava dome extrusion. *Nature* **402**, 37-41.

MOURTADA-BONNEFOI C. C. and LAPORTE D. (1999) Experimental study of homogeneous bubble nucleation in rhyolitic magmas. *Geophysical Research Letters* **26**, 3505-3508.

MOURTADA-BONNEFOI C. C. and MADER H. M. (2001) On the development of highly-viscous skins of liquid around bubbles during magmatic degassing. *Geophysical Research Letters*, in press.

MURASE T. and MCBIRNEY A. R. (1973) Properties of some common igneous rocks and their melts at high temperatures. *Bulletin of the Geological Society of America* **84**, 3563-3592.

NAVON O., CHEKHMIR A. and LYAKHOVSKY V. (1998) Bubble growth in highly viscous melts: theory, experiments, and autoexplosivity of dome lavas. *Earth and Planetary Science Letters* **160**, 763-776.

NAVON O. and LYAKHOVSKY V. (1998) Vesiculation processes in silicic magmas. In *The physics of explosive volcanic eruptions* (eds. J. S. GILBERT and R. S. J. SPARKS), pp. 27-50. Geological Society.

NOWAK M. and BEHRENS H. (1997) An experimental investigation of diffusion of water in haplogranitic melts. *Contributions to Mineralogy and Petrology* **126**, 365-376.

PAPALE P. (1999) Strain-induced magma fragmentation in explosive eruptions. *Nature* **397**, 425-428.

PAPALE P., NERI A. and MACEDONIO G. (1998) The role of magma composition and water content in explosive eruptions: 1. Conduit ascent dynamics. *Journal of Volcanology and Geothermal Research* **87**, 75-93.

PAPALE P. and POLACCI M. (1999) Role of carbon dioxide in the dynamics of magma ascent in explosive eruptions. *Bulletin of Volcanology* **60**, 583-594.

PHILLIPS J. C., LANE S. J., LEJEUNE A. M. and HILTON M. (1995) Gum rosin-acetone system as an analogue to the degassing behaviour of hydrated magmas. *Bulletin of Volcanology* **57**, 263- 268.

PINKERTON H. and STEVENSON R. J. (1992) Methods of determining the rheological properties of magmas at sub-liquidus temperatures. *Journal of Volcanology and Geothermal Research* **53**, 47-66.

PITZER K. S. and STERNER S. M. (1994) Equations of state valid continuously from zero to extreme pressures for H_2O and CO_2. *Journal of Chemical Physics* **101**, 3111-3116.

PRESS W. H., TEUKOLSKY S. A., VETTERLING W. T. and FLANNERY B. P. (1992) *Numerical Recipes in Fortran*, 2nd ed., Cambridge University Press, 933p.

PROUSSEVITCH A. A. and SAHAGIAN D. L. (1996) Dynamics of coupled diffusion and decompressive bubble growth in magmatic systems. *Journal of Geophysical Research, B* **101**, 17447-17455.

PROUSSEVITCH A. A. and SAHAGIAN D. L. (1998) Dynamics and energetics of bubble growth in magmas: Analytical formulation and numerical modelling. *Journal of Geophysical Research, B* **103**, 18223- 18251.

PROUSSEVITCH A. A., SAHAGIAN D. L. and ANDERSON A. T. (1993a) Dynamics of diffusive bubble growth in magmas: isothermal case. *Journal of Geophysical Research, B* **98**, 22283-22307.

PROUSSEVITCH A. A., SAHAGIAN D. L. and KUTOLIN V. A. (1993b) Stability of foams in silicate melts. *Journal of Volcanology and Geothermal Research* **59**, 161-178.

RENARDY Y. (1987) Viscosity and density stratification in vertical Poiseuille flow. *Physics of Fluids* **30**, 1638-1648.

ROUAULT Y. (1999) The construction of an Appolonian packing. *Powder Technology* **102**, 274-280.

RUTHERFORD M. J. and HILL P. M. (1993) Magma ascent rates from amphibole break-down: An experimental study applied to the 1980-1986 Mount St. Helens eruptions. *Journal of Geophysical Research, B* **98**, 19667-19685.

RYAN M. P. (1988) The mechanics and 3-dimensional internal structure of active magmatic systems- Kilauea volcano, Hawaii. *Journal of Geophysical Research, B* **93**, 4213-4248.

SAAR M. O. and MANGA M. (1999) Permeability-porosity relationship in vesicular basalts. *Geophysical Research Letters* **26**, 111-114.

SAHAGIAN D. L. (1999) Magma fragmentation in eruptions. *Nature* **402**, 589-591.

SAHAGIAN D. L. and PROUSSEVITCH A. A. (1998) 3D particle size distributions from 2D observations: stereology for natural applications. *Journal of Volcanology and Geothermal Research* **84**, 173-196.

SAHAGIAN D. L., PROUSSEVITCH A. A. and ANDERSON A. T. (1994) Reply to Sparks RSJ (1994) Comment on 'Dynamics of diffusive bubble growth in magmas: isothermal case' by Proussevitch AA, Sahagian DL, Anderson AT (J Geophys Res 98:22283-22308, 1993). *Journal of Geophysical Research, B* **99**, 17829-17832.

SAHIMI M. (1994) *Applications of percolation theory*, Taylor & Francis Ltd., 258p.

SARDA P. and GRAHAM D. (1990) Mid-ocean ridge popping rocks: implications for de-gassing at ridge crests. *Earth and Planetary Science Letters* **97**, 268-289.

SCRIVEN L. E. (1959) On the dynamics of phase growth. *Chemical Engineering Science* **10**, 1-13.

SHAW H. R. (1972) Viscosities of magmatic silicate liquids: An empirical method of pre-diction. *American Journal of Science* **272**, 870-893.

SHEPHERD J. B., HERD R. A., JACKSON P. and WATTS R. (1998) Ground deformation measurements at the Soufriere Hills Volcano, Montserrat: II: Rapid static GPS measure-ments June 1996-June 1997. *Geophysical Research Letters* **25**, 3413-3416.

SIMAKIN A. G., ARMIENTI P. and EPEL'BAUM M. B. (1999) Coupled degassing and crys-tallization: experimental study at continuous pressure drop, with application to volcanic bombs. *Bulletin of Volcanology* **61**, 275-287.

SPARKS R. S. J. (1978) The dynamics of bubble formation and growth in magmas: a review and analysis. *Journal of Volcanology and Geothermal Research* **3**, 1-37.

SPARKS R. S. J. (1994) Comment on "Dynamics of diffusive bubble growth in magmas: isothermal case" by A.A. Proussevitch, D.L. Sahagian and A.T. Anderson. *Journal of Geophysical Research, B* **99**(9), 17827-17828.

SPARKS R. S. J. (1997) Causes and comsequences of pressurisation in lava dome eruptions. *Earth and Planetary Science Letters* **150**, 177-189.

SPARKS R. S. J. and BRAZIER S. (1982) New evidence for degassing processes during explosive eruptions. *Nature* **295**, 218- 220.

STASIUK M. V., BARCLAY J., CARROLL M. R., JAUPART C., RATTÉ J. C., SPARKS R. S. J. and TAIT S. R. (1996) Degassing during magma ascent in the Mule Creek vent (USA). *Bulletin of Volcanology* **58**, 117-130.

STEIN D. J. and SPERA F. J. (1992) Rheology and microstructure of magmatic emulsions: theory and experiments. *Journal of Volcanology and Geothermal Research* **49**, 157-174.

STERNER S. M. and PITZER K. S. (1994) An equation of state for carbon dioxide valid from zero to extreme pressures. *Contributions to Mineralogy and Petrology* **117**, 362-374.

TAYLOR B. E., EICHELBERGER J. C. and WESTRICH H. R. (1983) Hydrogen isotopic evidence of rhyolitic magma degassing during shallow intrusion and eruption. *Nature* **306**, 541-545.

TAYLOR G. I. (1932) Viscosity of a fluid containing small drops of another fluid. *Proceedings of the Royal Society, A* **138**, 41-48.

THOMAS N., JAUPART C. and VERGNIOLLE S. (1994) On the vesicularity of pumice. *Journal of Geophysical Research, B* **99**, 15633-15644.

TORAMARU A. (1989) Vesiculation process and bubble size distributions in ascending magmas with constant velocities. *Journal of Geophysical Research, B* **94**, 17523-17542.

TORAMARU A. (1990) Measurement of bubble-size distributions in vesiculated rocks with implications for quantitative estimation of eruption processes. *Journal of Volcanology and Geothermal Research* **43**, 71-90.

TORAMARU A. (1995) Numerical study of nucleation and growth of bubbles in viscous magmas. *Journal of Geophysical Research, B* **100**, 1913-1931.

TUCKWELL H. C. (1988) *Elementary applications of probability theory*, Chapman and Hall, 225p.

TURCOTTE D. L. (1992) *Fractals and chaos in geology and geophysics*, Cambridge University Press, 221p.

VERHOOGEN J. (1951) Mechanics of ash formation. *American Journal of Science* **249**, 729-739.

VOIGHT B., HOBLITT R. P., CLARKE A. B., LOCKHART A. B., MILLER A. D., LYNCH L. and McMAHON J. (1998) Remarkable cyclic ground deformation monitored in real-time on Montserrat, and its use in eruption forecasting. *Geophysical Research Letters* **25**, 3405-3408.

WATSON E. B. (1994) Diffusion in volatile-bearing magmas. In *Reviews in Mineralogy* (eds. M. R. CARROLL and J. R. HOLLOWAY), Vol. 30, pp. 371-411. Mineralogical Society of America.

WESTRICH H. R. and EICHELBERGER J. C. (1994) Gas transport and bubble collapse in rhyolitic magma: an experimental approach. *Bulletin of Volcanology* **56**, 447-458.

WHITHAM A. G. and SPARKS R. S. J. (1986) Pumice. *Bulletin of Volcanology* **48**, 209-223.

WILSON L., SPARKS R. S. J. and WALKER G. P. L. (1980) Explosive volcanic eruptions-IV. The control of magma properties and conduit geometry on eruption column behaviour. *Geophysical Journal of the Royal Astronomical Society* **63**, 117-148.

WILSON S. D. R. (1998) A mechanism for the lateral transport of gas bubbles in silicic lava rising in a vertical conduit. *Earth and Planetary Science Letters* **156**, 13-18.

WOODS A. W. and KOYAGUCHI T. (1994) Transitions between explosive and effusive eruptions of silicic magmas. *Nature* **370**, 641-644.

WYLIE J. J., VOIGHT B. and WHITEHEAD J. A. (1999) Instability of magma flow from volatile-dependent viscosity. *Science* **285**, 1883-1885.

ZHANG Y. (1999a) A criterion for the fragmentation of bubbly magma based on brittle failure theory. *Nature* **402**, 648-650.

ZHANG Y. (1999b) H_2O in rhyolitic glasses and melts: measurement, speciation, solubility, and diffusion. *Reviews of Geophysics* **37**, 493-516.

ZHANG Y.AND BEHRENS H. (2000) H_2O diffusion in rhyolitic melts and glasses. *Chemical Geology* **169**, 243-262.

ZHANG Y., STOLPER E. M. and WASSERBURG G. J. (1991) Diffusion of water in rhyolitic glasses. *Geochimica et Cosmochimica Acta* **55**, 441-456.

ZHANG Y., STURTEVANT B. and STOLPER E. M. (1997) Dynamics of gas-driven eruptions: Experimental simulations using CO_2-H_2O- polymer system. *Journal of Geophysical Research, B* **102**, 3077- 3096.

Appendix A

Stereology

Given a distribution $F(R)$ of randomly-placed spheres in three-dimensional space, we wish to find the expected distribution $f(r)$ of circular slices resulting from the intersection of a plane and the spheres.

Figure A.1 shows the intersection of a spherical bubble of radius R by a plane distant x from the bubble centre. The radius of the circle described by the intersection of the plane and the sphere is r where

$$r = \sqrt{R^2 - x^2} \tag{A.1}$$

A.1 Monodisperse BSD

The simplest case which shall be dealt with first is that of a monodisperse distribution (i.e. all the bubbles have the same radius). If these bubbles are randomly positioned, then a slice through the population will generate a range of circle sizes; some bubbles will be intersected near a diameter and will appear as a circle of radius $\sim R$, whilst others will be intersected away from a diameter and will appear as smaller circles (see figure 4.5 for
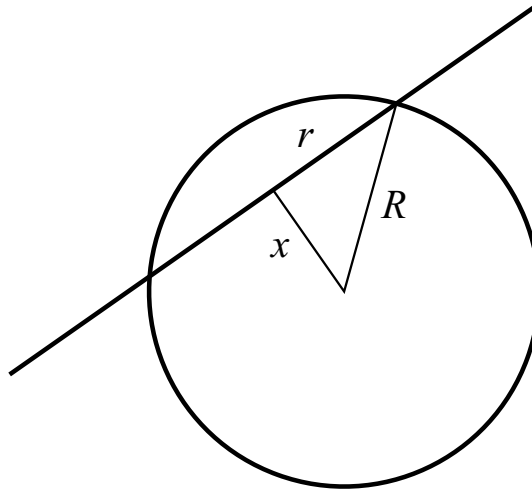
Figure A.1: The intersection of a spherical bubble of radius R with a plane at a distance x from the bubble centre. The radius of the circular slice of the bubble in the plane is r.

an illustration of this).

From equation A.1:

$$x = \sqrt{R^2 - r^2}$$

$$\Rightarrow \frac{\mathrm{d}x}{\mathrm{d}r} = \frac{r}{\sqrt{R^2 - r^2}} \tag{A.2}$$

From the laws of probability:

$$|f(x)\,\mathrm{d}x| = |f(r)\,\mathrm{d}r|$$

$$\Rightarrow f(r) = f(x)\left|\frac{\mathrm{d}x}{\mathrm{d}r}\right| \tag{A.3}$$

where $f(r)$ and $f(x)$ are the probability density functions of r and x respectively.

Now, since each value of x has an equal chance of occurring and $0 \leq x \leq R$, $f(x) = 1/R$. Therefore
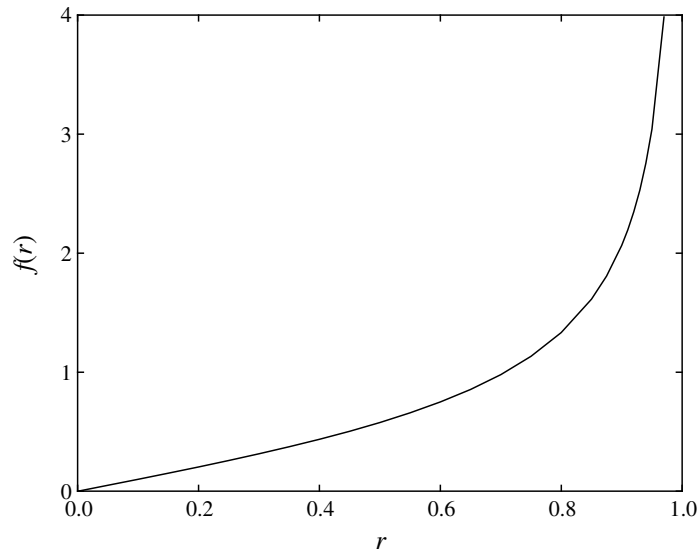
$$f(r) = \frac{1}{R}\frac{r}{\sqrt{R^2 - r^2}} \tag{A.4}$$

Figure A.2: The expected two-dimensional size distribution (probability density function, $f(r)$) of circles produced by the intersection of a plane with a monodisperse distribution of spheres of unit radius whose centres are placed at random.

Figure A.2 shows the form of the expected two-dimensional slice distribution in the case of a monodisperse BSD. The average slice radius $\bar{r}$ is given by:

$$\bar{r} = \int r f(r)\, \mathrm{d}r \quad = \quad \frac{1}{R} \int_0^R \frac{r^2}{\sqrt{R^2 - r^2}} \quad = \quad \frac{\pi}{4} R \tag{A.5}$$

A.2 Polydisperse BSDs— the general case

Equation A.4 gives the probability of obtaining a circular cross-section of radius r given the intersection of a plane with a sphere of radius R. Now let us consider a polydisperse distribution of bubbles with probability density function $F(R)$. The probability of a plane intersecting a given bubble is proportional to the bubble radius R. Cross-sections of radius r may be obtained from any bubble with a radius greater than or equal to r. We may now write a general expression for the probability of obtaining a cross-section of radius r from

the whole distribution:

$$f(r) = \int_r^\infty F(R)\, R\, \frac{1}{R} \frac{r}{\sqrt{R^2 - r^2}}\, \mathrm{d}R \qquad \text{(A.6)}$$

That is to say, $f(r)$ is the probability of finding a bubble of radius R, multiplied by the probability of intersecting this bubble, multiplied by the probability of obtaining a slice of radius r from this bubble, integrated over the range of $R \geq r$. This gives:

$$f(r) = \int_r^\infty \frac{r}{\sqrt{R^2 - r^2}}\, F(R)\, \mathrm{d}R \qquad \text{(A.7)}$$

A.2.1 Power law (fractal) BSD

The general form of a power law (or fractal) bubble size distribution is

$$F(R) = aR^{-\alpha} \qquad \text{(A.8)}$$

where a is a constant and α is the power law exponent. From equation A.7:

$$f(r) = \int_r^\infty \frac{r}{\sqrt{R^2 - r^2}}\, aR^{-\alpha}\, \mathrm{d}R \qquad \text{(A.9)}$$

Substituting $R = ry$ giving $\mathrm{d}R = r\, \mathrm{d}y$:

$$\begin{aligned} f(r) &= a \int_1^\infty \frac{r}{\sqrt{r^2 y^2 - r^2}},\ (ry)^{-\alpha}\, r\, \mathrm{d}y \\ &= ar^{1-\alpha} \int_1^\infty \frac{y^{-\alpha}}{\sqrt{y^2 - 1}}\, \mathrm{d}y \end{aligned} \qquad \text{(A.10)}$$

Noting that the integral factor is simply a number (which is a function of α) we obtain:

$$f(r) \propto r^{-(\alpha - 1)} \qquad \text{(A.11)}$$

This is an important result; it states that if the size distribution of bubble is in the form of a power law with exponent α then the size distribution of slices is also in the form of a power law with an exponent of $(\alpha - 1)$.

Appendix B

The physical properties of gum rosin/acetone solutions

In chapter 2 a series of analogue shock-tube experiments used to investigate explosive degassing are described. The experiments employ the gum rosin and acetone (GRA) liquid system. The purpose of this appendix is to characterize the basic physical properties of GRA solutions.

Gum rosin (natural pine resin) is supplied as glassy, amorphous solid blocks. A jaw crusher is used to break these blocks up into gravel-sized pieces. GRA solutions are produced by adding a known mass of gum rosin to a known mass of acetone in a 1-litre conical flask and stirring using a powerful magnetic stirrer. Dissolution takes place on a timescale of a few hours. The smaller the acetone concentration, the longer the dissolution time.

B.1   The rheology of GRA solutions

B.1.1   Rotary viscometry

The rheology of the GRA solutions was investigated using a Haake RV20 rotary viscometer (figure B.1a). This employs a concentric-cylinder sensor system (figure B.1b) and is a controlled-rate device; the user specifies the rotation rate to be applied to the sample
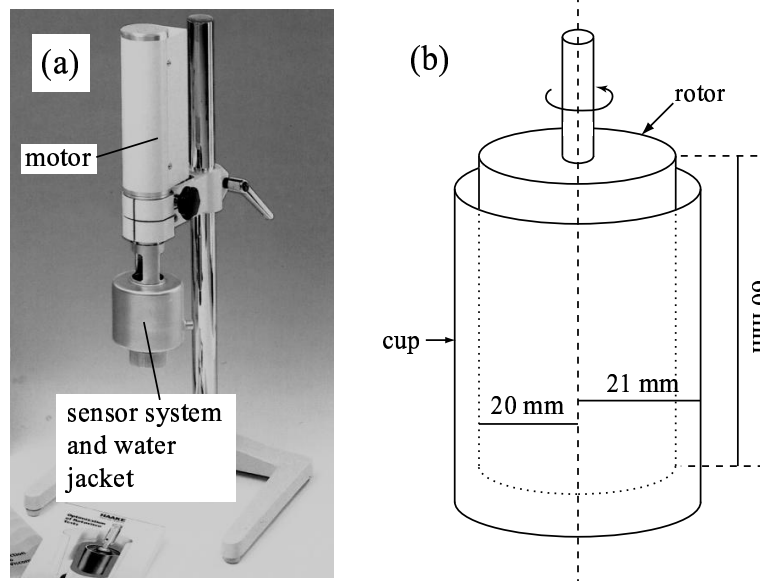
Figure B.1: (a) The Haake RV20 rotary viscometer. The sensor system is surrounded by a water jacket for temperature regulation. (b) Diagrammatic representation of the MV1 concentric-cylinder sensor mechanism. The rotor is shown slightly raised out of the cup for clarity. The solution under test is placed between the cup and rotor. The rotor rotates at a prescribed rate and the torque required to maintain this rotation rate is measured.

and the driveshaft torque required to maintain this rotation rate is calculated. The MV1 sensor system was employed— this is suitable for measuring viscosities in the range 10^{-2} to 10^5 Pa s. The equipment was calibrated against silicone oils of known (Newtonian) viscosity.

In a typical measurement (figure B.2a) the rotation rate is increased linearly over a few minutes to a prescribed maximum value, and is then decreased at the same rate to zero. The required rotation rate is calculated (by the system software) from the given strain rate using the physical dimensions of the sensor system. The instantaneous stress is calculated from the instantaneous driveshaft torque, which is in turn calculated from the current required to drive the motor at the required rotation rate.

The major control on the viscosity of a sample of GRA solution is its acetone content. In the experiments discussed in this appendix and in chapter 2, the temperature is always
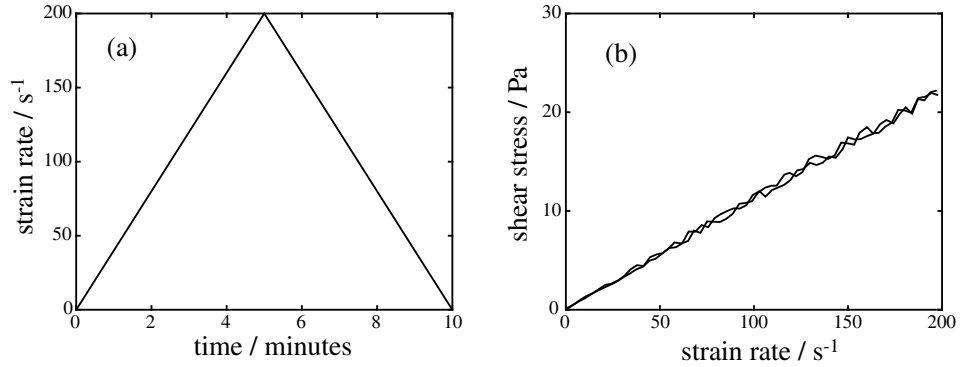
Figure B.2: An example of viscosity measurement using the Haake RV20 rotary viscometry system. The sample under test is a freshly-prepared solution of GRA with 25 wt.% acetone. (a) The user specifies the strain rate as a function of time. The strain rate is increased linearly over time to some maximum value, then decreased at the same rate to zero. (b) Shear stress as a function of strain rate. In this case the rheology of the sample is Newtonian with a well-constrained viscosity of 0.112 Pa s. (The viscosity is the gradient of the graph of shear stress vs strain rate.)

20°C. Provided that the measurement of viscosity is performed less than ∼ 12 hours after the solution is prepared (see section B.1.2), the solution exhibits a Newtonian rheology. Measurements were made at 20, 25 and 30 wt.% acetone, and table B.1 shows the viscosities obtained. Measurements of viscosity at lower concentrations were made by Phillips et al. (1995). Figure B.3 combines the data from this study and the present work.

B.1.2   Problems

The main difficulty in characterizing the rheology of GRA solutions is that the solution properties change over time. Viscosities gradually increase over a period of hours (figure B.4) and after 12 to 24 hours, depending on the acetone content, the rheology departs significantly from Newtonian. (figure B.5). In order to ensure that the rheology of the solution in a shock-tube experiment is Newtonian, therefore, only freshly-prepared solutions

Acetone concentration (wt.%)	Viscosity (Pa s)
0	10^{13}
12	19
15	6.1
20	0.80
25	0.11
30	0.044

Table B.1: GRA viscosity measurements at different acetone concentrations at 20°C. Measurements at 0, 12 and 15 wt.% acetone were taken from Phillips et al. (1995).
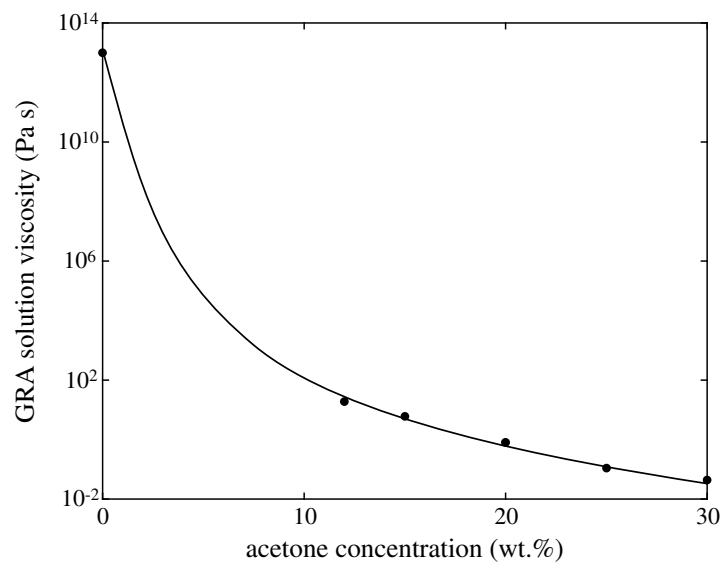

Figure B.3: The viscosity of GRA solution as a function of its acetone concentration at 20°C. Data are in table B.1.
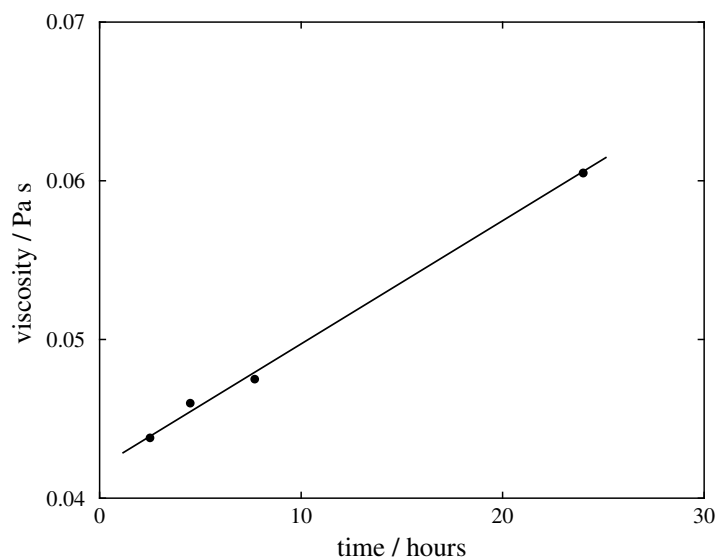
Figure B.4: The increase in viscosity of a sample of 30 wt.% GRA solution with time since the gum rosin and acetone were first mixed. Note that the dissolution time was 2.5 hours so there are no measurements of viscosity before this time.

are used.

B.2 Diffusivity of acetone in GRA solutions

B.2.1 Experimental method

The diffusivity of acetone in solutions of GRA was measured using a weight-loss method. The experimental procedure is as follows (figure B.6): A sample of GRA solution is poured into a shallow, glass-bottomed circular dish with vertical sides and diameter 91.7 mm, to a depth of ~ 1 mm. The dish is placed on a sensitive balance (accurate to 0.5 mg) in a fume cupboard at constant temperature. The mass of the dish and solution film over time is measured as the acetone evaporates from the free surface. The supply of acetone to the free surface and hence the evaporation rate is controlled by the diffusivity of acetone in the solution.
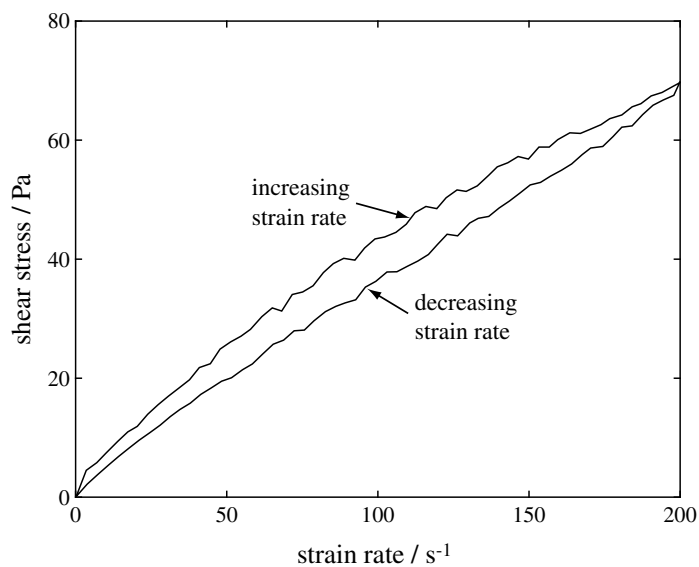
Figure B.5: Development of non-Newtonian rheology in a sample of GRA solution. The sample under test is from the same batch of solution as that in figure B.2b but the solution is now 24 hours old. Not only is the graph of shear stress vs strain rate non-linear, but the rheology is different for increasing and decreasing strain rate (figure B.2a).
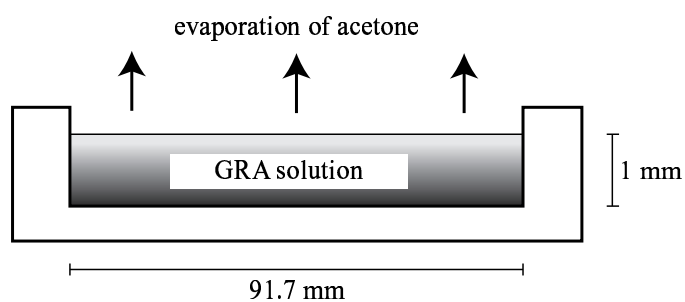

Figure B.6: The experimental apparatus used to measure the diffusivity of acetone in GRA solutions.

B.2.2   Calculation of diffusivity

The diameter of the dish is much greater than the thickness of the film, and only one surface is exposed to the atmosphere. The diffusion of acetone to the free surface proceeds to a good approximation in one direction only, being perpendicular to the solution surface. The one-dimensional diffusion equation is:

$$\frac{\partial c}{\partial t} = \frac{\partial}{\partial x}\left(D(c)\frac{\partial c}{\partial x}\right) \tag{B.1}$$

where c is the concentration (mass fraction) of acetone in the film, x is the spatial coordinate, t is time and $D(c)$ is the diffusion coefficient which is a function of the acetone concentration (see B.2.2). Unfortunately, the concentration-dependent nature of the diffusivity means that no analytical solutions exist for equation B.1. However, solutions can be found if D is assumed constant. In this case D is an 'effective' diffusivity.

Solution of the diffusion equation

The author is very grateful to Professor J.P. Keating of the School of Mathematics, University of Bristol for the following derivation.

We are required to solve equation B.1 subject to the boundary conditions (l is the thickness of the film): (i) $t = 0, 0 < x < l : c = 1$ (initial uniform concentration of material); (ii) $t > 0, x = l : c = 0$ (zero concentration at the surface of the film); (iii) all t, $x > l$: $c = 0$ (zero concentration outside the film); (iv) all t, $x = 0$: $\partial c/\partial x = 0$ (no diffusion across the lower surface of the film). l is the thickness of the film.

Now, since the diffusion coefficient D is assumed constant, we may write:

$$\frac{\partial c}{\partial t} = D\left(\frac{\partial^2 c}{\partial x^2}\right) \tag{B.2}$$

Firstly, we assume the equation is separable, i.e. $c = X(x)T(t)$ where X and T are functions of distance and time only, respectively. Now:

$$D\frac{X''(x)}{X(x)} = \frac{T'(t)}{T(t)} = -C \tag{B.3}$$

where C is some constant. Integration yields:

$$T = C_1 \exp(-Ct) \tag{B.4}$$

where C_1 is another constant. Also:

$$X'' = \frac{-C}{D}X \tag{B.5}$$

$$\Rightarrow X = A\cos\left(x\sqrt{\frac{C}{D}}\right) + B\sin\left(x\sqrt{\frac{C}{D}}\right) \tag{B.6}$$

A and B are also constants. Hence:

$$c(x,t) = C_1 \exp(-Ct)\left[A\cos\left(x\sqrt{\frac{C}{D}}\right) + B\sin\left(x\sqrt{\frac{C}{D}}\right)\right] \tag{B.7}$$

$$\Rightarrow \frac{\partial c}{\partial x} = C_1 \exp(-Ct)\left[-A\sqrt{\frac{C}{D}}\sin\left(x\sqrt{\frac{C}{D}}\right) + B\sqrt{\frac{C}{D}}\cos\left(x\sqrt{\frac{C}{D}}\right)\right] \tag{B.8}$$

Boundary condition (iv) gives $\partial c/\partial x = 0$ at $x = 0$, giving $B = 0$. So:

$$c = C_1 A \exp(-Ct)\cos\left(x\sqrt{\frac{C}{D}}\right) \tag{B.9}$$

By choosing an appropriate scaling we may set $C_1 A = 1$. Boundary condition (ii) gives

$c = 0$ at $x = l$ for $t > 0$. Therefore:

$$\cos\left(l\sqrt{\frac{C}{D}}\right) = 0$$

$$\Rightarrow C = \frac{D}{4l^2}(2n+1)^2\pi^2 \tag{B.10}$$

where n is any integer. Each value of n gives a particular solution of equation B.9 above. The full solution is the sum of these solutions, where each solution is multiplied by its associated constant a_n:

$$c(x,t) = \sum_{n=0}^{\infty} a_n \cos\left(\frac{(2n+1)\pi}{2l}x\right) \exp\left[\frac{-D(2n+1)^2\pi^2}{4l^2}t\right] \tag{B.11}$$

We need to solve this for a_n for all x. Choosing $t = 0$, multiplying by $\cos((2m+1)\pi x/2l)$ (where m is any integer) and integrating over the thickness of the film:

$$\int_0^l c(x,0) \cos\left(\frac{(2m+1)\pi}{2l}x\right) dx$$
$$= \sum_{n=0}^{\infty} a_n \int_0^l \cos\left(\frac{(2n+1)\pi}{2l}x\right) \cos\left(\frac{(2m+1)\pi}{2l}x\right) dx \tag{B.12}$$

Since $2\cos A \cos B \equiv \cos(A+B) + \cos(A-B)$ and $c(x,0) = 1$ for all x (boundary condition (i)):

$$\int_0^l c(x,0) \cos\left(\frac{(2m+1)\pi}{2l}x\right) dx$$
$$= \frac{1}{2}\sum_{n=0}^{\infty} a_n \int_0^l \cos\left(\frac{(n+m+1)\pi}{l}x\right) + \cos\left(\frac{(n-m)\pi}{l}x\right) dx \tag{B.13}$$

Integrating:

$$\frac{2l}{(2m+1)\pi}\sin\left(\frac{(2m+1)\pi}{2}\right) = \frac{1}{2}\sum_{n=0}^{\infty} a_n \frac{l}{(n-m)\pi}\sin((n-m)\pi) \tag{B.14}$$

The term inside the sum on the right-hand side of this equation is zero unless $n = m$. Hence:

$$\frac{2l}{(2n+1)\pi}(-1)^n = \frac{1}{2}l a_n$$
$$\Rightarrow a_n = \frac{4(-1)^n}{(2n+1)\pi} \tag{B.15}$$

Now we may write the full solution for the concentration profile across the film:

$$c(x,t) = \sum_{n=0}^{\infty} \frac{4(-1)^n}{(2n+1)\pi} \cos\left(\frac{(2n+1)\pi}{2l}x\right) \exp\left[\frac{-D(2n+1)^2\pi^2}{4l^2}t\right] \tag{B.16}$$

We are required to find M_t/M_∞ which is the fractional amount of material lost from the film at time t. This is:

$$\frac{M_t}{M_\infty} = 1 - \frac{\int_0^l c(x,t)\mathrm{d}x}{\int_0^l c(x,0)\mathrm{d}x} = 1 - \frac{1}{l}\int_0^l c(x,t)\mathrm{d}x$$
$$= 1 - \frac{1}{l}\sum_{n=0}^{\infty} \frac{4(-1)^n}{(2n+1)\pi} \exp\left[\frac{-D(2n+1)^2\pi^2}{4l^2}t\right] \int_0^l \cos\left(\frac{(2n+1)\pi}{2l}x\right)\mathrm{d}x$$
$$= 1 - \frac{1}{l}\sum_{n=0}^{\infty} \frac{4(-1)^n}{(2n+1)\pi} \exp\left[\frac{-D(2n+1)^2\pi^2}{4l^2}t\right] \frac{2(-1)^n l}{(2n+1)\pi}$$
$$\Rightarrow \frac{M_t}{M_\infty} = 1 - \sum_{n=0}^{\infty} \frac{8}{(2n+1)^2\pi^2} \exp\left[\frac{-D(2n+1)^2\pi^2}{4l^2}t\right] \tag{B.17}$$

Measurement of D from experimental data

In the experiments, the mass of acetone in the sample (M_t) is measured as a function of time. Figure B.7 shows a typical result from these experiments. The initial mass of acetone (M_∞) is known. There are several ways to recover the diffusivity D from these data (Crank 1975). The most convenient way is to measure the time taken for a third of the acetone to evaporate $(t_{1/3})$. By substituting $M_t/M_\infty = 1/3$ into equation B.17, we
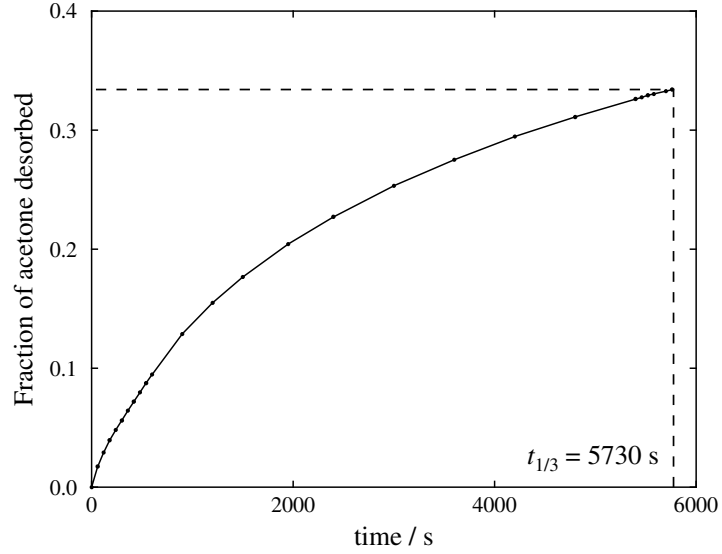
Figure B.7: A typical result from an experiment to measure the diffusivity of acetone in a sample of GRA solution. The time taken for 1/3 of the original acetone to be lost is 5730 s. $\rho = 985$ kg m^{-3} and $m_0 = 6.447$ g giving $l = 0.994$ mm (equation B.19). This gives a diffusivity of 1.50×10^{-11} m^2 s^{-1} (equation B.18). Errors on each point are approximately the size of the marker.

obtain:

$$D \simeq 0.0872 \frac{l^2}{t_{1/3}} \qquad (B.18)$$

The thickness of the solution film is very difficult to measure *in situ*. It is calculated from the following formula:

$$l = \frac{4m_0}{\rho \pi d^2} \qquad (B.19)$$

where m_0 is the initial mass of the solution, ρ is the density of the solution and d is the diameter of the dish. The solution density is measured by weighing a known volume of solution and is slightly dependent on the acetone concentration (figure B.8).

The results of these experiments are given in table B.2 and figure B.9. The measured values of D cover a range between 2.8×10^{-12} and 2.8×10^{-11} m^2 s^{-1}. These values are very close to those estimated for the diffusivity of water in rhyolitic magma under eruption
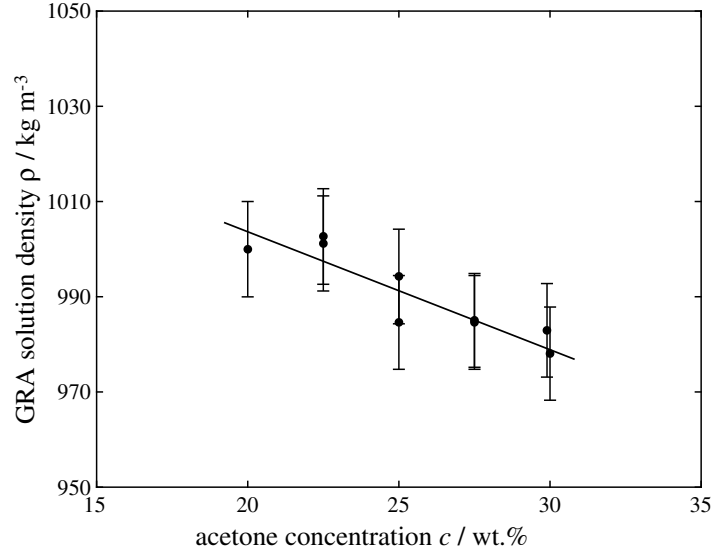
Figure B.8: The density of GRA solution as a function of its acetone concentration. The best fit line is $\rho = 1052 - 2.403c$, $R^2 = 0.81$. The density is calculated by weighing 100 cm^3 of solution in a measuring cylinder. The error on the measurement of volume is ± 1 cm^3; the uncertainty in measuring the mass of the solution is much smaller ($\sim \pm 0.1$g in ~ 100g) giving a total error on each measurement of $\pm 1\%$.

conditions (Watson 1994; Zhang and Behrens 2000). Note that measurement of D using this method is only practical for solutions with 20 wt.% acetone or more. Beneath this value, solutions become too viscous to easily spread into a thin film. This represents a major limitation of the method.

Concentration-dependent diffusivity

The measured diffusivity is clearly dependent on the initial acetone content of the solution film. The higher the acetone content, the higher the calculated diffusivity. The measured value of D is therefore the *average* of the diffusivity from zero to the initial concentration of acetone (Crank 1975):

$$D_{\text{measured}} = \frac{1}{c_0} \int_0^{c_0} D \, dc \tag{B.20}$$

Initial acetone concentration (wt.%)	Diffusivity / 10^{-11} $\mathrm{m^2\,s^{-1}}$
30.0	2.82
29.9	2.16
27.5	1.67
27.5	1.96
25.0	1.05
25.0	1.50
22.5	0.99
22.5	0.72
20.0	0.28

Table B.2: Diffusivity of acetone calculated (equation B.18) at different initial acetone concentrations. Errors on each measurement are around 10%. Also see figure B.9
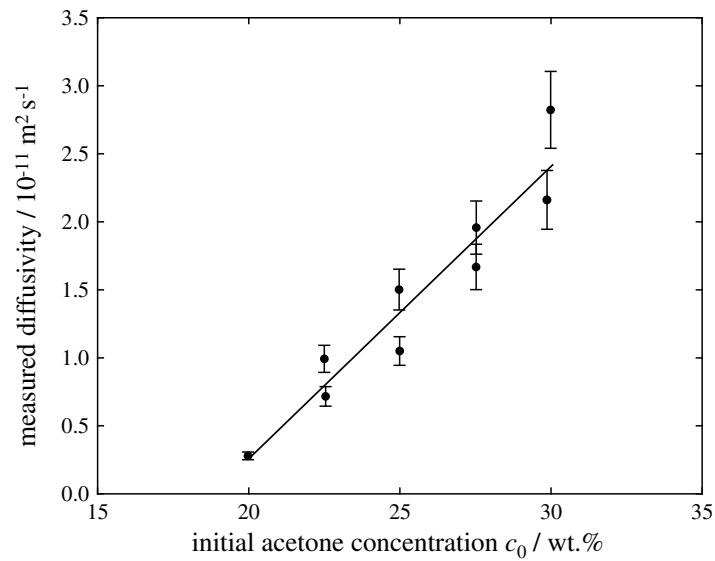

Figure B.9: Measured acetone diffusivity (equation B.18) as a function of initial acetone concentration (table B.2). The measured diffusivity is strongly dependent on the initial acetone content. The linear best fit line has the equation $D_{\mathrm{measured}} = (0.217c_0 - 4.09) \times 10^{-11}$ $\mathrm{m^2\,s^{-1}}$ with correlation coefficient $R^2 = 0.91$.

where c_0 is the initial concentration of acetone in the film. It is possible to derive the functional form of $D(c)$ from equation B.20 by plotting $c_0 \, D_{\mathrm{measured}}$ against c_0 and differentiating the resulting curve numerically. This method, however, requires very large amounts of data to achieve acceptable accuracy. It was decided that the calculated average diffusivity (table B.2) was sufficient to conveniently describe the degassing behaviour of GRA solutions.

Sources of error

The formal error on the measurement of D from equations B.18 and B.19 is very small since all the parameters (m_0, d, ρ and $t_{1/3}$) in these equations can be measured with an accuracy of 1% or better. It is estimated that the largest errors arise from variations in the thickness l of the film, especially near the edge of the dish where a prominent meniscus was observed to develop with time. D depends on l^2 so small errors in l lead to large errors in D. The actual error on l is very hard to quantify with certainty, but I estimate it to be around 5%, giving a total error of 10% on the measured value of D.

Appendix C

Derivation of the hydrodynamic equation of bubble growth in the case of radially-varying viscosity

The author is very grateful to Dr S.D.R. Wilson of the Department of Mathematics, University of Manchester for this derivation.

C.1   Rate of strain tensor

Let the rate of strain tensor be $\dot\gamma_{ij}$. We wish to find

$$\dot\gamma_{rr} = \frac{1}{\mathrm{d}A}\frac{\partial}{\partial t}(\mathrm{d}A) = \frac{\mathrm{d}\dot A}{\mathrm{d}A} \tag{C.1}$$

Now

$$\mathrm{d}A = X^2\frac{\mathrm{d}X}{A^2}$$

$$\mathrm{d}\dot A = -2\frac{X^2}{A^3}\,\mathrm{d}X \ \dot A = -2\frac{X^2}{A^3}\,\mathrm{d}X\,\frac{R^2\dot R}{A^2}$$

$$\Rightarrow \dot\gamma_{rr} = -2\frac{R^2\dot R}{A^3} = -\frac{2R^2\dot R}{R^3 - R_0^3 + X^3} = -2\epsilon \tag{C.2}$$

where

$$\epsilon = \frac{R^2 \dot{R}}{R^3 - R_0^3 + X^3} \tag{C.3}$$

Hence, by incompressibility and radial symmetry:

$$\dot{\gamma}_{\theta\theta} = \dot{\gamma}_{\phi\phi} = \epsilon \tag{C.4}$$

C.2 Force balance

Let the total stress tensor be σ_{ij}. Consider a small surface element $\mathrm{d}s$ of a spherical shell, distant A from the origin, subtending there an angle $\mathrm{d}\lambda$. Tangential stresses give a force of $2\sigma_{\theta\theta}\mathrm{d}A\,\mathrm{d}s(\mathrm{d}s/A)$ towards the origin. Normal stresses give $(\sigma_{rr}\mathrm{d}s^2)_X^{X+\mathrm{d}X}$ away from the origin. The mass-acceleration of the element is $\rho_m \mathrm{d}A\,\mathrm{d}s^2\,\ddot{A}$. The equation of motion is therefore:

$$\rho_m \mathrm{d}A\,\mathrm{d}s^2\,\ddot{A} = \left(\sigma_{rr}\mathrm{d}s^2\right)_X^{X+\mathrm{d}X} - 2\frac{\sigma_{\theta\theta}}{A}\mathrm{d}A\,\mathrm{d}s^2 \tag{C.5}$$

Now, using $\mathrm{d}s = A\mathrm{d}\lambda$ and $\mathrm{d}\lambda$ is a constant, and $\mathrm{d}A = X^2\mathrm{d}X/A^2$ we obtain:

$$\rho_m \frac{X^2}{A^2}\ddot{A} = \frac{\partial \sigma_{rr}}{\partial X} + 2\frac{X^2}{A^3}\left(\sigma_{rr} - \sigma_{\theta\theta}\right) \tag{C.6}$$

C.3 The equation of motion

Assuming the liquid is Newtonian with viscosity η, we have:

$$\sigma_{rr} = -p + 2\eta\dot{\gamma}_{rr} = -p - 4\eta\epsilon$$

$$\sigma_{\theta\theta} = -p + 2\eta\dot{\gamma}_{\theta\theta} = -p + 2\eta\epsilon \tag{C.7}$$

Substituting into equation C.6 and neglecting the inertial term, we have:

$$0 = -\frac{\partial p}{\partial X} - 4\epsilon\frac{\partial \eta}{\partial X} \tag{C.8}$$

At $X = R_0$, $\epsilon = \dot{R}/R$, and at $X = S_0$, $\epsilon = \dot{S}S$. Continuity of normal stress (σ_{rr}) at $X = R_0$ and $X = S_0$ gives:

$$p_g = p(R_0, t) + 4\eta(R_0, t)\frac{\dot{R}}{R}$$
$$p_\infty = p(S_0, t) + 4\eta(S_0, t)\frac{\dot{S}}{S} \tag{C.9}$$

Integrating (C.8) by parts with respect to X between R_0 and S_0:

$$p(S_0, t) - p(R_0, t) = -4\int_{R_0}^{S_0}\epsilon\frac{\partial \eta}{\partial X}\,\mathrm{d}X$$
$$= 4\int_{R_0}^{S_0}\eta\frac{\partial \epsilon}{\partial X}\,\mathrm{d}X - 4\eta(S_0, t)\frac{\dot{S}}{S} + 4\eta(R_0, t)\frac{\dot{R}}{R} \tag{C.10}$$

Combining equations C.9 and C.10:

$$p_\infty - p_g = \int_{R_0}^{S_0}4\eta\frac{\partial \epsilon}{\partial X}\,\mathrm{d}X \tag{C.11}$$

and, substituting for ϵ from equation C.3:

$$p_g = p_\infty + 12R^2\frac{\mathrm{d}R}{\mathrm{d}t}\int_{R_0}^{S_0}\frac{\eta(c)X^2}{(R^3 - R_0^3 + X^3)^2}\,\mathrm{d}X \tag{C.12}$$

Appendix D

Finite difference form of the diffusion equation in transformed, radial, Lagrangian coordinates

In the transformed coordinate system (section 3.3.3) the diffusion equation 3.5 becomes:

$$\frac{\partial \tilde{c}}{\partial t} = \frac{1}{e^{3Y}} \frac{\partial}{\partial Y} \left(k(\tilde{c}) \frac{A^4}{e^{3Y}} \frac{\partial \tilde{c}}{\partial Y} \right) \tag{D.1}$$

We wish to find an appropriate finite-difference form of the right hand side of this equation. At a general grid point i, integrating between the interpolated grid points $i - 1/2$ and $i + 1/2$:

$$\frac{\partial}{\partial Y} \left(k(\tilde{c}) \frac{A}{e^{3Y}} \frac{\partial \tilde{c}}{\partial Y} \right)_i \simeq \frac{1}{\delta Y} \left[\left(k(\tilde{c}) \frac{A}{e^{3Y}} \frac{\partial \tilde{c}}{\partial Y} \right)_{i+1/2} - \left(k(\tilde{c}) \frac{A}{e^{3Y}} \frac{\partial \tilde{c}}{\partial Y} \right)_{i-1/2} \right] \tag{D.2}$$

We approximate the diffusivity at an interpolated grid point as the mean of the diffusivities at the bracketing grid points. The concentration gradient $\partial \tilde{c}/\partial Y$ is similarly approximated:

$$k_{i+1/2} \simeq \frac{k_{i+1} + k_i}{2} \qquad k_{i-1/2} \simeq \frac{k_i + k_{i-1}}{2}$$

$$\left. \frac{\partial \tilde{c}}{\partial Y} \right|_{i+1/2} \simeq \frac{\tilde{c}_{i+1} - \tilde{c}_i}{\delta Y} \qquad \left. \frac{\partial \tilde{c}}{\partial Y} \right|_{i-1/2} \simeq \frac{\tilde{c}_i - \tilde{c}_{i-1}}{\delta Y}$$

The values of $A_{i+1/2}$, $A_{i-1/2}$, $Y_{i+1/2}$ and $Y_{i-1/2}$ may be calculated precisely. This gives:

$$\frac{\mathrm{d}\tilde{c}_i}{\mathrm{d}t} = \frac{1}{2\,e^{3Y}\,\delta Y^2} \left\{ (k_{i+1} + k_i)(\tilde{c}_{i+1} - \tilde{c}_i)\frac{A_{i+1/2}^4}{e^{3Y_{i+1/2}}} \right.$$

$$\left. - (k_i + k_{i-1})(\tilde{c}_i - \tilde{c}_{i-1})\frac{A_{i-1/2}^4}{e^{3Y_{i-1/2}}} \right\} \quad \text{(D.3)}$$